

Imaging using volume holograms

by

Arnab Sinha

B.Tech., Mechanical Engineering,
Indian Institute of Technology, Kharagpur (2000)

Submitted to the Department of Mechanical Engineering
in partial fulfillment of the requirements for the degree of

Doctor of Philosophy in Mechanical Engineering

at the

MASSACHUSETTS INSTITUTE OF TECHNOLOGY

~~February~~ 2004 JUN 2004

© Massachusetts Institute of Technology 2004. All rights reserved.

Author

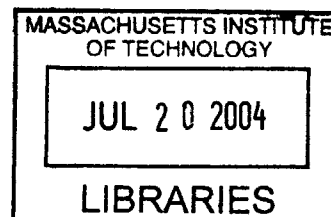
.....
Department of Mechanical Engineering
February 25, 2004

Certified by.

.....
George Barbastathis
Esther and Harold E Edgerton Assistant Professor
Thesis Supervisor

Accepted by

Ain A. Sonin
Chairman, Department Committee on Graduate Students



BARKER

Imaging using volume holograms

by

Arnab Sinha

Submitted to the Department of Mechanical Engineering
on February 25, 2004, in partial fulfillment of the
requirements for the degree of
Doctor of Philosophy in Mechanical Engineering

Abstract

Volume holograms can be thought of as self-aligned 3D stacks of diffractive elements that operate coherently on incident fields as they propagate through the structure. In this thesis, we propose, design and implement imaging systems that incorporate a volume hologram as one of the elements that operate on the optical field incident on the imaging system. We show that a volume hologram acts like a “smart” lens that can perform several useful functions in an imaging system and demonstrate the same experimentally. To this end, we first develop the theory of volume holographic imaging and calculate the imaging properties of the field diffracted by a volume hologram for the special cases of coherent and incoherent monochromatic illumination. We concentrate on two simple imaging system configurations, *viz.* volume holograms recorded using a planar signal and either a spherical or a planar reference beam. We pay particular attention to the depth resolution of each system and discuss how appropriately designed objective optics placed before the volume hologram can enhance the depth resolution. We also derive the imaging properties of the volume holographic “smart” lens under conditions of incoherent broadband illumination. We show that multiple volume holographic sensors can be configured to acquire different perspectives of an object with enhanced resolution. We experimentally verify the developed theories and implement several volume holographic imaging systems for a wide range of imaging applications. We compare volume holographic imaging with some commonly used 3D imaging systems and discuss the merits of each system. We find that volume holograms with low diffraction efficiencies result in lower photon counts and information loss and hence poorer imaging performance. We present an optical method to solve this problem by resonating the volume hologram inside an optical cavity. Finally, we conclude with some directions for future work in this emerging field.

Thesis Supervisor: George Barbastathis

Title: Esther and Harold E Edgerton Assistant Professor

Acknowledgments

Firstly, I would like to thank my advisor George Barbastathis. I came to MIT knowing little Electromagnetics and even less about optics reserach. He has been instrumental in guiding me during the course of my research and for this I will forever be grateful. More importantly, he taught me to appreciate good wine and steak during the many conferences that we attended. I have had a lot of fun over the last four years and a lot of that is on account of him.

I would also like to thank my thesis committee: Professors Cardinal Warde, Demetri Psaltis and Peter So for taking the time to offer valuable advice about my work. I thoroughly enjoyed the discussions we had and have made it a point to follow their recommendations.

I would also like to thank my colleagues (past and present) at the 3D Optical Systems group for all their help and various stimulating discussions: Andy Stein, Carlos Hidrovo, Greg Nielson, Hyun-Jin In, Kehan Tian, Stan Jurga, Tina Shih, Troy Savoie, Wei-Chuan Shih and especially Wenyang Sun for his help in setting up the various experiments.

Lastly I would like to thank my family: Ba, Ma and Rit for all their support and encouragement; my immediate relatives in the US: Mesomosai, Masi, Dada and Sonai for all their affection and finally Varsha for being there for me all the time.

Contents

1	Introduction	29
1.1	Fundamentals of Imaging Systems	31
1.1.1	Classification of Imaging Systems	32
1.1.2	Analysis of 2D Lens-Based Imaging Systems	34
1.1.3	Filtering Methods Used in Lens-Based 3D Imaging	35
1.2	Imaging Using 3D Optical Elements	37
1.2.1	Volume Holographic Imaging (VHI)	38
1.2.2	Impulse Response of Volume Holographic Lens with Baseband Modulation	42
1.2.3	Impulse Response of Volume Holographic Lens with Carrier Frequency	43
1.3	Outline of this Thesis	47
2	Volume Holographic Imaging Fundamentals	49
2.1	Spherical Reference Volume Holographic Imaging (SR-VHI)	50
2.1.1	Derivation and properties of the diffracted field	50
2.1.2	Depth resolution	57
2.1.3	Design of objective optics	60
2.1.4	Experimental validation	64
2.2	VHI using plane wave reference beams	65
2.2.1	Derivation and properties of the diffracted field	65
2.2.2	Depth resolution	71
2.2.3	Design of the objective optics	74

2.2.4	Design of telephoto objective optics for PR-VHI systems . . .	77
2.2.5	Experimental validation	80
2.3	Exploiting a-priori object information to enhance depth resolution . .	83
2.4	PR-VHI using broadband illumination	86
2.5	Depth resolution of PR-VHI under broadband illumination	91
3	<i>N</i>-ocular Volume Holographic Imaging	99
3.1	Resolution of PR-VHI systems	99
3.2	Overcoming depth resolution degradation using multiple PR-VHI sen- sors and digital post-processing	101
3.2.1	<i>N</i> -ocular VHI for surface profilometry	103
3.2.2	<i>N</i> -ocular VHI for 3D Imaging	106
4	Volume Holographic Imaging Systems	117
4.1	Classification of VHI systems	117
4.1.1	Type of object/illumination	117
4.1.2	Single hologram / Many multiplexed holograms	118
4.1.3	Single / Multiple VHI sensors in the imaging system	119
4.1.4	Type of objective optical system	119
4.2	VHI implementations	120
4.2.1	{Reflective object + Active illumination, Single hologram, Sin- gle sensor, No objective optics}	121
4.2.2	{Reflective object + Active illumination, Single hologram, Sin- gle sensor, Microscope objective optics}	124
4.2.3	{Reflective object + Active illumination, Single hologram, Sin- gle sensor, Telescope/telephoto objective optics}	125
4.2.4	{Reflective object + Active illumination, Single hologram, Sin- gle sensor, Inclined telephoto objective optics}	126
4.2.5	{Reflective object + Active illumination, Single hologram, Two sensors, Telescope objective optics}	128

4.2.6	{3D fluorescent object + Active illumination, Single hologram, Three sensors, Telephoto objective optics}	130
4.2.7	{Reflective object + Broadband passive illumination, Single hologram, Single sensor, Telephoto objective optics}	131
4.2.8	{3D fluorescent object + Active illumination, Multiple holograms, Single sensor, Microscope objective optics}	133
4.3	Volume holographic spectrometer	134
5	Comparison of VHI with Other 3D Imaging Systems	137
5.1	Comparison of Depth Resolution	137
5.1.1	Comparison of Δz_{FWHM} of a Binocular System and telescopic VHI system	138
5.1.2	Comparison of Δz_{FWHM} of a Confocal Microscope and VHI system	139
5.2	Information Theoretic Analysis of VHI	140
5.2.1	Imaging Mutual Information of Incoherent Imaging Systems	143
5.2.2	Mutual Image Information for fluorescent objects elongated in the direction of the optical axis	149
5.2.3	Numerical comparison	155
6	Resonant Volume Holography	161
6.1	Introduction to Resonant Holography	161
6.2	Resonant Holographic Systems	166
6.3	Resonant holographic imaging architectures	169
7	Conclusion	173
7.1	Volume Holographic Imaging Summary	173
7.2	Future work	176
A	Volume diffraction in the Born approximation	179

List of Figures

1-1	Imaging system schematic	31
1-2	(a) A 2D imaging system can not discriminate the distance between two objects; (b) a 3D imaging system can recover depth information by scanning and (c) a $2\frac{1}{2}$ D imaging system maps the height of a reflective surface to an intensity on the detector.	32
1-3	Imaging system schematic	34
1-4	Simplified schematics of traditional holographic imaging (a) Recording (b) Readout by scanning. Schematics of volume holographic imaging (VHI) (c) Making VH lens (d) Readout.	39
1-5	Generic volume hologram based imaging system.	41
1-6	Volume holographic imaging system using the $4F$ geometry.	42
1-7	Bragg selectivity of volume holograms, (a) Recording; (b) Bragg matched readout using a replica of the reference beam; (c) Bragg mismatched readout results in a weak diffracted field; (d) A Bragg degenerate beam yields a strong diffracted beam. The Bragg degenerate beam is of different wavelength and is incident at a different reference angle governed by Bragg selectivity.	44
1-8	Schematic of VHI system. A CCD camera monitors the diffracted beam to detect the whether the light scattered by the object contains any Bragg matched and/or Bragg degenerate components.)	45

2-1	General schematic of volume holographic imaging. (a) The volume grating is the recorded 3D interference pattern of two mutually coherent beams (b) The imaging step consists of reading out the volume hologram by an unknown object illumination. The volume hologram diffracts only the Bragg matched components of the object illumination. This effect is used in conjunction with scanning to recover the object illumination.	50
2-2	Spherical wave reference VHI, (a) Recording and (b) Readout(imaging).	51
2-3	Intensity pattern observed on the detector for spherical VHI for (NA)= 0.07, $\theta_s = 12^\circ$ (0.21 rad) and $\delta = 6$ mm. (a) Diffraction pattern caused by axial defocus, (b) Crescent shaped Bragg filter of SR hologram, (c) Diffracted pattern observed on the detector.	54
2-4	VHI is a shift variant imaging system; the observed diffracted field changes with a change in the spatial location of the point source: (a) Mutually incoherent point sources with no defocus, (b) Mutually incoherent point sources with defocus δ	56
2-5	VHI methods (a) 3D scanning using an integrating detector and focussed illumination (b) Exploiting y - degeneracy by using a CCD and 2D scanning with extended illumination.	57
2-6	Theoretical and experimental plots of longitudinal PSF for SR-VHI.	58
2-7	Computed contour lines giving the fraction of the total diffracted power which falls within small circles centered at the Bragg matched point versus selected values of the defocus term. Values corresponding to a defocus equal to the FWHM are indicated by the dashed lines.	59
2-8	Dependence of G_{SR} on θ_s	61
2-9	SR-VHI systems (a) without objective optics (b) with objective optics in between the hologram and object.	62
2-10	Depth resolution Δz_{FWHM} of SR-VHI system degrades quadratically with working distance.	63

2-11	Theoretical and experimental diffracted patterns on CCD for SR-VHI with a point source displaced $\delta = 4$ mm from Bragg match.	64
2-12	Observed diffracted fields on CCD for three mutually incoherent points, (a) Points are at the Bragg matched plane and (b) points are at a defocused plane $\delta = 4$ mm.	65
2-13	Plane wave reference VHI schematic, (a) Recording; (b) Bragg matched readout and (c) Bragg mismatched readout.	66
2-14	Intensity pattern observed on the detector for spherical VHI for (NA)= 0.07, $\theta_s = 12^\circ$ (0.21 rad) and $\delta = 8$ mm. (a) Diffraction pattern caused by axial defocus and the finite aperture of collimating lens, (b) Straight Bragg slit of PR hologram, (c) Diffracted pattern observed on the detector.	69
2-15	PR-VHI using a line source to reduce scanning required (a) Schematic (b) Intensity pattern observed on CCD.	70
2-16	Longitudinal PSF for PR-VHI.	72
2-17	Depth resolution degrades slightly when using a line readout as opposed to a point readout. The PR-VHI system had an objective lens with $f = 50.2$ mm and $a = 5$ mm; $\theta_s = 25^\circ$. The volume hologram was 2 mm thick crystal of LiNbO_3 with diffraction efficiency $\eta = 5\%$ recorded using a doubled Nd:YAG laser with $\lambda = 532$ nm.	73
2-18	VHI by exploiting the y -degeneracy by using a camera at the detector plane (a) Line scanning of object with small surface features (b) Line scanning of object with large surface features.	74
2-19	Schematic for design of an objective optical system to obtain high depth resolution at large working distances in VHI systems.	75
2-20	Appropriately designed objective optics can improve the Δz_{FWHM} of a PR VHI system. (a) PR VHI schematic without objective optics (b) PR VHI schematic with objective optics.	77

2-21	An appropriately designed telephoto system can improve working distance d without any degradation in the resolution. PSFs for stand alone PR VHI system (dashed line) and telephoto PR-VHI system (solid line) show that both systems have $\Delta z_{\text{FWHM}} \approx 1$ mm for $d = 50$ mm and $d = 500$ mm respectively.	79
2-22	Calculation of FOV for telephoto PR VHI system, the chief ray makes an angle α with the optical axis.	79
2-23	(a) Theoretical (solid line) and experimental (crosses) Δz_{FWHM} vs a for fixed f and L , confirming the inversely proportional relationship to (NA) in this case. (b) Theoretical (solid line) and experimental (crosses) Δz_{FWHM} vs f for fixed a and L , confirming the quadratic dependence on f	80
2-24	Theoretical and experimental diffracted patterns on CCD for PR VHI with a point source displaced $\delta = 8$ mm from Bragg match.	81
2-25	PR VH images of the fabricated letters MIT placed 50.2 mm away from the entrance pupil of the system. (a) is the actual CAD rendering of the object, (b) is a PR volume holographic image of the object obtained by a 1D scan with surface of the letter M being placed at Bragg matched location, (c) is an image of the object obtained by a 1D scan with surface of the letter I being placed at Bragg matched location and (d) is an image of the object obtained by a 1D scan with surface of the letter T being placed at Bragg matched location.	82
2-26	PR VH images using collector optics of the fabricated letters MIT placed 500 mm away from the entrance pupil of the system. (a) is a PR volume holographic image of the object obtained by a 1D scan with surface of the letter M being placed at Bragg matched location, (b) is an image of the object obtained by a 1D scan with surface of the letter I being placed at Bragg matched location and, (c) is an image of the object obtained by a 1D scan with surface of the letter T being placed at Bragg matched location.	84

2-27 (a) PR-VHI metrology system at normal incidence (b) Inclined PR-VHI system to exploit a-priori object information.	85
2-28 Depth resolution improves by taking advantage of a-priori object information. The PR-VHI sensor had $f = 460$ mm, $a = 5$ mm and $F = 50.2$ mm for the same LiNbO ₃ crystal used in Fig.2-17.	86
2-29 Setup for experimental verification of diffracted field for two color readout	90
2-30 Experimentally observed diffracted field for readout using two mutually incoherent Bragg matched point sources emitting at $\lambda_p = 532$ nm and $\lambda_p = 632.8$ nm. (a) Defocus $\delta = 0$ (b) $\delta = 4$ mm. All lateral dimensions are in mm.	92
2-31 (a)Percentage change in wavelength-normalized Δz_{FWHM} as a function of normalized wavelength μ . We note that the PSF narrowing effect is very small and can be neglected for most practical purposes as seen in (b) Experimentally observed longitudinal PSFs for the two point sources described in Fig.2-30.	93
2-32 Experimentally observed diffraction pattern observed for broadband fluorescent object emitting at $\lambda_p = 580 \pm 20$ nm. (a) Comparing Bragg matched laser $\lambda_p = 532$ nm and fluorescent source. (b) Fluorescent source stays visible for a large lateral translation $\Delta x' = 3$ mm. (c) Bragg slit at $\delta = 2$ mm for the fluorescent source is wider than the laser Bragg slit.	94
2-33 Depth resolution under broadband illumination. (a) Simulation setup used, the object is assumed to emit at two discrete wavelengths $\lambda_{p,1} = 532$ nm and $\lambda_{p,2} = 540$ nm, $a = 12.7$ mm, $f = 50.2$ mm, $L = 2$ mm and $\theta_s = 30^\circ$ (b) Theoretical PSFs: Solid line $\mu = 1$; dashed line $\mu = 1.015$; the dotted line is the incoherent sum of the two PSFs and is broader than the monochromatic PSF.	95

2-34	Comparing depth resolution for monochromatic and broadband illumination. The broadband PSF (dashed line) is broader than the monochromatic PSF (solid line).	96
2-35	Tradeoff involved in between field of view and depth resolution for broadband VHI. (a) Object of interest is the bottom screw in the chassis of the toy car. (b) & (c) The FOV for narrowband (green light with $\Delta\lambda \approx 10$ nm) illumination is much lesser than that of broadband illumination (white light with $\Delta\lambda \approx 120$ nm). All lateral dimensions are in mm. (d) Depth resolution, or equivalently the contrast in between surface features at different heights is much better for the narrowband illumination as also shown in (e) the theoretical PSF curves under narrowband and broadband illumination.	98
3-1	Theoretical performance of imaging with multiple sensors. (i) PSF of single sensor. (ii) PSF of two sensors at $\phi = 90^\circ$. (iii) PSF of three sensors at 45° . (iv) PSF of four sensors at 30°	102
3-2	Theoretical depth resolution (FWHM) for different imaging geometries. ϕ refers to the viewing angle available to the VHI sensors (except when $\phi=0$, which refers to a monocular system). The number of sensors is taken to be 4 and we plot the expected value of the depth resolution for an arrangement of sensors from a uniform probability distribution.	103
3-3	Experimental PSFs for two individual sensors oriented at $\phi = 10^\circ$ for point sources located at different distances in front of the sensor.(a) 29 cm; (b) 45 cm; (c) 72 cm.	104
3-4	Theoretical performance of 7-ocular 1D sensor after post processing using a pseudo inverse. The SNR of each measurement is 10. The sensors are oriented in steps of 15° starting at 0° . The red curve indicates the original signal. It is seen that the pseudo inverse solution (extreme right) returns the correct location of the source whereas individual inversions do not.	106

3-5	Schematic of N -ocular VHI system. For illustration purposes, we have depicted $N = 3$	107
3-6	All voxels located along a line in the object space are mapped on to the same lateral location on the detector.	109
3-7	Several point sources that satisfy (3.12) are <i>simultaneously</i> imaged by the PR volume hologram according to (3.13).	110
3-8	Inversion scheme to reconstruct 3D object data from 2D VHI images.	110
3-9	A broadband PR-VHI system measures the Radon transform of an object along a direction specified by the inclination of the sensor.	111
3-10	N -ocular PR-VHI of broadband objects. (a) The object of interest consisted of two fluorescent beads of diameter 0.66 mm and 0.72 mm separated by an aluminum spacer of length 2.91 mm. (b) and (c) are VHI PR-images of the object at inclination angles $\phi_b = 0^\circ$ and $\phi_c = 45^\circ$ respectively.	112
3-11	3D image of object shown in Fig. 3-10 using the inverse Radon transform approach. (a) shows 5 slices through the object and (b) - (f) show the same slices at $y = 0, 0.25, 0.5, 0.75$ and 1 mm side by side. All dimensions are in mm. The separation between the centroids of the two reconstructed beads was calculated to be 3.6 ± 0.01 mm.	114
3-12	The least squares inversion is able to recover the object shown in Fig. 3-10(a) shows 5 slices through the object and (b) - (f) show the same slices at $y = 0, 0.25, 0.5, 0.75$ and 1 mm side by side. All dimensions are in mm.	116
4-1	VHI for {Reflective object + Active illumination, Single hologram, Single sensor, No objective optics}. An intensity detector monitors the beam by the SR hologram diffracted while the object is scanned in 3D.	121

- 4-2 Experimental VH image of a fabricated artifact obtained using 2 mm thick crystal of LiNbO_3 with diffraction efficiency $\eta \approx 5\%$ recorded at $\lambda = 532$ nm. The working distance $d = 5$ cm; $a = 3.5$ mm; $\theta_s = 30^\circ$ and $\Delta z_{\text{FWHM}} \approx 1$ mm. (a) is the actual CAD rendering of the object and (b) is a volume holographic image of the object obtained by a complete lateral scan with surface of the letter M being placed at Bragg matched location, which consequently appears to be bright. 122
- 4-3 VHI for {Reflective object + Active illumination, Single hologram, Single sensor, Microscope optics}. The microscope objective collimates the light reflected from the surface and an intensity detector monitors the diffracted beam as the active probe is scanned with respect to the object. 123
- 4-4 VH image of MEMS grating using microscope objective optics using the same LiNbO_3 crystal but recorded with a normally incident planar reference beam instead of the spherical reference. The microscope objective optics had a working distance of $d = 2$ cm with $a = 0.5$ cm. (a) is a picture of MEMS grating being imaged; the height difference in between the top and bottom of the reflective grating is $24\mu\text{m}$. (b) VH image with laser point focused on the bottom of the grating and (c) VH image after the focus is raised $24\mu\text{m}$ to focus on the top of the grating surface. Note that there is a complete contrast reversal to indicate that the surfaces are indeed at different heights. 124
- 4-5 VHI for {Reflective object + Active illumination, Single hologram, Single sensor, Telescope optics}. The telescope creates an real image of the distant object in front of the SR hologram which then diffracts according to the Bragg condition. An intensity detector monitors the diffracted beam. The entire object surface is recovered by scanning. 125

- 4-6 VH image of microturbine. The hologram was the same LiNbO₃ crystal described in Fig. 4-2. The telescope had angular magnification $M_\alpha = 1.5$ with $d = 16$ cm and $a = 1.2$ cm. (a) Image of the microturbine captured with a standard digital camera; the microturbine was manufactured to have surface height features of $225\mu\text{m}$. (b) Experimental depth response for a point source object at the same distance $\Delta z_{\text{FWHM}} \approx 100\mu\text{m}$; (c - f) VH telescope scans at progressive increments of $100\mu\text{m}$ through the object. At any given depth, the Bragg-matched portions of the object are brightest. 126
- 4-7 VHI for {Reflective object + Active illumination, Single hologram, Single sensor, Inclined telephoto optics}. If it is known that the object consists only of flat surfaces, depth resolution can be improved by inclining the object surface with respect to the scanning direction at an angle ϕ as indicated. This approach exploits the superior depth resolution to improve the apparent depth resolution. 127
- 4-8 Surface scan of nanogate which has surface features $\approx 150\mu\text{m}$ using an inclined telephoto PR-VHI sensor with $d = 46$ cm (a) Image of nanogate captured using standard CCD, (b) PR-VHI image of device with the top surface in focus, (c)& (d) PR-VHI images focused $50\mu\text{m}$ and $100\mu\text{m}$ below the top surface. (e) PR-VHI image focused on the base of the turbine $150\mu\text{m}$ below the top surface. Note that there again is a complete contrast reversal in between images (b) and (e). 127
- 4-9 VHI for {Reflective object + Active illumination, Single hologram, Multiple sensors, Telescope optics}. Multiple VH sensors similar to the one described in Fig. 4-6 are used to simultaneously image the object. This leads to overconstraining the solution to the imaging inverse problem and results in better resolution. 129

4-10	Surface profiles obtained using two VHI sensors imaging the turbine described in Fig. 4-6. One sensor was normal to the turbine surface, the other was inclined at an angle $\phi = 30^\circ$ with respect to the turbine surface. The resultant binocular VH image is obtained by point multiplying the individual images. Note that there is a significant improvement in between the binocular and normal VHI images. However, the improvement is not as discernible in between the inclined sensor and the binocular image on account of the phenomenon described in section 4.2.4.	129
4-11	VHI for {3D fluorescent object + Active illumination, Single hologram, Multiple sensors, Telephoto optics}. Multiple VH sensors similar to that described in Fig. 4-8 acquire different perspectives of the fluorescent 3D object. The multiple measurements allow for an over-constrained solution to overcome the degradation of depth resolution on account of the broadband nature of the fluorescence.	130
4-12	3D image of a set of fluorescent particles arranged in a helical pattern. The object was located at a working distance of $d = 10$ cm from three broadband N -ocular PR-VHI sensors. The image inversion was done using pseudo inverse techniques.	131
4-13	VHI for {Reflective object + Broadband illumination, Single hologram, Single sensor, Telephoto optics}. Increased illumination bandwidth improves the field of view of the VHI system thus reducing the amount of scanning required. However, this is accompanied by degradation of the depth resolution.	132

- 4-14 From section 2.5, surface profiles obtained using broadband illumination and PR-VHI. The object is the bottom chassis of a toy car of Fig. 2-35 . The particular region of interest is a raised screw on the chassis. (a) is the VH image obtained under narrowband illumination whereas in (b) the field of view improves under broadband illumination. However (c) indicates that the depth resolution degrades as the illumination bandwidth increases *i.e.* there is a price to pay for the enhanced field of view with respect to poorer depth discriminating ability. 132
- 4-15 VHI for {3D fluorescent object + Active illumination, Multiple holograms, Single sensor, Microscope optics}. Multiple gratings can be recorded inside the same hologram volume. This results in reduced scanning as the VHI system can simultaneously image multiple locations within the object. This is illustrated in the figure. There are three multiplexed gratings, each observing a different depth slice of the object and then diffracting to a different location on the detector. Thus, the VHI system can simultaneously monitor three locations without any scanning. 133
- 4-16 Experimental demonstration of real time hyperspectral microscope. Three holograms were multiplexed within the same volume to look at three different depth layers of a 3D object that consisted of fluorescent microspheres of diameter $15\mu\text{m}$. The Bragg selectivity of the hologram allows us to simultaneously image three depth slices (one slice is much fainter than the other on account of some recording irregularities); the width of each slice corresponds to the fluorescence bandwidth. 134
- 4-17 Schematic of PR-VHI spectrometer. The illumination whose spectrum is unknown is placed at the Bragg matched plane of the PR-VHI system; the illumination spectrum is the measured 1D intensity function (appropriately scaled) on the detector. 135

4-18	Measured spectrum using two narrow bandpass optical filters 488 ± 10 nm and 532 ± 10 nm (green). The separation in between the green slit and blue slit corresponds to 43.92 nm and the actual wavelength separation is 44 nm.	135
5-1	Setup for comparison of (a) VHI with objective telescope with (b) binocular system	138
5-2	Plots of Δz_{FWHM} versus object distance d for PR VHI (solid lines), SR VHI (dashed line), Confocal systems (dotted line).	140
5-3	Schematic of a general-purpose volume-holographic imaging system.	142
5-4	The IMI measures the actual amount of information that is obtained after transmission through a noisy channel. The IMI is a measure of the relevant information from a measurement since it disregards contributions from channel noise.	146
5-5	(a) Source geometry for the simulations of section 5.2.2. (b) Fluorescence imaging geometry with a lens and a pinhole for depth resolution. (c) Geometry of fluorescence imaging with a volume holographic element. (d) Imaging with a volume holographic element exploiting in parallel the undiffracted beam with the pinhole-based system.	150
5-5	(continued)	151
5-6	Integrated intensity (over infinite detector area) for the volume holographic imaging system of Fig. 5-5(c). The hologram has $u = 0.4$, $R = 1, 500\lambda$ and (a) $\mathbf{r}_f = (0, 0, -10^4\lambda)$, (on-axis hologram) (b) $\mathbf{r}_f = (4 \times 10^3\lambda, 0, -10^4\lambda)$ (off-axis hologram). Results for three different thicknesses are shown.	153

5-7	Comparison of IMI for the imaging system using a lens plus pinhole of varying diameter (Fig. 5-5b) with that of a volume hologram (Fig. 5-5c). The solid line is the IMI of the confocal and the dashed lines are IMI of various volume holograms. Here the holograms are assumed to be ideal, <i>i.e.</i> with diffraction efficiency $\eta = 1$. The hologram data are labelled such that (i) is an $L = 400\lambda$ -thick hologram recorded with an on-axis reference $\mathbf{r}_f = (0, 0, -10^4\lambda)$, plane-wave signal with $u = 0.4$; (ii) is an $L = 1,600\lambda$ -thick hologram recorded with an on-axis reference $\mathbf{r}_f = (0, 0, -10^4\lambda)$, plane-wave signal with $u = 0.4$; and (iii) is an $L = 400\lambda$ -thick hologram recorded with an off-axis reference $\mathbf{r}_f = (4 \times 10^3\lambda, 0, -10^4\lambda)$, plane-wave signal with $u = 0.4$. Increasing L to $1,600\lambda$ in the off-axis geometry leads only to marginal increase in IMI.	156
5-8	Data and layout same as in Figure 5-7, except for a weaker hologram with $\eta = 0.5$	157
5-9	IMI for the combined imaging system of Fig. 5-5(d). The volume holographic geometries considered are (a) on-axis $\mathbf{r}_f = (0, 0, -10^4\lambda)$ with $L = 400\lambda$; (b) on-axis $\mathbf{r}_f = (0, 0, -10^4\lambda)$ with $L = 2,800\lambda$; (c) off-axis $\mathbf{r}_f = (4 \times 10^3\lambda, 0, -10^4\lambda)$ with $L = 2,800\lambda$	159
5-9	(continued)	160
6-1	Geometries for resonant holography: (a) two-port with normal incidence; (b) two-port with oblique incidence; (c) three-port with normal incidence. VHOE: volume holographic optical element; PRM: partially reflecting mirror.	163

6-2	Holographic reconstruction (a) non-resonant and (b) resonant. The hologram of the Air Force Resolution Chart was recorded slightly off the Fourier plane to ensure equal diffraction efficiencies for a wide bandwidth of plane wave components. The resonant and non-resonant reconstructions have comparable quality. This and subsequent experiments were implemented on a 1mm thick slab of Fe-doped LiNbO ₃ with loss coefficient $b \approx 0.05$	165
6-3	Theoretical (solid lines) and experimental sensitivity curves for deviation of the one-pass efficiency η_1 from its resonant value (6.3) for two cases of PRM reflectivity. Loss coefficient of $b = 0.05$ was used for the theoretical curves. The experimental curves were obtained with a lateral aperture of $\approx 1\text{mm}^2$, where resonance was relatively uniform.	166
6-4	Holographic memory with resonant enhancement of the diffraction efficiency. The blue curve was obtained by angular scanning the memory without the resonator. Each peak corresponds to one stored hologram. The red curve was obtained by applying (6.1-6.2) and (6.4) to the experimental data of the blue curve. The black stars are actual values of the corresponding resonant diffraction efficiencies obtained experimentally.	167
6-5	Experimental and theoretical response of the three-port element of Figure 6-1(c) with $r^2 = 0.7$, $r'^2 = 0.9$ and $b = 0.05$	168
6-6	Imaging architectures for resonant imaging. (a) point source outside resonant cavity. (b) collimated point source inside resonant cavity.	169
6-7	Imaging architectures for resonant imaging with point source outside resonant cavity.	170
6-8	Imaging architectures for resonant imaging with point source inside resonant cavity.	171
6-9	(a) Calculated and (b) experimental images on detector for readout of resonant volume hologram with the point source inside the cavity.	171

6-10	Resolution of resonant VHI with the point source within the cavity. The working distance was $660\mu\text{m}$. The NA of the system was 0.1, the one pass diffraction efficiency $\eta_1 = 3.5\%$, loss= 5%. $\eta_\infty(\text{theory})= 12\%$, $\eta_\infty(\text{expt})= 10\%$. Non resonant depth resolution $\Delta z_{\text{FWHM}} \sim 120\mu\text{m}$. Resonant depth resolution $\Delta z_{\text{FWHM}} \sim 10\mu\text{m}$	172
7-1	General schematic of volume holographic imaging. (a) The volume grating is the recorded 3D interference pattern of two mutually coherent beams (b) The imaging step consists of reading out the volume hologram by an unknown object illumination. The volume hologram diffracts only the Bragg matched components of the object illumination. This effect is used in conjunction with scanning to recover the object illumination.	174
A-1	Volume diffraction geometry.	180

List of Tables

2.1	Measured intensity values for stand alone PR VHI (a.u).	83
2.2	Ratios of intensity values calculated from Table 2.1.	83
2.3	Measured intensity values for PR VHI with telephoto system (a.u). .	83
2.4	Ratios of intensity values calculated from Table 2.3.	83

Chapter 1

Introduction

Imaging [1, 2] remains one of the major applications of optical science. The rapid proliferation of CCD cameras and the availability of ample digital computing power to process the images from these cameras has led to the development of “computational” imaging systems. A computational imaging system (CIS) [3, 4] comprises two kinds of elements:

1. *Analog or Field transforming elements* receive emitted or scattered radiation from an object of interest, and optically transform this radiation. Common field-transforming elements are lenses, apertures, wave plates etc.
2. *Digital or Intensity transforming elements* capture the radiation transformed by the field-transforming elements as an electronic signal on a photoelectric detector or detector array. This signal can then be transformed by digital processing to recover object attributes such as spatial structure, spectral composition, etc.

Thus, computational imaging involves a series of transformations on the information received by the CIS until the information acquires a form that an end user can comprehend. These transformations are effected by both the analog and digital elements of the CIS. As a result of this, it is no longer necessary for the field-transforming elements to produce “images” that are physically analogous to the imaged objects. All that is required is ensure that the detector captures sufficient information to allow the recovery of the objects after appropriate processing operations.

Traditional optical imaging systems, such as photographic cameras, microscopes, telescopes and projection lenses are composed of an “optical train,” *i.e.* several lenses in succession. The role of the lenses is to transform the optical field such that the resulting field distribution at the image plane meets the functional requirements of the system. For example, in traditional photographic imaging the goal is to create a projection of a three dimensional (3D) field onto a two dimensional (2D) receptor plane (photosensitive film or digital sampling plane). Within the constraints of projective geometry, the 2D image is intended to be geometrically similar to the original 3D object.

This thesis describes a new kind of optical field transforming element: a volume holographic lens [5, 6]. The volume holographic lens is a pre-recorded volume hologram [7] that is incorporated into the optical train in addition to the other traditional lenses that are already present in the train. The traditional refractive lenses perform simple 2D processing operations on the optical field [2] as it passes through the optical train and is incident on the volume holographic lens. The volume holographic lens processes the optical field in 3D on account of its thickness [8]. The field diffracted by the volume holographic lens is measured to obtain the specific information that is sought about the optical field. The unique properties of volume holographic lenses make it possible to recover 3D spatial data about an object of interest easily with a little additional processing of the measured data. It is even possible to acquire spectral information (*i.e.* absorption or fluorescence) separately from each point in 3D space, thus increasing the total number of image dimensions to four.

We will show that the three dimensional nature of the volume holographic lens allows sufficient degrees of freedom to customize the volume hologram based imaging system for a wide range of applications. Thus, the analysis and design of volume hologram based imaging systems forms the core of this thesis.

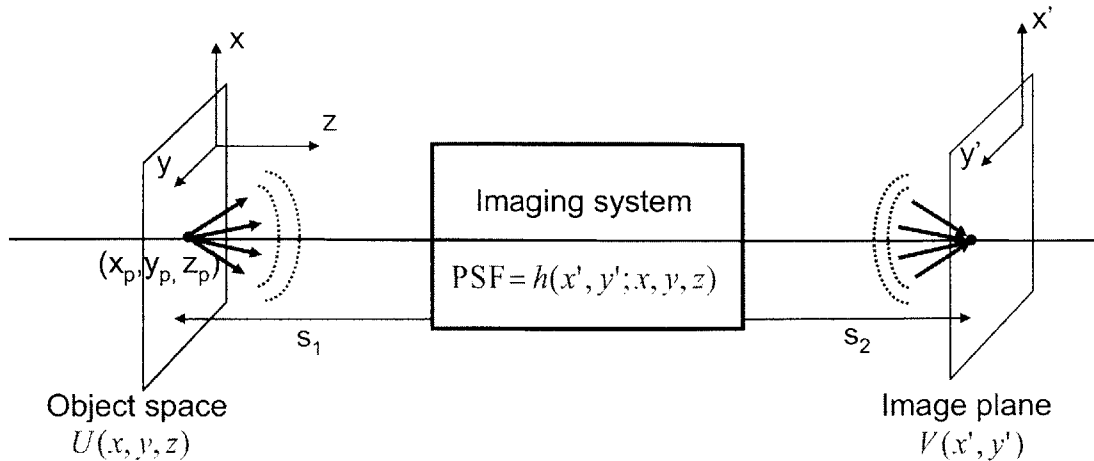


Figure 1-1: Imaging system schematic

1.1 Fundamentals of Imaging Systems

Figure 1-1 depicts the schematic of a generic imaging system. In most cases, the object space is three dimensional with point sources located throughout the 3D object space. Radiation from these sources serves the input to the imaging system. However, for a single-shot imaging system, the detector space is restricted to be planar because the photographic film/photoelectric detector array that captures the output of the imaging system can only be two dimensional.

The imaging system is completely described by its impulse response. The impulse response is a 5D function $h(x', y'; x, y, z)$ that relates the 2D output image $V(x', y')$ to the 3D input $U(x, y, z)$. The form of $h(x', y'; x, y, z)$ depends on the nature of the illumination. Spatially coherent illumination involves a linear superposition of electric fields whereas quasi-monochromatic spatially incoherent illumination results in a linear superposition of object intensities. The transfer functions in these cases are related through an autocorrelation function [9]. Partially coherent illumination involves more complicated relationships in between the coherence properties of the object and image fields. We will not discuss partial coherence here and will instead confine our discussion to coherent imaging systems. In this case, the output field is related to the input field through a Fredholm integral equation [1] of the 1st kind or

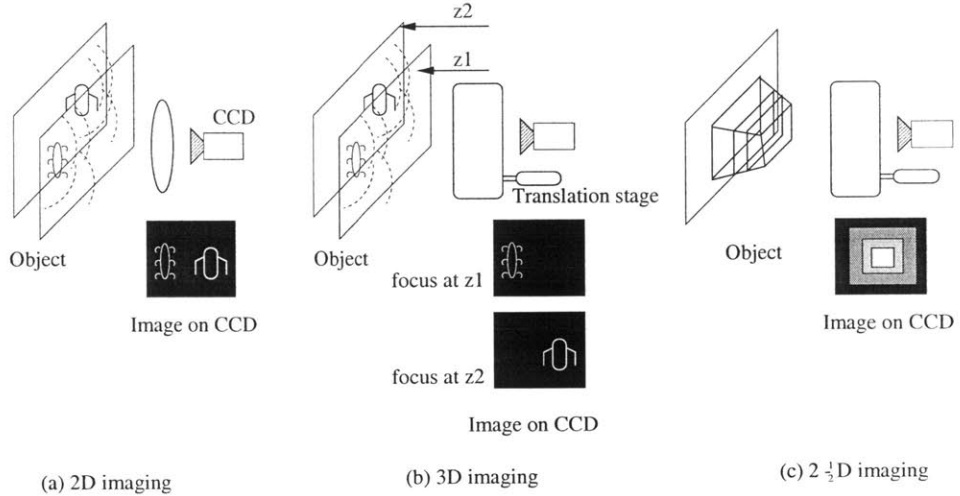


Figure 1-2: (a) A 2D imaging system can not discriminate the distance between two objects; (b) a 3D imaging system can recover depth information by scanning and (c) a $2\frac{1}{2}$ D imaging system maps the height of a reflective surface to an intensity on the detector.

simply put, the linear superposition integral

$$V(x', y') = \iiint h(x', y'; x, y, z)U(x, y, z)dx dy dz. \quad (1.1)$$

Equation 1.1 describes the image formation step of the imaging system *i.e.* if the input $U(x, y, z)$ and impulse response $h(x', y'; x, y, z)$ are known accurately, it is possible to calculate the output image $V(x', y')$. Imaging is the solution to the inverse problem of (1.1). In other words, imaging tries to answer the question:

Given a known imaging system $h(x', y'; x, y, z)$ and a measured image $V(x', y')$, what is the input object $U(x, y, z)$ that created this image?

This problem is ill posed especially since the object is 3D whereas the image is only 2D. Before we analyze this problem further, we classify various classes of imaging systems in the next section.

1.1.1 Classification of Imaging Systems

In most cases, we will focus on imaging systems that recover the spatial structure from objects of interest, so we classify imaging systems of relevance as:

1. *2D imaging systems* typically recover only the 2D brightness or intensity information about an object as shown in Fig. 1-2(a). In other words, a 2D image is of the form $I(x, y)$, an intensity distribution defined over the lateral co-ordinates. Photographic cameras and traditional microscopes are examples of 2D imaging systems.

2. *3D imaging systems* recover the entire 3D intensity information about the object, as shown in Fig. 1-2(b). 3D imaging requires that the object be at least translucent. Thus, a 3D image is of the form $I(x, y, z)$, *i.e.* a complete three dimensional intensity distribution. Fluorescence confocal microscopy [10] and optical coherence tomography (OCT) [11] are examples of 3D imaging methods. Another class of 3D imaging systems are referred to as “tomographic,” e.g. like X-ray computerized tomography (CT) and magnetic resonance imaging (MRI) [12]. In the latter, the object information is retrieved as a set of projections through the object, and Radon transform inversion techniques map the information back to native object coordinates. Typically, 3D imaging systems require scanning in at least one dimension to obtain the complete 3D image.

3. $2\frac{1}{2}D$ *imaging systems*, [13] sometimes also referred to as profilometers, are typically used for reflective objects. The profilometer returns a height map $z(x, y)$ representing the distance of a particular point on the surface from a fixed base as shown in Fig. 1-2(c). This location of fixed base depends on the imaging system being used; for a confocal microscope, it lies at the common focus of the object and collector lenses. Confocal microscopes [14] and interferometers such as the Twyman–Green and the Mach–Zehnder are common non-contact optical profilometers. Heterodyne and white light interferometers can yield accuracy as good as a few nanometers in the axial z direction, but their lateral resolution is limited to a few microns typically. The recently developed methods of Atomic Force Microscopy (AFM) [15] and Scanning Tunnelling Microscopy (STM) [16] extend profilometry to nanoscale accuracies in all three dimensions.

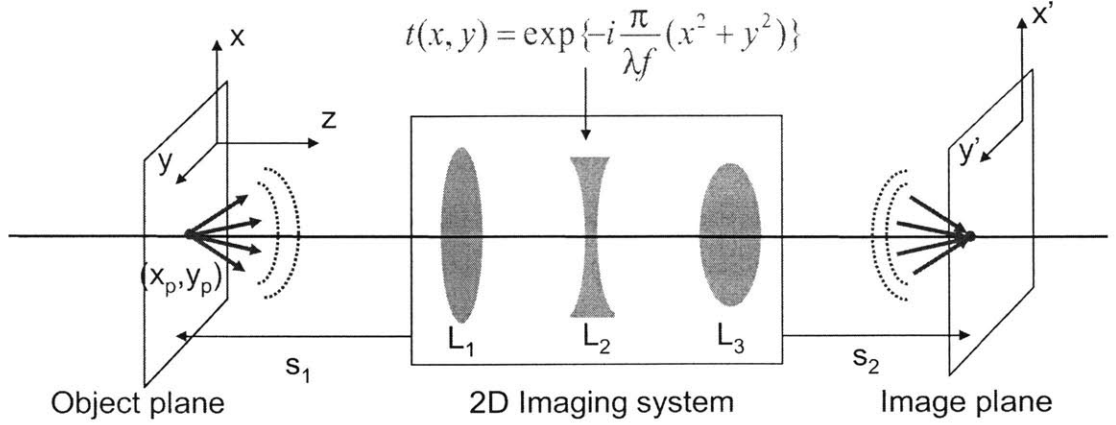


Figure 1-3: Imaging system schematic

Most profilometers also require scanning to recover a complete height map.

1.1.2 Analysis of 2D Lens-Based Imaging Systems

Figure 1-3 shows a simplified 2D imaging system. As mentioned in section 1.1.1, the lens only maps light from a 2D object plane $U(x, y)$ to the image plane $V(x', y')$. The mapping is done through the impulse response of the monochromatic, aberration-free lens based imaging system [2] as

$$V(x', y') = \iint h(x' - x, y' - y)U(x, y)dx dy. \quad (1.2)$$

Note that (1.2) is simply a 2D convolution of the input 2D object $U(x, y)$ with the lens impulse response

$$h(u, v) = \mathcal{F}\{P(x, y)\}_{\frac{x'}{\lambda s_2}, \frac{y'}{\lambda s_2}}. \quad (1.3)$$

In (1.3), $\mathcal{F}\{\cdot\}$ denotes the 2D Fourier transform of the function $P(x, y)$ which represents the aperture of the lens-based imaging system, λ is the wavelength of the light used. The shift-invariant impulse response of the lens-based imaging system ensures that it can form sharp images of objects over a large field of view (FOV) [17]. However, this also implies that the lens-based imaging system has little or no ability to resolve 3D object features [18] without further processing/filtering of the image to

recover some depth cues.

In the next section, we discuss the working of some commonly used 3D imaging systems.

1.1.3 Filtering Methods Used in Lens-Based 3D Imaging

As mentioned earlier, a simple 2D transform based imaging system can not recover depth information without further processing of the image data. The methods developed to recover depth information involve physical gating/filtering of the image prior to detection or digital post-processing of image data or a combination of both.

The confocal microscope [14] operates by obtaining point measurements and constructs a 3D image by scanning the volume of the specimen. Thus the emitted intensity values are recovered one point at a time. The geometry of the optical system is such only that light emitted locally from a very small portion of the object is allowed to reach the detector. The rest of the light is rejected by the detector pinhole. The proportional light contribution to a single measurement as function of object coordinates is equivalent to the 3D point-spread function (PSF) of the system; it can be calculated accurately under various aberration conditions using Fourier optics [19, 20]. Confocal microscopy has been implemented in many different variants for improved light efficiency or resolution, e.g. differential interference [21], fluorescence [22], two-photon [23], etc.; it has been spectacularly successful, primarily in various applications of biological and biomedical imaging.

Coherence imaging is an example of 3D imaging that relies on global, rather than local, measurements. It is based on a fundamental result, derived independently by van Cittert and Zernicke [24, 25], which states that the degree of statistical correlation of the optical field in the far zone, expressed as a complex function over the exit pupil of the imaging system, is the Fourier transform of the object intensity distribution. Therefore, the object can be recovered by measuring the coherence function through interferometry, and then inverse-Fourier transforming the result. The application of the van Cittert-Zernicke theorem in the radio frequency spectral region is the basis of radio astronomy [26], which yields by far the most accurate images of remote cosmic

objects. The most common formulation of the theorem relates the mutual coherence in a plane at infinity to a two-dimensional source intensity distribution, but extensions to 3D sources have been derived by various authors [27, 28, 29, 30]. The far-field version of the extended van Cittert-Zernicke theorem was recently implemented experimentally [31, 32, 33]. A full generalization of the theorem has also been developed and experimentally implemented to allow Fresnel zone reconstruction in projective coordinates [34]. In most coherence imaging systems, the main role of optical measurement is to “fold” the field in order to generate a self-interference pattern which maps the field auto-correlation onto the intensity detector [34, 35, 36].

Optical coherence tomography [11] is an interesting hybrid between confocal microscopy and coherence imaging. It uses field decorrelation due to decoherence to achieve depth slicing (in the confocal microscope, the slicing function is performed by the pinhole). An extension, spectroscopic optical coherence tomography [37] exploits the phase information in the recorded fringes to extract in addition the spectral composition of the object through a Fourier transform. Both Confocal microscopy and optical coherence tomography are excellent for imaging thick (with thickness \sim few μm) specimens such as tissue and other semi-transparent materials.

Extended depth of field imaging with the use of cubic phase masks [38, 39] aims to completely eliminate the effect of the 3rd dimension on $2D$ imaging. Because of this property, we classify the cubic phase mask method as 3D imaging even though it produces images that lack depth information. The cubic phase mask “scrambles” the optical field thereby forming a strongly blurred intensity image in the focal plane. Application of the inverse de-blurring digital transform leads to recovery of the object(s) in the input field with relative insensitivity to their depth. Cubic phase mask based imaging is appropriate for digital photography applications, where defocus-free 2D projections of 3D objects are sufficient, but it can be combined with scanning to return $2 + 1/2D$ data as well. [39]

Laser radar [40] systems use heterodyne detection of a pulsed signal to estimate the depth of the object, the lateral structure is recovered by 2D scanning. Depth information can also be recovered from 2D lens images by using digital post-processing

algorithms like depth-from-defocus [41], depth-from-shading [42, 43] etc. Often multiple lens-based cameras are used in conjunction with triangulation reconstruction schemes to recover 3D object information [44]. Similarly, Radon transform tomographers [45] acquire depth information by reconciling multiple perspectives using the Fourier slice theorem.

Thus, we see that the underlying feature in recovery of 3D object information is processing of image data (either prior to or post image acquisition) and scanning to recover 3D object information. In the next section, we discuss 3D optical information processing for imaging and describe optical elements that can perform these operations.

1.2 Imaging Using 3D Optical Elements

In section 1.1, we saw that the dimensional mismatch between the 3D object space and 2D image plane led to an ill-posed inverse problem for 3D imaging. Further, in section 1.1.2, we saw that the stand alone 2D processing of a lens-based imaging system was insufficient to recover depth information and that some additional processing (optical/digital) was always required. As we saw in section 1.1.3, this is often done by sampling the object several times and capturing multiple 2D images which are then combined to recover 3D object information.

We propose to use volume (3D) optical elements as optical imaging elements. The most general 3D optical element is a volume \mathcal{V} with a three dimensional modulation of the dielectric constant $\epsilon(x, y, z) = n(x, y, z) + i\alpha(x, y, z)$ [46]. $n(x, y, z)$ represents the 3D refractive index modulation inside the volume and $\alpha(x, y, z)$ represents the modulation of the absorption coefficient. We will restrict our attention to 3D optical elements with $\alpha(x, y, z) = 0$ *i.e.* volume elements with only refractive index modulation. We refer to these elements as 3D diffractive optical elements or more simply volume holograms [7]¹ (3D optical elements in which $n(x, y, z) = 0$ are called 3D reference structures [47]). Volume holograms can be thought of as self-aligned 3D stacks

¹A volume hologram is a 3D modulation of the refractive index that rides on carrier $e^{i\vec{K}_0 \cdot \vec{r}}$

of diffractive elements operating on the incident field coherently as it propagates through.

We have chosen to use volume holograms as optical imaging elements for one main reason: A volume element provides a larger number of degrees of freedom in defining the optical response, compared to a surface element (e.g., a thin hologram or a thin lens) of the same aperture. This is intuitively obvious from dimensional arguments, and was proven formally in [48, 49] using the modal properties of electromagnetic fields. We will not repeat the formal arguments here, but point out the desirable and undesirable features of volume holography that should be taken into account in the design process. The main price to pay for the advanced design flexibility is that the control problem of defining the hologram response (*i.e.*, “programming” the volume hologram) becomes considerably more difficult, and is accomplished at the expense of diffraction efficiency [49]. One interesting consequence of the degrees of freedom afforded by volume holograms is that the shift invariance of these elements can be limited in at least one dimension. This is a useful property for 3D imaging systems, e.g. the optical sectioning ability of confocal microscopes can be thought of as resulting from the shift variance of the pinhole response [18].

1.2.1 Volume Holographic Imaging (VHI)

Gabor originally proposed the use of holography as an imaging method to recover both the amplitude and phase of light coming from an object [50] with the intent of using the phase to store and reconstruct 3D information about the object. A Gabor or Leith–Upatnieks [51] hologram is recorded in a thin photosensitive material as the interference pattern between a reference beam and the light scattered by the object. Both analog [52] and digital [53, 54] holograms have been used extensively for 3D and $2\frac{1}{2}$ imaging. Fig. 1-4(a) is a simplified holographic imaging setup; auxiliary optical elements such as lenses have been omitted. It is possible to recover the amplitude and perform optical slicing of the object by probing the hologram optically by scanning, or digitally as shown in Fig. 1-4(b). Analog holography requires recording a fresh hologram for each object and then optically reconstructing them slice-by-slice. Dig-

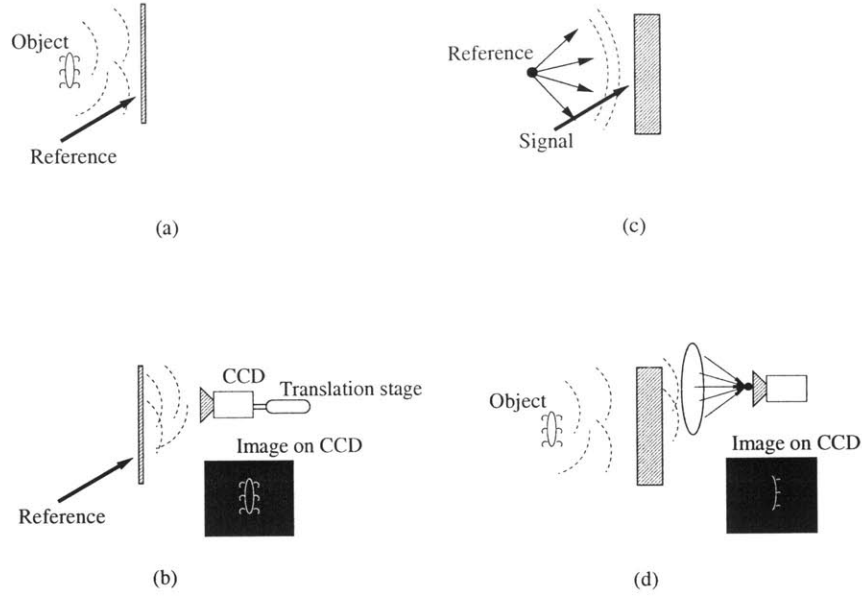


Figure 1-4: Simplified schematics of traditional holographic imaging (a) Recording (b) Readout by scanning. Schematics of volume holographic imaging (VHI) (c) Making VH lens (d) Readout.

ital holography does not require frame by frame holographic recording, but it does require a deconvolution operation for each frame recorded by the camera. Holographic interferometry [55] and two wavelength interferometry [56, 57] are commonly used in imaging systems where the hologram does not function as a fixed imaging element, but rather as a sophisticated detector that captures phase properties of the object. Further, Bertero and collaborators [58, 59, 60, 61, 62, 63, 64] have proposed a method of superresolving confocal microscopy using diffractive elements calculated based on singular system theory.

We discuss a different imaging principle which we call volume holographic imaging (VHI). VHI can be used for both 3D and $2\frac{1}{2}$ D imaging. VHI is different from traditional holographic imaging because:

1. A VHI system incorporates at least one thick holographic element, a volume hologram (VH). The volume hologram (which is also referred to as the volume holographic lens) acts as depth selective imaging element to achieve 3D or $2\frac{1}{2}$ D imaging.

2. A single VH lens can be used to image arbitrary objects on a digital camera. Thus, there is no need to record a new hologram for each object as in the case of analog holographic imaging.

The image, *i.e.* the 3D or $2\frac{1}{2}$ D spatial structure of the object, is recovered from the intensity data recorded on the camera. This computational aspect of the VHI approach can be particularly simple, basically in the form of a “shuffle” map between intensity measurements and spatial coordinates. More sophisticated computational methods employing over-constraining and deconvolutions can also be applied to VHI, which we discuss later.

Volume holographic gratings were first introduced by van Heerden [7]. Since then, the properties of these “thick” diffractive elements have been studied extensively [65, 66]. Volume holograms have been used in several sub-areas of optical information processing, namely data storage [65, 67, 68, 69], optical interconnects [70], artificial neural networks [71, 72, 73] and communication [74, 75, 76, 77, 78]. Prior to the spectacular improvement of VLSI technology in the 1990’s [79, 80], volume holograms were considered as a primary contender for the efficient storage and implementation of the massive interconnections needed for complex pattern recognition tasks.

The use of volume holograms as imaging elements has only been proposed recently [5], and demonstrated in the context of a confocal microscope with a volume hologram replacing the pinhole [81], a volume hologram long range surface profilometer [82, 83], and a real-time (scan-free) hyperspectral imaging instrument [84], a volume holographic spectrometer [85] etc.

A volume hologram is created by recording the interference pattern of reference and signal beams within the entire volume of a “thick” photosensitive material [86]. For example, Figure 1-4(c) depicts a volume hologram recorded by a point source reference and plane wave signal. Holograms that are sufficiently thick [8] are very sensitive to the nature of the illumination and diffract only when the input field matches the recording conditions. For an arbitrary object illumination, as shown in Figure 1-4(d), the volume hologram diffracts only the so called Bragg matched portions of the incident field. Thus the observer sees only a part of the entire ob-

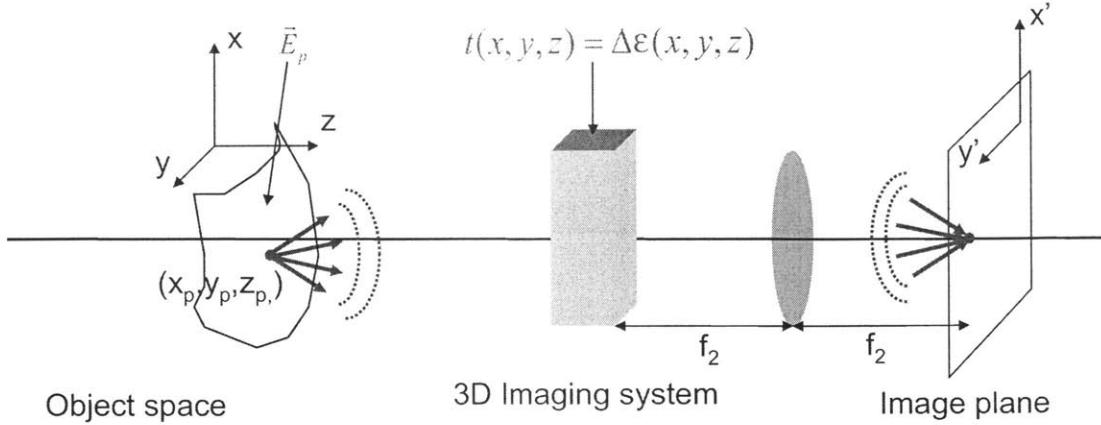


Figure 1-5: Generic volume hologram based imaging system.

ject on the detector. We exploit this property in VHI to resolve depth ambiguities and thus get $2\frac{1}{2}$ D and 3D images. The entire object information is recovered by scanning or multiplexing several holograms to probe different portions of the object simultaneously [84].

To understand how volume holograms can serve as imaging elements, we first briefly review diffraction from volume (3D) holograms. A hologram is 3D if it diffracts in the Bragg regime (as opposed to the Raman–Nath regime of thin holograms [8]). An important property of the Bragg regime that is useful for VHI application is the phenomenon of *Bragg selectivity*. A volume hologram is recorded as usual by use of two mutually coherent beams, the reference and signal. The holographic material thickness must exceed a certain threshold, which depends on the fringe spacing and wavelength of the interference pattern [8].

Figure 1-5 shows the schematic of generic volume hologram based imaging system. The volume hologram with dielectric modulation $\Delta\epsilon(x, y, z)$ is read out by a probe field $\mathbf{E}_p(x, y, z)$ emitting at wavelength λ . The field diffracted by the hologram is Fourier transformed by a lens of focal length f_2 before it is captured on the detector plane (x', y') .

We use the first Born approximation and scalar volume diffraction theory (Refer to Appendix A) to calculate field $\mathbf{E}_d(x', y')$ diffracted by the volume hologram when it is read out by the probe $\mathbf{E}_p(x, y, z)$. The result of the calculation after few simplifications

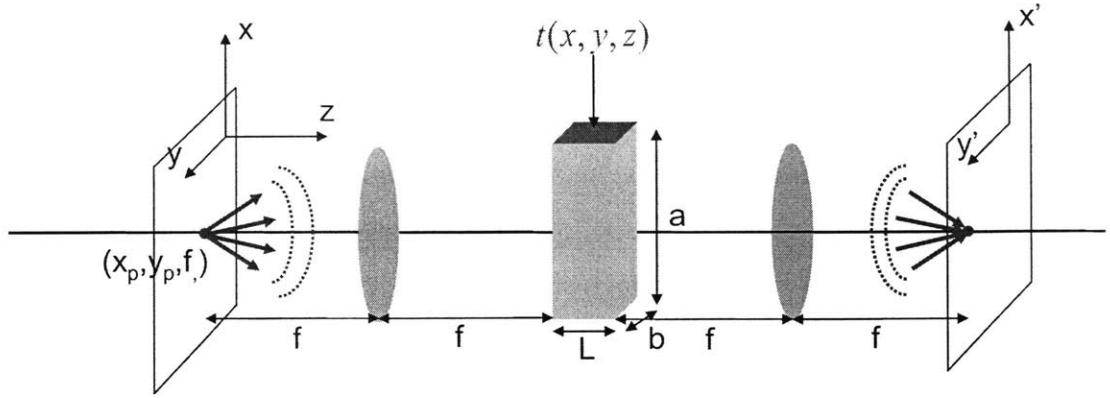


Figure 1-6: Volume holographic imaging system using the 4F geometry.

is

$$\mathbf{E}_d(x', y') = \mathcal{G} \left\{ \frac{x'}{\lambda f_2}, \frac{y'}{\lambda f_2}, \frac{1}{\lambda} \left(1 - \frac{x'^2 + y'^2}{2f_2^2} \right) \right\}. \quad (1.4)$$

In (1.4),

$$\mathcal{G}(u, v, w) = \mathcal{F} \{ \mathbf{E}_p(x, y, z) \times \Delta\epsilon(x, y, z) \} \quad (1.5)$$

is the 3D Fourier transform of the product of the probe field and the dielectric index modulation. Note that the field on the detector plane is shift variant, as evident from (1.4). The shift variance suggests that it is possible for volume holograms to directly image in 3D [18] without further processing of the image data. We will discuss this in greater detail in the next section.

1.2.2 Impulse Response of Volume Holographic Lens with Baseband Modulation

Figure 1-6 is the schematic of simplified volume holographic imaging system. An objective lens of focal length f_1 is placed at a distance f_1 in front of the volume hologram which only has a low frequency (baseband) modulation $\Delta\epsilon(x, y, z)$. The volume hologram is parallelepiped with dimensions $a \times b \times L$ as shown in the figure. For simplicity, we set $f_1 = f_2 = f$ for the 4F optical system. For a input point located

at (x_p, y_p, f) , the response at the detector plane can be calculated using (1.4) to be

$$\begin{aligned} \mathbf{E}_d(x', y') = & \text{sinc}\left(\frac{a(x' - x_p)}{\lambda f}\right) \text{sinc}\left(\frac{b(y' - y_p)}{\lambda f}\right) \text{sinc}\left(\frac{L}{2\lambda f^2}(x_p^2 + y_p^2 - x'^2 - y'^2)\right) \\ & \otimes \Delta\tilde{\epsilon}\left(\frac{a(x' - x_p)}{\lambda f}, \frac{b(y' - y_p)}{\lambda f}, \frac{L}{2\lambda f^2}(x_p^2 + y_p^2 - x'^2 - y'^2)\right). \end{aligned} \quad (1.6)$$

In (1.6), $\tilde{\epsilon}(u, v, w)$ is the 3D Fourier transform of the dielectric modulation $\Delta\epsilon(x, y, z)$ and \otimes represents a convolution operation. From (1.6), we see that the shift variance of the $\tilde{\epsilon}(u, v, w)$ term results in a different response for each set of input points (x_p, y_p, f) . Thus, it should be possible to perform 3D imaging based on the shift variance.

1.2.3 Impulse Response of Volume Holographic Lens with Carrier Frequency

Consider Fig. 1-6 again, except this time the volume hologram is modulated on a carrier wave grating vector \mathbf{K}_g . In other words, the dielectric modulation is $\Delta\epsilon(x, y, z)e^{i\mathbf{K}_g \cdot \mathbf{r}}$. All other parameters are the same as those described in section 1.2.2. For simplicity we define a grating vector written by two beams a normally incident plane wave and another plane wave inclined at an angle θ_s with respect to the normal. The grating vector is

$$\mathbf{K}_g = \frac{i2\pi}{\lambda} \left(\hat{\mathbf{x}}\theta_s - \hat{\mathbf{z}}\frac{\theta_s^2}{2} \right). \quad (1.7)$$

Again, for a input point located at (x_p, y_p, f) , the response at the detector plane can be calculated using (1.4) to be

$$\begin{aligned} \mathbf{E}_d(x', y') = & \text{sinc}\left(\frac{a(x' - x_p - \theta_s f)}{\lambda f}\right) \text{sinc}\left(\frac{b(y' - y_p)}{\lambda f}\right) \\ & \text{sinc}\left(\frac{L}{2\lambda f^2}(x_p^2 + y_p^2 + (\theta_s f)^2 - x'^2 - y'^2)\right) \\ & \otimes \Delta\tilde{\epsilon}\left(\frac{a(x' - x_p - \theta_s f)}{\lambda f}, \frac{b(y' - y_p)}{\lambda f}, \frac{L}{2\lambda f^2}(x_p^2 + y_p^2 + (\theta_s f)^2 - x'^2 - y'^2)\right). \end{aligned} \quad (1.8)$$

The $\text{sinc}(\cdot)$ term on the second line of (1.8) represents the Bragg selectivity of the volume hologram with a carrier. The Bragg selectivity makes the response of the VHI

system even more shift *variant* and helps reject out of focus or Bragg mismatched light efficiently. This allows carrier volume holograms to perform 3D imaging very efficiently.

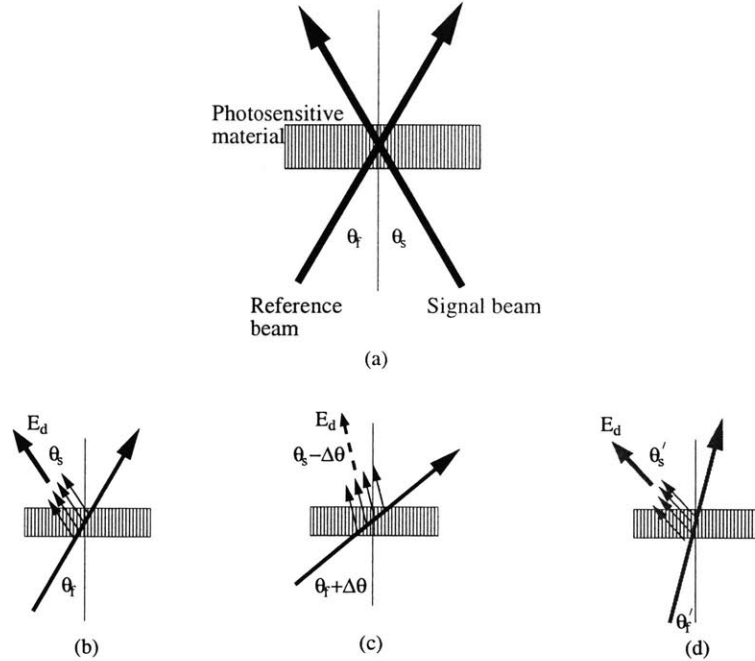


Figure 1-7: Bragg selectivity of volume holograms, (a) Recording; (b) Bragg matched readout using a replica of the reference beam; (c) Bragg mismatched readout results in a weak diffracted field; (d) A Bragg degenerate beam yields a strong diffracted beam. The Bragg degenerate beam is of different wavelength and is incident at a different reference angle governed by Bragg selectivity.

To better understand Bragg selectivity, suppose that a volume hologram is recorded with a certain reference beam and a signal beam. After recording is complete, we probe the hologram with a third beam. Depending on the relationship of the probe beam to the reference beam, we can obtain three types of diffraction:

1. *Bragg matched*, where the probe beam is an exact replica of the reference beam, as shown in Fig. 1-7(b). In this case, the full diffraction efficiency of the recorded hologram is recovered.
2. *Bragg mismatched*, where the probe beam differs from the reference beam. For example, the probe beam could have a different angle of incidence or wave-

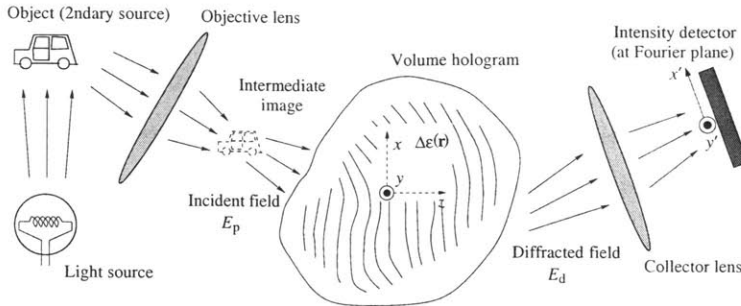


Figure 1-8: Schematic of VHI system. A CCD camera monitors the diffracted beam to detect the whether the light scattered by the object contains any Bragg matched and/or Bragg degenerate components.)

length [65] or location (for a spherical reference [87]) etc. For a Bragg mismatched probe, which is not degenerate (see below) the hologram does not diffract at all or at least the diffraction efficiency obtained from the hologram is much weaker than the Bragg matched case. This is shown in Figure 1-7(c).

3. *Bragg degenerate* diffraction is obtained for a special class of probe beams that differ from the reference beam yet still give rise to strong diffraction, of magnitude comparable to the Bragg matched case. For volume holograms recorded with a plane wave reference, degenerate diffraction can be obtained by either a combined change in wavelength and angle of a plane wave probe, as shown in Figure 1-7(d) [88, 89] or by tilting the probe beam in a direction along the orientation of the fringes that constitute the volume hologram [65, 86]. Generally, degenerate diffraction occurs if the probe beam can be obtained from the reference beam via a transformation which is invariant with respect to the orientation of the interference pattern that constitutes the hologram. The degeneracy property is exploited extensively to reduce the scanning required for VHI, as we discuss later.

We aim to use the Bragg selectivity of volume holographic gratings for depth-selective imaging systems with reflective objects. The general geometry of the imaging system is shown in Figure 1-8. When light scattered from an object contains a component that Bragg matches or is Bragg degenerate for the hologram, some

diffraction is obtained, and so it is possible to detect the presence of Bragg matched and Bragg degenerate object illumination by monitoring the diffracted field. On the other hand, portions of the object which are Bragg mismatched are “invisible” to the VHI system. Thus, we can perform optical slicing, similar to a confocal microscope using the Bragg diffraction as the depth-sensitive component in the system.

A major portion of this thesis is devoted to the characterization of image quality that can be obtained from VHI systems in terms of the point-spread function (PSF) in different geometries. In the literature, there is some confusion about the definition of the PSF. When the imaging system can be adequately modelled as a linear transformation from a 2D object (input) space to a 2D image (output) space, the PSF is interpreted as the impulse response of the imaging system, *i.e.* the intensity pattern observed at the output of an imaging system in response to a point source input. This definition can, in principle, be used for $2\frac{1}{2}$ D or 3D imaging systems as well, provided that the output space is defined accordingly. We are more interested in the response of the VHI system measured on a single pixel detector or a 2D detector array (camera). Thus, we have to deal with the definition of the PSF when the output space has a lower dimension than the input space. To resolve this problem, we interpret the PSF as the intensity response of the VHI system to displacement of the input point source (the “probe” source) away from a reference location. The reference location is specified during the recording step of the VH lens. A similar situation occurs in confocal microscopy, except then the reference location is specified by the focus of the illumination beam, which is also arranged to be conjugate of the pinhole used in front of the detector.

For instance, the depth resolution of the system is obtained from the PSF as follows: we first obtain the intensity measured at the detector plane of the VHI system as function of axial probe displacement, theoretically or experimentally. Then we estimate the extent of the PSF which tells us roughly how far two objects can be placed apart in the longitudinal direction and still be resolved by our imaging system. This definition ignores the noise present in the imaging system, but still provides an adequate measure for comparison of alternative systems (a system with more extended

PSF will perform worse than an alternative with narrower PSF under identical noise conditions.) We elected to use the full width at half maximum (FWHM) of the PSF, denoted as Δz_{FWHM} , for comparisons of resolution. We will discuss this in greater detail in the chapters that follow.

1.3 Outline of this Thesis

We start by developing the theoretical framework for volume holographic imaging systems in Chapter 2 based on the Born approximation (Refer to Appendix A). We focus on transmission volume holograms and two especially simple imaging geometries: VHI using spherical and planar reference beams (SR-VHI and PR-VHI). We adopt the following procedure: First, we derive the diffracted field for a Bragg mismatched probe, then we calculate the resolution of the setup and discuss how the design of objective optics to enhance the resolution further. Finally, we present experimental validation of the theory. In section 2.4 and onwards, we focus only on PR-VHI and present the theory when VHI is done with broadband illumination and again verify the theoretical predictions experimentally.

In Chapter 3, we discuss means to enhance the depth resolution for systems with long working distances under conditions of broadband illumination using N -ocular VHI. We focus on two particular classes of objects: Surface profilometry of remote $2\frac{1}{2}$ objects in section 3.2.1 and 3D imaging of volume scatterers in section 3.2.2.

We have designed and built several VHI systems for a wide variety of applications. In Chapter 4, we classify and discuss VHI systems that we built. These systems range from a high resolution long range surface profilometer to a hyperspectral scan-free microscope with superior imaging performance. This chapter presents a glimpse of the immense flexibility offered by VHI in designing application-specific imaging systems.

In Chapter 5, we compare VHI with other systems that are currently used for these applications. Specifically, we focus on comparison between a telescopic-VHI and a binocular camera in terms of the depth resolution in section 5.1. We also compare the information carrying capacity of a VHI based microscope and a pinhole based

confocal microscope in section 5.2. We show that volume holograms that possess sufficient diffraction efficiency can always outperform a confocal microscope. Thus low diffraction efficiencies would pose a significant hurdle to widespread acceptance of VHI.

We present a solution to the limited diffraction efficiency problem in Chapter 6. We discuss an all optical method that utilizes a resonant optical cavity to enhance the diffraction efficiency of a volume hologram. We call this method Resonant volume holography. We demonstrate some resonant volume holographic systems and then present some preliminary theoretical analysis and experimental results of imaging using resonant volume holographic system in sections 6.2 and 6.3.

We conclude in Chapter 7 by summarizing the major benefits and drawbacks of VHI systems. We discuss some promising directions for future work in this field.

Chapter 2

Volume Holographic Imaging Fundamentals

In this chapter, we present the theory of volume holographic imaging systems. A volume holographic lens is manufactured by recording a three-dimensional interference pattern of two (or more) mutually coherent beams as shown in Fig. 2-1(a). The recording is independent of the object to be imaged, although the selection of the type of hologram to be recorded (e.g. the type of reference beam) can be based prior information about the *type* of objects to be imaged (e.g. the average working distance, reflective vs. fluorescent, etc.). Simple recording schemes include interfering a spherical reference (SR) or planar reference (PR) beam with a planar signal beam to record holograms in the transmission, reflection or 90° geometry [5]. After recording is complete, the hologram is fixed; no further processing is done on the hologram (just like the fixed lenses in an imaging instrument after they are ground and polished). Despite the apparent simplicity of recording, these holograms offer unique imaging capabilities that are not available in traditional lenses.

During imaging, the recorded holograms are probed by the incident illumination as shown in Fig. 2-1(b). If an SR hologram is used, the imaging system is referred to as SR-VHI. Similarly, PR-VHI refers to a system that contains a planar reference volume hologram. The hologram diffracts the Bragg matched [8, 65] components of the incident illumination. The diffracted field is monitored by a detector or a detector

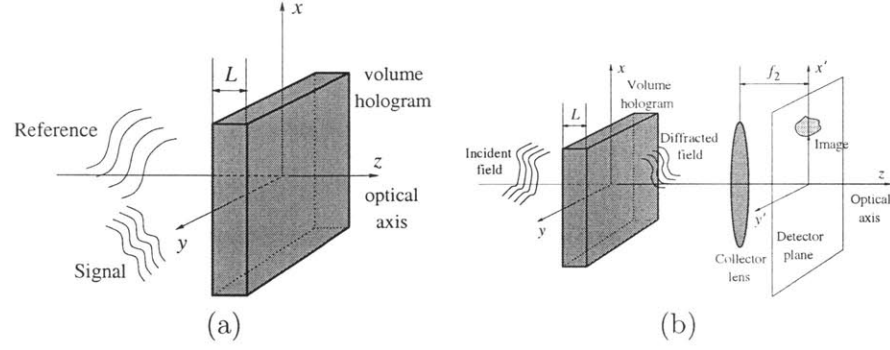


Figure 2-1: General schematic of volume holographic imaging. (a) The volume grating is the recorded 3D interference pattern of two mutually coherent beams (b) The imaging step consists of reading out the volume hologram by an unknown object illumination. The volume hologram diffracts only the Bragg matched components of the object illumination. This effect is used in conjunction with scanning to recover the object illumination.

array. The diffracted field intensity captured by the detector is the “image” formed by the VHI system and can be used to determine the required object information like the 3D spatial and/or spectral characteristics of the object of interest. We will examine SR-VHI and PR-VHI systems in detail for the rest of this chapter [90].

2.1 Spherical Reference Volume Holographic Imaging (SR-VHI)

2.1.1 Derivation and properties of the diffracted field

Fig. 2-2(a) shows the recording setup for VHI using spherical reference (SR-VHI). In this analysis, we will use a coordinate system centered on the hologram, as shown in the Figure. Thus, all wavelengths and angles are measured inside the holographic medium. The corresponding free space values can be obtained by multiplying with the average refractive index n of the medium.

The volume hologram is the stored 3D interference pattern of the point source reference emanating at $\mathbf{r}_f = x_f\hat{\mathbf{x}} + y_f\hat{\mathbf{y}} + z_f\hat{\mathbf{z}}$ and the plane wave signal inclined at an angle $\theta_s \ll 1$ with respect to the $\hat{\mathbf{z}}$ -axis. The holographic medium is disk-shaped

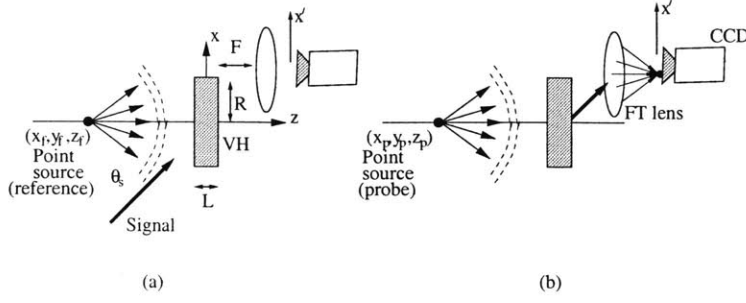


Figure 2-2: Spherical wave reference VHI, (a) Recording and (b) Readout(imaging).

with thickness L and radius R . The origin of the spherical reference is the “reference depth” at which the holographic imaging system operates during readout. As shown in Fig. 2-2(b), the field diffracted by the volume hologram is Fourier transformed by a lens of focal length F , assumed to have infinite lateral extent. The Fourier-transformed diffracted field is observed on a detector or a detector array (eg. CCD or CMOS camera). As mentioned in section 1.2.3, we use the FWHM of the PSF in the longitudinal direction as a metric of the system’s axial resolving capability. Thus, our first task is to calculate and experimentally verify the dependence of the PSF on system parameters. To this end, we idealize the object as a point source located at $\mathbf{r}_p = x_p \hat{\mathbf{x}} + y_p \hat{\mathbf{y}} + z_p \hat{\mathbf{z}}$ and explicitly calculate the diffracted field produced on the detector by this point source.

In the paraxial approximation, the reference beam can be expressed as

$$\mathbf{E}_f(\mathbf{r}) = \exp \left\{ i2\pi \frac{z - z_f}{\lambda} + i\pi \frac{(x - x_f)^2 + (y - y_f)^2}{\lambda(z - z_f)} \right\}. \quad (2.1)$$

Note that here and in the sequel we neglect a term of the form $1/\lambda(z - z_f)$ because it varies with z much slower than the exponential term. The signal beam is expressed in the paraxial approximation as

$$\mathbf{E}_s(\mathbf{r}) = \exp \left\{ i2\pi \left(1 - \frac{\theta_s^2}{2} \right) \frac{z}{\lambda} + i2\pi \theta_s \frac{x}{\lambda} \right\}. \quad (2.2)$$

After recording is complete, the index modulation recorded in the hologram is

$$\Delta\epsilon(\mathbf{r}) \propto \mathbf{E}_f^*(\mathbf{r})\mathbf{E}_s(\mathbf{r}), \quad (2.3)$$

where the “*” denotes complex conjugate. The actual interference pattern is given by $|\mathbf{E}_f + \mathbf{E}_s|^2$, but out of the four resulting product terms only the one in (2.3) results in significant diffraction; the remaining three terms are Bragg-mismatched. Suppose that the hologram is illuminated by a probe field $\mathbf{E}_p(\mathbf{r})$. Since we know the refractive index modulation of the volume hologram from Eq. 2.3, we can calculate the light diffracted by the volume hologram in response to $\mathbf{E}_p(\mathbf{r})$ approximately by (Refer to Appendix A)

$$\mathbf{E}_d(\mathbf{r}'') = \sqrt{\eta} \int \mathbf{E}_p(\mathbf{r}) \Delta\epsilon(\mathbf{r}) G(\mathbf{r}'' - \mathbf{r}) d^3\mathbf{r}, \quad (2.4)$$

where η is the diffraction efficiency, $G(\mathbf{r})$ is Green’s function for free space

$$G(\mathbf{r}'' - \mathbf{r}) = \frac{e^{ik|\mathbf{r}'' - \mathbf{r}|}}{|\mathbf{r}'' - \mathbf{r}|} \approx \exp \left\{ i2\pi \frac{z'' - z}{\lambda} + i\pi \frac{(x'' - x)^2 + (y'' - y)^2}{\lambda(z'' - z)} \right\}, \quad (2.5)$$

and $\mathbf{r}'' \equiv (x'', y'')$ is the position vector on the exit face of the hologram. The result gives the diffracted field as the superposition of fields scattered by individual point radiators such that the radiation generated at each point is proportional (in amplitude and phase) to the product of the illuminating field and the local index modulation. This approximation, known as 1st-order Born scattering, neglects re-diffraction of the scattered field as it propagates through the volume hologram. The approximation is valid only if the hologram is relatively weak (in practice, it works well for η up to 50% or higher, depending on the specific modulation and thickness of the hologram). The spherical probe beam emanating at \mathbf{r}_p is expressed in the paraxial approximation as

$$\mathbf{E}_p(\mathbf{r}) = \exp \left\{ i2\pi \frac{z - z_p}{\lambda} + i\pi \frac{(x - x_p)^2 + (y - y_p)^2}{\lambda(z - z_p)} \right\}. \quad (2.6)$$

The diffracted field at the detector plane is obtained by substituting expressions (2.1), (2.2), (2.3) and (2.6) in (2.4) and performing a Fourier transformation with

conjugate coordinates $(x'', y'') \equiv (x'/\lambda F, y'/\lambda F)$ where (x', y') are the coordinates on the detector plane. The details of the calculation are given in [86, pp. 38-42]. The result after omitting some constant phase factors is

$$\mathbf{E}_d(x', y') = 2\pi R^2 \sqrt{\eta} \int_{-L/2}^{L/2} \exp\{i\pi C(z)\} \mathcal{L}(2\pi A(z)R^2, 2\pi B(z)R) dz. \quad (2.7)$$

The coefficients $A(z)$, $B_x(z)$, $B_y(z)$, $C(z)$ are given by

$$A(z) = \frac{1}{\lambda(z - z_f)} - \frac{1}{\lambda(z - z_p)}; \quad (2.8)$$

$$B_x(z) = -\frac{x_p}{\lambda(z - z_p)} + \frac{x_f}{\lambda(z - z_f)} - \frac{x'}{\lambda F} + \frac{\theta_s}{\lambda}; \quad (2.9)$$

$$B_y(z) = -\frac{y_p}{\lambda(z - z_p)} + \frac{y_f}{\lambda(z - z_f)} - \frac{y'}{\lambda F}; \quad (2.10)$$

$$B(z) = \sqrt{B_x(z)^2 + B_y(z)^2}; \quad (2.11)$$

$$C(z) = \frac{x_p^2 + y_p^2}{\lambda(z - z_p)} - \frac{x_f^2 + y_f^2}{\lambda(z - z_f)} + \left(\frac{x'^2 + y'^2}{\lambda F^2} - \frac{\theta_s^2}{\lambda} \right) z. \quad (2.12)$$

The function

$$\mathcal{L}(u, v) = \int_0^1 \exp\left\{-\frac{i}{2}u\rho^2\right\} J_0(v\rho)\rho d\rho \quad (2.13)$$

also occurs in the calculation of the 3D light distribution near the focus of a lens [1]. It is the Hankel transform of the radial quadratic chirp $\exp(-iu\rho^2/2)$ truncated to $0 < \rho \leq 1$. We compute this integral as a series expansion given in Ref. [1], although faster approximate methods have been suggested in the literature [91]. Eq. 2.7 describes the action of the volume holographic filter as an imaging element with a spherical wave reference. The PSF of the volume hologram is obtained by calculating the total diffracted field intensity

$$\left| \mathbf{E}_d(x', y'; x_p, y_p, z_p) \right|^2,$$

which is a function of the location of the probing point source and the observation location at the detector plane. For simplicity, we consider a hologram recorded and probed with an on-axis point source *i.e.*, $x_f, y_f, x_p, y_p = 0$. Eq. 2.7 is further simplified by setting $z_p - z_f = \delta$ and assuming $L/z_p \ll 1$. Replacing these in (2.8)–(2.11)

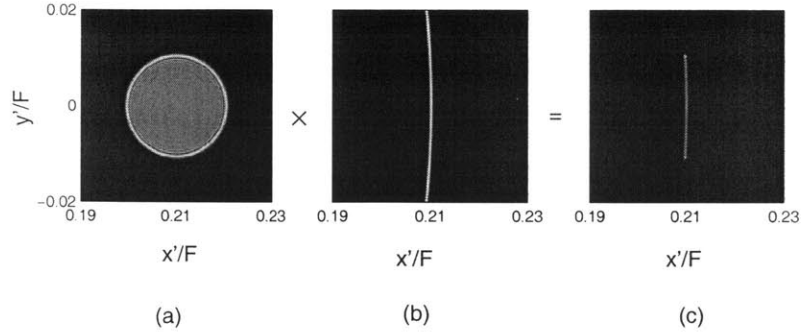


Figure 2-3: Intensity pattern observed on the detector for spherical VHI for (NA)=0.07, $\theta_s = 12^\circ$ (0.21 rad) and $\delta = 6$ mm. (a) Diffraction pattern caused by axial defocus, (b) Crescent shaped Bragg filter of SR hologram, (c) Diffracted pattern observed on the detector.

and (2.12) and carrying out the integration yields an approximate expression for the normalized diffracted field intensity,

$$\frac{I(x', y'; \delta)}{I_b(\theta_s F, 0; \delta)} = \left| \mathcal{L} \left(\frac{2\pi R^2 \delta}{\lambda z_f^2}, \frac{2\pi R}{\lambda F} \sqrt{(x' - \theta F)^2 + y'^2} \right) \operatorname{sinc} \left(\frac{(x'^2 + y'^2 - (\theta F)^2)L}{2\lambda F^2} \right) \right|^2. \quad (2.14)$$

We chose the normalization constant $I_b \equiv I(x' = \theta_s F, y' = 0)$ because the diffracted intensity peaks at detector location $(x', y') = (\theta_s F, 0)$, as can be seen from (2.9) and (2.10). Eq. 2.14 offers an intuitive explanation for the behavior of this volume holographic optical element. The observed diffracted field contains two contributions, shown in Fig. 2-3:

1. The $\mathcal{L}(\cdot, \cdot)$ term shown in Fig. 2-3(a) is similar to the impulse response of a lens with defocus δ , [1] but with an important difference: The equivalent numerical aperture (NA) is R/z_f in the longitudinal direction and R/F in the lateral. For a normal lens, it would have been R/z_f for both the lateral and longitudinal directions. Since we are primarily interested in the depth selectivity of the VHI

system, we define

$$(\text{NA}) = \frac{R}{z_f}. \quad (2.15)$$

This definition is also intuitively satisfactory from the geometry of the system. For large enough defocus δ , the $\mathcal{L}(\cdot, \cdot)$ term represents an almost uniformly illuminated disk (see Fig. 2-3a) in agreement with geometrical optics. The disk is centered at the Gaussian image point $(x', y') = (\theta_s F, 0)$ where the intensity peaks, as noted earlier.

2. The $\text{sinc}(\cdot)$ term shown in Fig. 2-3(b) peaks along the *degeneracy* circle, which in this geometry is centered at $(0, 0)$ and has radius $F\theta_s$. The thickness of the degeneracy circle is

$$\Delta r' = \frac{2\lambda F}{L\theta_s}. \quad (2.16)$$

This term originates from the Bragg selectivity of the hologram. In the SR VHI system, it serves to reject out of focus light. It is seen that the filter only rejects light in mostly one lateral (\hat{x}) direction near the Gaussian image point; points along the other (\hat{y}) direction are mapped along the arc of the degeneracy circle. This behavior is evidence of the y -degeneracy of the volume hologram. The circular shape of the locus of the degeneracy is due to the curvature of the fringes that constitute the SR VH.

The degeneracy circle due to the $\text{sinc}(\cdot)$ term acts as a mask superimposed on the defocused disk image due to the $\mathcal{L}(\cdot, \cdot)$ term. Together, they result in the crescent-like shape of Figure 2-3(c).

The pinhole in a confocal microscope performs a function similar to the $\text{sinc}(\cdot)$ filter imposed by the hologram. Both reject out of focus light from an object. However, the rejection mechanism is different in the two cases: The pinhole operates as a hard limiter, whereas the hologram is a matched filter with respect to the wavefront of a point source located at the reference depth. An information theoretic comparison of the two systems [92] shows that the matched filter can provide superior image quality despite the limited diffraction efficiency $\eta < 1$ for a line shaped source oriented along

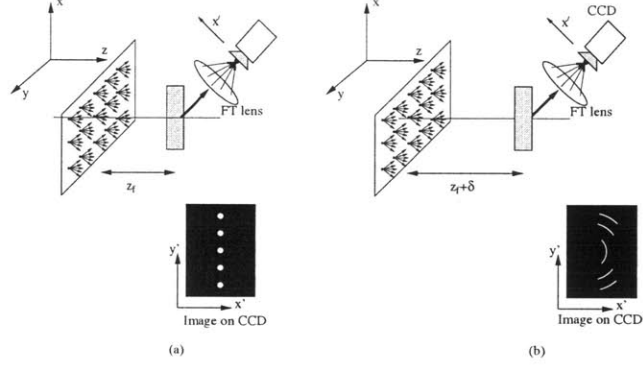


Figure 2-4: VHI is a shift variant imaging system; the observed diffracted field changes with a change in the spatial location of the point source: (a) Mutually incoherent point sources with no defocus, (b) Mutually incoherent point sources with defocus δ .

the \hat{z} axis, and under the assumption of Gaussian noise statistics.

An alternative point of view of the above observations is that depth selectivity results from the shift variance of the volume hologram [18]. Indeed, the SR hologram has shift selectivity; [87] *i.e.*, the diffracted field is Bragg mismatched when the spherical wave probe is displaced in the direction \hat{x} , perpendicular to the recorded fringes, for any value of δ (both in and out of focus). On the other hand, the response of the hologram to a probe displaced by δ_y in the other lateral direction is qualitatively different. If the probe is in focus, *i.e.* $\mathbf{r}_p = (0, \delta_y, z_f)$, the point image is simply displaced to the location $y' = F\delta_y/z_f$. That is, the in-focus system is shift invariant in the \hat{y} direction, within a magnification factor F/z_f . If the probe is located out of focus at $\mathbf{r}_p = (0, \delta_y, z_f + \delta)$, the response is

$$\frac{I(x', y')}{I_b} = \left| \mathcal{L} \left(\frac{2\pi R^2 \delta}{\lambda z_f^2}, \frac{2\pi R}{\lambda F} \sqrt{(x' - \theta_s F)^2 + \left(y' - \frac{F\delta_y}{z_f}\right)^2} \right) \right|^2 \times \text{sinc} \left(\frac{(x'^2 + y'^2 - F^2(\theta_s^2 + \delta_y^2/z_f^2))L}{2\lambda F^2} \right)^2. \quad (2.17)$$

This represents a crescent of radius $F\sqrt{\theta_s^2 + \delta_y^2/z_f^2}$, still centered at $(0, 0)$ as in the on-axis case.

The above discussion can be easily extended to the case when the input field

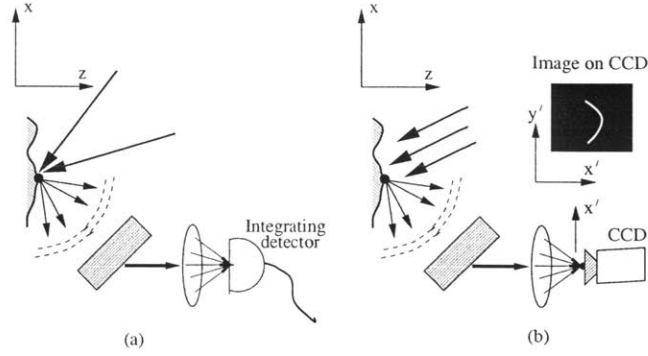


Figure 2-5: VHI methods (a) 3D scanning using an integrating detector and focussed illumination (b) Exploiting y - degeneracy by using a CCD and 2D scanning with extended illumination.

consists of a superposition of mutually incoherent point sources arranged on a plane perpendicular to the \hat{z} axis. When the source plane coincides with the reference plane, $z_p = z_f$ for all the sources, as shown in Figure 2-4(a), only the sources with $x_p \approx 0$ are “visible” to the hologram, and they generate a line of point images oriented along the y' axis of the detector plane. The horizontal coordinate is $x' = \theta_s F$ for all the point images. In the case of a plane out of focus, $z_p = z_f + \delta$, the visible sources still lie on the $x_p \approx 0$ line, but each source is creating its own crescent image on the detector plane, displaced and with different radius as discussed above. The image is the superposition of intensities corresponding to these crescents, as shown in Figure 2-4(b) and experimentally validated for three mutually incoherent points as shown in Fig. 2-12.

2.1.2 Depth resolution

The presence of a masked “defocus” term in (2.14) indicates that SR-VHI can map depth to the intensity of the diffracted field. We describe two methods for exploiting this property to obtain $2\frac{1}{2}$ D or 3D images:

1. *Method 1*: The reflective object is illuminated by focused illumination as shown in Fig. 2-5(a). A large area detector is placed at the Fourier plane of the FT lens and the entire diffracted power is measured. Thus, the object shape is obtained

one voxel at a time. Complete 3D scanning recovers the object in its entirety. In this case, the longitudinal PSF is calculated by integrating (2.14) over the entire detector area

$$I_d(\delta) = \iint_{-\infty}^{\infty} I(x', y') dx' dy'. \quad (2.18)$$

Fig. 2-6 shows theoretical and experimental plots of I_d as a function of defocus

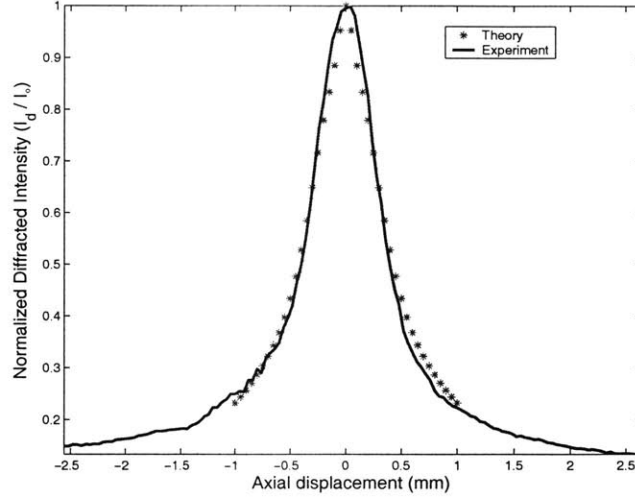


Figure 2-6: Theoretical and experimental plots of longitudinal PSF for SR-VHI.

δ for the case of a single probe point with an integrating detector. We normalize the PSF to the Bragg matched diffracted intensity $I_o = I_d(0)$. In both theory and experiment, we used $NA \approx 0.07$, $R = 3.5$ mm, $z_f = 50$ mm and $\theta_s = 12^\circ$ inside the hologram. The hologram was recorded in a 2 mm thick 0.03% Fe-doped LiNbO_3 crystal. It is seen that $\Delta z_{\text{FWHM}} \approx 800 \mu\text{m}$ for this case.

2. *Method 2:* The reflective object is illuminated by extended monochromatic light as shown in Figure 2-5(b). The y -degeneracy allows the VH to image an entire strip along the degenerate \hat{y} direction. A CCD camera is placed at the Fourier plane of the FT lens to capture the strip. As a result, only 2D scanning is required to recover the entire object. However, from (2.17), it is obvious that each Bragg degenerate point in the \hat{y} direction gives rise to an out of focus crescent. These crescents overlap for adjacent degenerate points,

thus degrading the lateral resolution. One way to compensate is to adaptively estimate the size of the crescent and deconvolve in a way similar to depth-from-defocus techniques [93]. The starting point for this type of estimation is the percentage of power contained in a spot of given size on the detector plane. This is given in Figure 2-7, which plots the radii of the circles confining 95%, 99% and 99.9% of the total diffracted energy for various values of defocus. The complete derivation of the adaptive deconvolution scheme and the derivation of the sensitivity to noise are beyond the scope of this thesis.

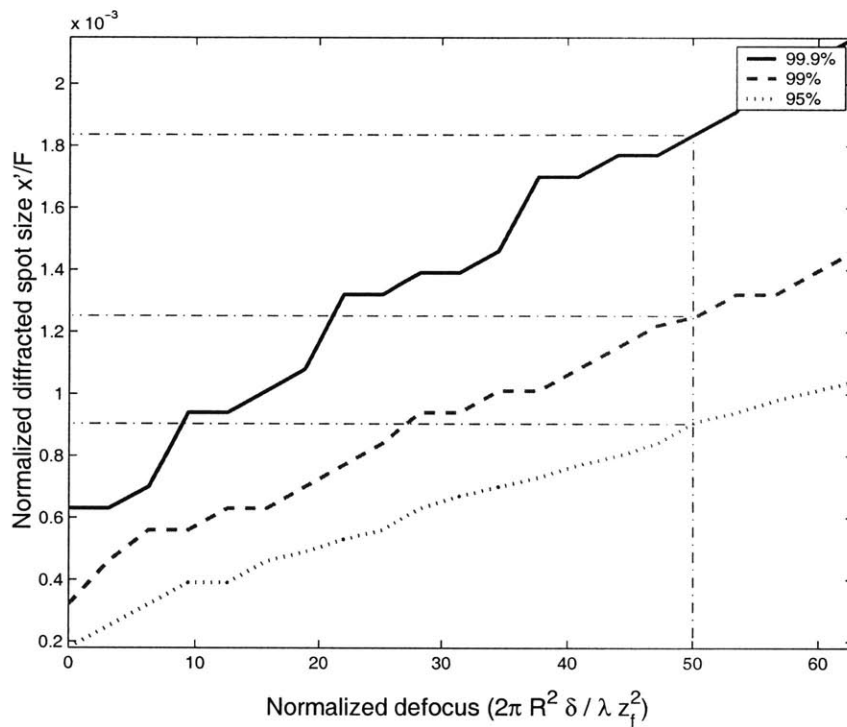


Figure 2-7: Computed contour lines giving the fraction of the total diffracted power which falls within small circles centered at the Bragg matched point versus selected values of the defocus term. Values corresponding to a defocus equal to the FWHM are indicated by the dashed lines.

Returning to the point-by-point method 1 using an integrating detector, which appears to be the most practical, we now estimate the depth resolution as the Δz_{FWHM} from the PSF. The most interesting aspect of this calculation is the dependence of

the Δz_{FWHM} on the distance z_f between the reference plane and the optical system, in other words the “working distance” of the imaging system. The scaling factor in the defocus term of (2.14) and the crescent width term of (2.16) suggest a dependence of the form

$$\Delta z_{\text{FWHM}}(\text{SR}) = \frac{G_{\text{SR}} \lambda z_f^2}{R^2 L}, \quad (2.19)$$

or, in terms of the (NA) of the system,

$$\Delta z_{\text{FWHM}}(\text{SR}) = \frac{G_{\text{SR}} \lambda}{(\text{NA})^2 L}. \quad (2.20)$$

In (2.19) and (2.20) the factor G_{SR} depends on the signal beam angle θ_s only. Its value is determined from integration (2.18) and is given in Figure 2-8 as function of θ_s . The result matches well the model

$$G_{\text{SR}} = \frac{18.2}{\theta_s}. \quad (2.21)$$

For the value $\theta_s = 12$ used in the experiment, the theoretical value is $G_{\text{SR}} = 14$ in agreement with our observation.

2.1.3 Design of objective optics

Result (2.19) states that the depth resolution degrades quadratically with working distance. Such behavior is common in image-forming ranging instruments. To get good depth resolution at long working distances, *i.e.* remote objects, we need to use large apertures or thicker holograms; both methods are impractical and expensive. One way of accomplishing that is by use of “objective optics.” We use this term to refer to optical elements which are inserted between the object and the hologram to transform the incoming field and thus improve the working distance or the resolution. For example, the objective optics can simply be a telescope as discussed in section 4.2.3. Here, we discuss the use of objective optics in more general terms.

Consider the two SR-VHI systems shown in Figure 2-9, both of which have the same working distance d . In the system of Figure 2-9(a), the field from the object is

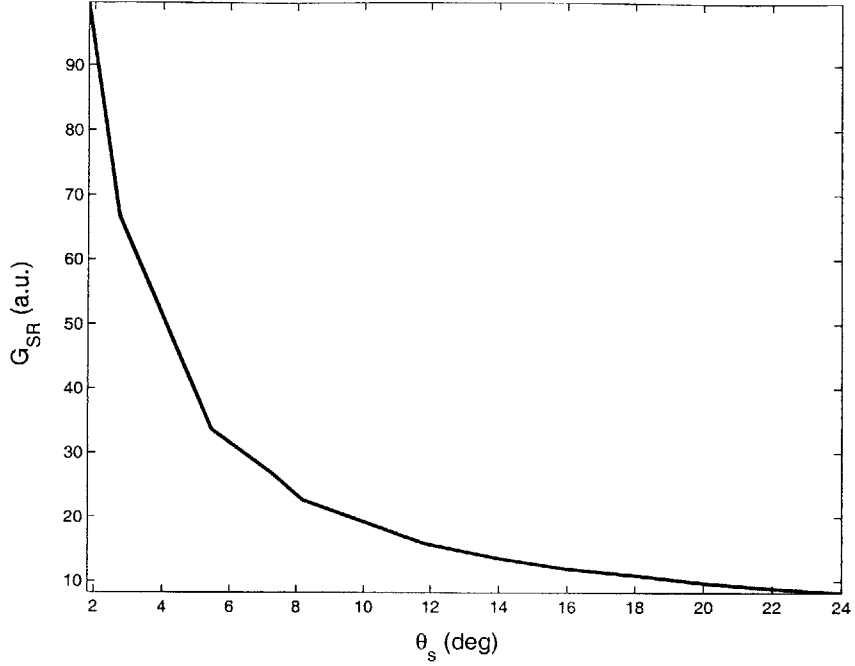


Figure 2-8: Dependence of G_{SR} on θ_s .

directly incident on the hologram; therefore, the reference distance for this case must be $z_f = d$, and the depth resolution in the vicinity of d is given, according to (2.19), by

$$\Delta z_{FWHM}(SR) = \frac{G_{SR} \lambda d^2}{R^2 L}. \quad (2.22)$$

The objective optics in Figure 2-9(b) create an intermediate image of the object in front of the hologram. Let m_1 denote the lateral magnification of the objective optics, and z'_f the new reference distance. We assume that z'_f is chosen such that the diffracted power is maximum when the object is located exactly at d . Now suppose that the object is displaced by δ in the longitudinal direction. The intermediate image is displaced by

$$\delta' = m_1^2 \delta. \quad (2.23)$$

Let a denote the size of the entrance pupil of the combination of the objective optics

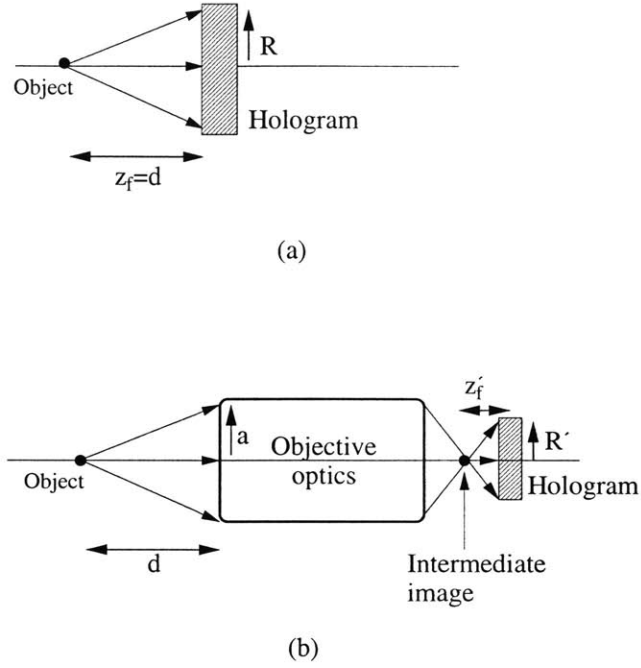


Figure 2-9: SR-VHI systems (a) without objective optics (b) with objective optics in between the hologram and object.

and hologram. The effective numerical aperture of the optical system is then

$$(\text{NA})_{\text{obj}} = \frac{a}{d}. \quad (2.24)$$

However, since the angular magnification of the objective optics is $1/m_1$, the numerical aperture of the field incident on the hologram is

$$(\text{NA}) = \frac{(\text{NA})_{\text{obj}}}{m_1} = \frac{R}{z'_f}. \quad (2.25)$$

From (2.23), (2.25) and (2.20) we can see that the apparent gain (or loss) in numerical aperture due to the magnification of the objective optics is exactly balanced by an equal loss (or gain) in longitudinal displacement of the intermediate image. Therefore, the resolution is

$$\Delta z_{\text{FWHM}}(\text{SR}) = \frac{G_{\text{SR}}\lambda}{(\text{NA})_{\text{obj}}^2 L} = \frac{G_{\text{SR}}\lambda d^2}{a^2 L}. \quad (2.26)$$

It appears that “there is no free lunch” in this case, and the objective optics did not help improve the image quality. However, we did gain one thing: the hologram aperture required to achieve performance as in 2.26 is given by

$$R = |m_1| a, \quad (2.27)$$

according to (2.25). By using demagnifying optics ($|m_1| < 1$) we can utilize a smaller hologram with the system of Figure 2-9(b) than the system of Figure 2-9(a). In most implementations, this is desirable in practice. This is the case in section 4.2.3, where the telescope was acting as demagnifier. The theoretical and experimental PSF dependence on working distance d is given in Figure 2-10.

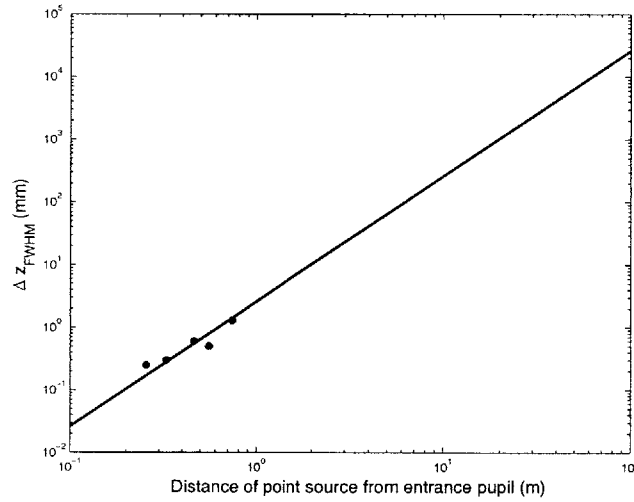


Figure 2-10: Depth resolution Δz_{FWHM} of SR-VHI system degrades quadratically with working distance.

It is worthwhile to mention that a confocal system (CF) with objective optics would also exhibit a similar dependence,

$$\Delta z_{FWHM}(CF) = \frac{G_{CF} \lambda r^2}{d^2}. \quad (2.28)$$

In (2.28), G_{CF} is a factor that depends on the pinhole radius of the confocal system [94].

2.1.4 Experimental validation

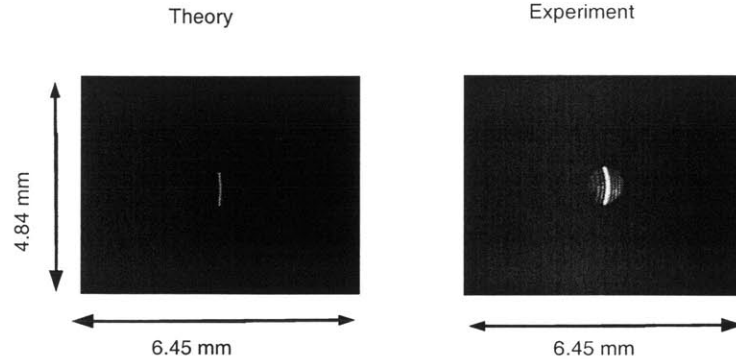


Figure 2-11: Theoretical and experimental diffracted patterns on CCD for SR-VHI with a point source displaced $\delta = 4$ mm from Bragg match.

Figure 2-11 compares the theoretical and experimental diffraction patterns captured on a camera for defocus $\delta = 4$ mm. The volume hologram was recorded with a reference point source located $z_f = 50$ mm away from the center of the hologram and a plane-wave signal beam inclined at angle $\theta_s = 12^\circ$ inside the hologram. The hologram radius was $R = 3.5$ mm, which corresponds to $(NA) \approx 0.07$. The Fourier transforming lens had focal length $F = 63.9$ mm. A doubled Nd:YAG CW laser ($\lambda = 532$ nm) was used for both recording and imaging in this and all subsequent experiments. The typical diffraction efficiency of the hologram was $\eta \approx 5\%$. We used a Jai CV235 industrial CCD camera to capture the diffraction patterns in all experiments. The experimental degeneracy pattern matches well with the theoretical predictions of curvature, spot size and thickness. The experimental strip is slightly thicker on account of saturation of the pixels on the CCD.

Three experimental diffraction patterns obtained from point sources with different y_p were added incoherently and are shown combined in Figure 2-12. This experiment was intended to emulate the incoherent imaging case discussed at the end of section 2.1.1. The experimental setup was identical to the one described in the previous paragraph. The in-focus images obtained with $\delta = 0$ and $\delta_y = -1.5, 0$ and 1.5 mm are shown in Figure 2-12(a) and the out-of-focus images for $\delta = 4$ mm and the same

lateral displacements are shown in Fig. 2-12(b). The crescent radii increase with δ_y , in agreement with the theoretical prediction.

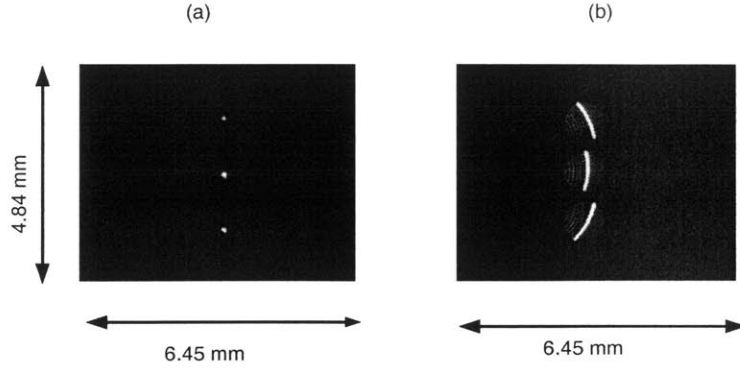


Figure 2-12: Observed diffracted fields on CCD for three mutually incoherent points, (a) Points are at the Bragg matched plane and (b) points are at a defocused plane $\delta = 4$ mm.

2.2 VHI using plane wave reference beams

2.2.1 Derivation and properties of the diffracted field

Fig. 2-13(a) is the recording setup for VHI using planar reference (PR-VHI). The collimating objective lens ensures that the reference beam is approximately a plane wave when it is incident on the hologram. Thus, the front focal length of the objective lens is the reference depth at which the PR-VHI system operates.

During recording, the reference beam is a normally incident plane wave

$$\mathbf{E}_r(\mathbf{r}) = \exp \left\{ i2\pi \frac{z}{\lambda} \right\}. \quad (2.29)$$

The hologram and the Fourier transforming lens are assumed to have infinite lateral extent. L is the thickness of the hologram, f is the focal length of the collimating objective lens and a is its radius. Thus, the NA of the imaging system equals a/f . The focal length of the Fourier transforming lens is F . The signal beam is a plane wave propagating at angle $\theta_s \ll 1$ with respect to the $\hat{\mathbf{z}}$ -axis, just as in the case of

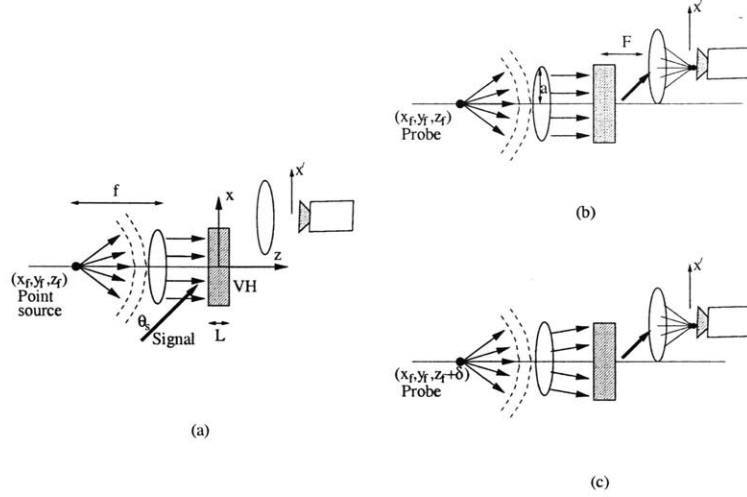


Figure 2-13: Plane wave reference VHI schematic, (a) Recording; (b) Bragg matched readout and (c) Bragg mismatched readout.

SR-VHI. In the paraxial approximation, the signal beam is expressed as

$$\mathbf{E}_s(\mathbf{r}) = \exp \left\{ i2\pi \left(1 - \frac{\theta_s^2}{2} \right) \frac{z}{\lambda} + i2\pi\theta_s \frac{x}{\lambda} \right\}. \quad (2.30)$$

The volume hologram is the recorded 3D interference pattern of the reference and signal beams and it is stored as a weak modulation $\Delta\epsilon(\mathbf{r}) \propto |E_r + E_s|^2$ of the dielectric constant. The Bragg matched term of the modulation is given by

$$\Delta\epsilon(\mathbf{r}) = \exp \left\{ \frac{i2\pi}{\lambda} \left(x\theta_s - z\frac{\theta_s^2}{2} \right) \right\}. \quad (2.31)$$

Fig. 2-13(b) shows the read-out procedure for PR-VHI. A probe point source is placed in front of the objective lens at coordinates $\mathbf{r}_p = (x_p, y_p, z_p)$. First consider the case when the probe is placed at the Bragg matched location $(0, 0, f)$. Then, the objective lens collimates the probe field. As a result, a replica of the reference beam is incident on the hologram. Since the probe is exactly Bragg matched in this case, the volume hologram diffracts a replica of the signal beam, *i.e.* a plane wave propagating in direction θ_s . The Fourier lens placed behind the hologram focuses this diffracted plane wave onto the detector surface. If instead the probe is axially displaced by δ

from the Bragg matched location, the objective lens can no longer collimate the probe field. Instead, the field incident on the hologram is a spherical wave originating at

$$z'_p = \frac{f(f - \delta)}{\delta} \approx \frac{f^2}{\delta} \quad (2.32)$$

for $\delta \ll f$. Only the on-axis Fourier component of this spherical probe is Bragg matched; therefore, the overall intensity diffracted from the hologram is reduced.

We now derive the dependence of the diffracted power on probe displacement δ . According to the observation in the previous paragraph, it is mathematically convenient to express the defocused spherical probe as well as the diffracted field in terms of their plane wave components with wave-vectors \mathbf{k}_p and \mathbf{k}_d , respectively. The “transfer function” [86, ch. 1]

$$\tilde{A}(\mathbf{k}_p, \mathbf{k}_d) = S \int_{\mathcal{V}} \Delta\epsilon(\mathbf{r}) \times \exp\{i(\mathbf{k}_p - \mathbf{k}_d) \cdot \mathbf{r}\} d^3\mathbf{r} \quad (2.33)$$

specifies the spatial spectrum of the hologram response to a single spatial frequency in the input field. In (2.33), S is a constant determined by the polarization and index modulation; our analysis will normalize the diffracted intensities, and so this factor can be ignored. $\tilde{A}(\mathbf{k}_p, \mathbf{k}_d)$ can be interpreted as the 3D Fourier transform of the dielectric constant modulation $\Delta\epsilon$ evaluated at $\mathbf{k}_p - \mathbf{k}_d$. In the more general case where the spatial spectrum of the probe field is given by $\tilde{E}_p(\mathbf{k}_p)$, the spatial spectrum of the diffracted field is obtained from (2.33) as

$$\tilde{E}_d(\mathbf{k}_d) = \iint \tilde{E}_p(\mathbf{k}_p) \tilde{A}(\mathbf{k}_p, \mathbf{k}_d) dk_{px} dk_{py}, \quad (2.34)$$

where k_{px} and k_{py} are the $\hat{\mathbf{x}}$ and $\hat{\mathbf{y}}$ components of the probe wave-vector respectively, while the $\hat{\mathbf{z}}$ component is given by the Bragg constraint $|\mathbf{k}_p| = 2\pi/\lambda$. Since the detector is located at a Fourier transform plane, the diffracted field as function of detector plane coordinates (x', y') is obtained from (2.34) by substituting $k_{dx} = 2\pi x'/\lambda F$, $k_{dy} = 2\pi y'/\lambda F$ for the $\hat{\mathbf{x}}$ and $\hat{\mathbf{y}}$ components of the wave-vector \mathbf{k}_d respectively.

In the specific case of interest, where the probe is a spherical wave, we express its spatial spectrum using Weyl's identity

$$\tilde{E}_p(k_{px}, k_{py}) = \exp \left\{ \frac{iz'_p(k_{px} + k_{py})^2}{2|\mathbf{k}|} \right\}. \quad (2.35)$$

We evaluate the integral (2.33) using (2.31) and then substitute the result of the integral and (2.35) in (2.34) to obtain the diffracted field on the detector plane

$$E_d(x', y') = \exp \left\{ -i\pi \frac{z'_p}{\lambda} \left(\left(\frac{x'}{F} - \theta_s \right)^2 + \left(\frac{y'}{F} \right)^2 \right) \right\} \text{sinc} \left(\frac{L \sin \theta_s}{\lambda} \left(\frac{x'}{F} - \theta_s \right) \right) \quad (2.36)$$

This function is almost zero outside a disk of radius $Fa\delta/f^2$ centered at $x' = \theta_s F$. This disk represents the geometrical image of the aperture of the objective lens on the detector plane. Therefore, the intensity is expressed approximately as

$$\frac{I(x', y')}{I_b} = \text{circ} \left(\frac{\sqrt{(x' - \theta_s F)^2 + y'^2}}{Fa\delta/f^2} \right) \text{sinc}^2 \left(\frac{L \sin \theta_s}{\lambda} \left(\frac{x'}{F} - \theta_s \right) \right), \quad (2.37)$$

where $I_b = I(x' = \theta_s F, y' = 0)$ is the peak intensity produced by the probe. The approximation neglects diffraction ripples at the disk edges; these ripples have negligible effect in practice. Comparing (2.37) and (2.14) suggests that the origin of depth selectivity is similar in the PR and SR implementations of VHI. In the PR case, the diffraction pattern contains two contributions, shown in Figure 2-14:

1. A disk, represented by the $\text{circ}(\cdot)$ function, whose radius is proportional to the defocus δ .
2. A slit oriented along the $\hat{\mathbf{x}}$ (Bragg-selective) direction, represented by the $\text{sinc}^2(\cdot)$ function, whose width is inversely proportional to the hologram thickness L . This term rejects out of focus light because of the Bragg mismatch property.

There are also some significant differences:

1. In the PR case, the disk radius grows linearly with defocus δ , whereas this

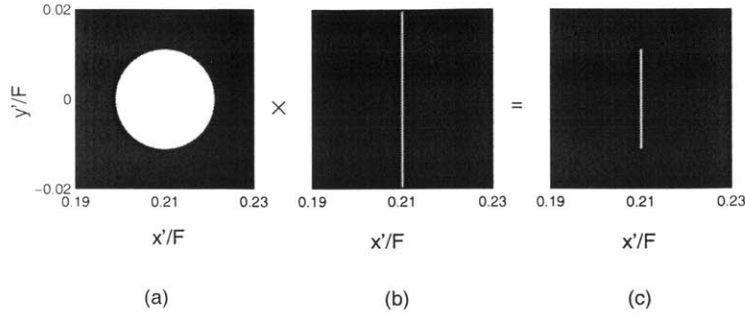


Figure 2-14: Intensity pattern observed on the detector for spherical VHI for $(NA)=0.07$, $\theta_s = 12^\circ$ (0.21 rad) and $\delta = 8$ mm. (a) Diffraction pattern caused by axial defocus and the finite aperture of collimating lens, (b) Straight Bragg slit of PR hologram, (c) Diffracted pattern observed on the detector.

dependence was quadratic in the SR case. We will belabor this point further in connection with the resolution of the two methods.

2. In the PR case, the shape of the Bragg degenerate illumination on the detector plane is a straight slit, consistent with the planar fringes recorded in the hologram. On the other hand, the fringes in SR holograms are curved leading to the crescent-shaped degeneracy.

PR-VHI is also a shift variant imaging system [18] similar to SR-VHI. The PR hologram has angular selectivity; [65] *i.e.*, the diffracted field is Bragg mismatched when the probe source is displaced in the direction \hat{x} , perpendicular to the recorded fringes, for any value of δ_x (both in and out of focus). On the other hand, the response of the hologram to a probe displaced by δ_y in the other lateral direction (\hat{y}) is qualitatively different. If the probe is in focus, *i.e.* $\mathbf{r}_p = (0, \delta_y, f)$, the point image is simply displaced to the location $y' = F\delta_y/f$. That is, the in-focus system is shift invariant within a magnification factor F/f . If the probe is located out of focus at

$\mathbf{r}_p = (0, \delta_y, f + \delta)$, the response is

$$\frac{I(x', y')}{I_b} = \text{circ} \left(\frac{\sqrt{(x' - \theta_s F)^2 + (y' - F\delta_y/f)^2}}{Fa\delta/f^2} \right) \text{sinc}^2 \left(\frac{L \sin \theta_s}{\lambda} \left(\frac{x'}{F} - \theta_s \right) \right). \quad (2.38)$$

This represents a disk masked by the Bragg selectivity slit similar to (2.37), centered at the Gaussian image point $(0, F\delta_y/f)$. The center would be located at $(0, 0)$ for an on axis probe $\delta_y = 0$. From Eq. 2.38, we see that PR-VHI is completely shift invariant in the \hat{y} direction for both in and out-of-focus probe points. This is because SR-VHI has a crescent shaped degeneracy curve whose radius changes with lateral displacement δ_y . On the other hand PR-VHI has a straight line degeneracy, which is independent of lateral displacement δ_y .

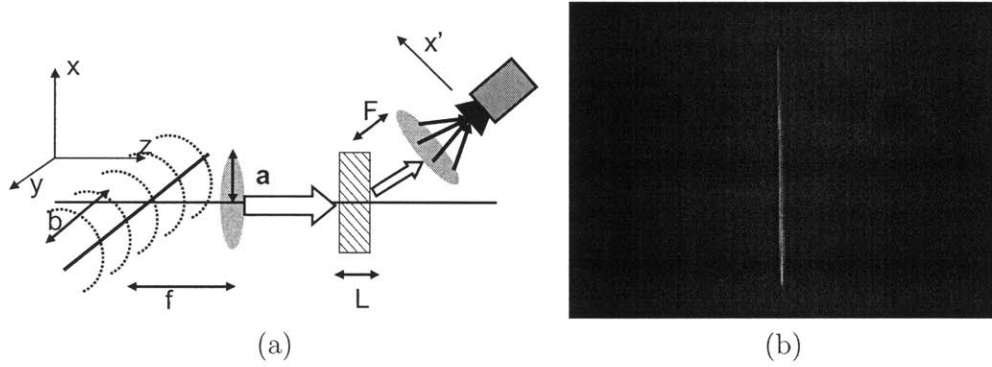


Figure 2-15: PR-VHI using a line source to reduce scanning required (a) Schematic (b) Intensity pattern observed on CCD.

Since the fringes that constitute the PR volume hologram are invariant in the \hat{y} direction of Fig. 2-13, it is possible to image in the PR-VHI geometry using a line source and scanning the object space one line at a time. This reduces the amount of scanning required. For a line source illumination as depicted in Fig. 2-15(a), the diffracted intensity on the CCD can be derived in a manner similar to (2.37). The result is

$$\frac{I(x', y')}{I_b} = \text{rect} \left(\frac{(x' - \theta_s F)}{2Fa\delta/f^2} \right) \text{rect} \left(\frac{y'}{2bF/f} \right) \text{sinc}^2 \left(\frac{L\theta_s}{\lambda} \left(\frac{x'}{F} - \theta_s \right) \right), \quad (2.39)$$

where $I_b = I(x' = \theta_s F, y')$ is the peak intensity produced by the probe. We note that (2.37) is the response to a defocused *point* source whereas (2.39) is the response of a defocused *line* source.

2.2.2 Depth resolution

We now calculate the longitudinal PSF of the PR system with an integrating detector and 3D scanning (method 1 of section 2.1.2). The calculation proceeds as follows: First we integrate the diffracted intensity (2.37) with respect to the detector coordinates (x', y') . Then we normalize to the peak Bragg-matched power I_o received when the probe is in focus. The result is

$$\frac{I_d}{I_o} = \frac{1}{\pi} \int_0^{2\pi} d\phi \int_0^1 d\rho \rho \operatorname{sinc}^2 \left(\frac{aL \sin \theta_s \delta}{\lambda f^2} \rho \sin \phi \right), \quad (2.40)$$

So far, all the derivations were performed using angles, distances and wavelength of light measured inside the holographic material of refractive index n . The corrected PSF for quantities measured in air is

$$\frac{I_d}{I_o} = \frac{1}{\pi} \int_0^{2\pi} d\phi \int_0^1 d\rho \rho \operatorname{sinc}^2 \left(\frac{aL \sin \theta_s \delta}{n\lambda f^2} \rho \sin \phi \right), \quad (2.41)$$

(Note that in the SR case there was no residual n entering the free space formula¹.)

Fig. 2-16 shows theoretical and experimental plots of the PSF as function of defocus δ for $\text{NA} \approx 0.07$, $a = 3.5$ mm, $f = 50.2$ mm and $\theta_s = 12^\circ$ inside the hologram. In both experiment and simulation, the hologram was recorded in a 2mm thick Fe-doped LiNbO_3 crystal ($n \approx 2.2$). Both the experimental and theoretical curves yield a $\Delta z_{\text{FWHM}} \approx 1.7$ mm.

The trend of longitudinal resolution Δz_{FWHM} vs working distance d is computed directly from the PSF expression. In this case, we select the focal length of the objective lens such that $f = d$, and from the scaling factors in the argument of the

¹I would like to thank Wenyang Sun for deriving the PSF in air

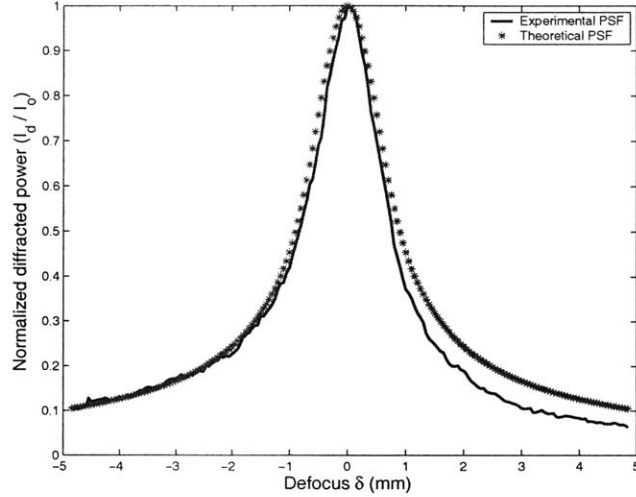


Figure 2-16: Longitudinal PSF for PR-VHI.

integrand in (2.41) we find

$$\Delta z_{\text{FWHM}} = \frac{G_{\text{PR}} \lambda f^2}{aL}, \quad (2.42)$$

where G_{PR} is a factor that depends linearly on θ_s . Numerical regression on (2.41) gives

$$G_{\text{PR}} = \frac{5.34}{\theta_s}. \quad (2.43)$$

It is possible to exploit the straight line degeneracy of PR-VHI and use a CCD camera to acquire information one slit at a time in way similar to method 2 of section 2.1.2. If a reflective object is illuminated by extended monochromatic light as shown in Figure 2-18, the y -degeneracy allows the PR VH to image an entire strip along the degenerate \hat{y} direction.

The depth and lateral resolutions for the line readout follow a trend similar to that observed for a point source readout on account of the similar scaling factors in equations (2.37) and (2.39). However, the depth resolution for the line readout method is poorer than the same optical system with the point readout method. This is shown in Fig. 2-17 which compares the longitudinal PSFs when the same PR-VHI system is probed first with a point and then a line source. A similar degradation is observed in confocal microscopy when the confocal pinhole is replaced by a narrow

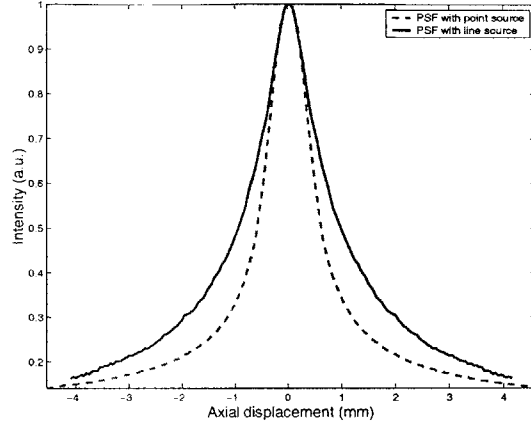


Figure 2-17: Depth resolution degrades slightly when using a line readout as opposed to a point readout. The PR-VHI system had an objective lens with $f = 50.2$ mm and $a = 5$ mm; $\theta_s = 25^\circ$. The volume hologram was 2 mm thick crystal of LiNbO_3 with diffraction efficiency $\eta = 5\%$ recorded using a doubled Nd:YAG laser with $\lambda = 532$ nm.

slit.

As mentioned earlier, PR-VHI is completely shift invariant in the \hat{y} direction unlike SR-VHI, which results in a different crescent for each degenerate point. We now examine two situations and examine which method (SR or PR-VHI) would prove more beneficial.

1. The reflective object shown in Fig. 2-18(a) has surface features of size $\Delta z < \Delta z_{\text{FWHM}}$. In this case, an SR-VHI system would result in an image with several weak crescent shaped defocus blurs and a bright Bragg matched slit. This image can be easily be processed (e.g. by deconvolution or iterative methods) to give an accurate representation of the surface. On the other hand, the PR-VHI system finds it difficult to distinguish between the surfaces because the smaller surface features and the straight degeneracy results in the slit of the out-of-focus surface appearing almost as bright as the slit of Bragg matched surface. Hence, a SR-VHI system employing method 2 is preferred in this case.
2. The reflective object shown in Fig. 2-18(b) has surface features $\Delta z > \Delta z_{\text{FWHM}}$. In this case, the SR-VHI image consists of a thick band of crescents (arising

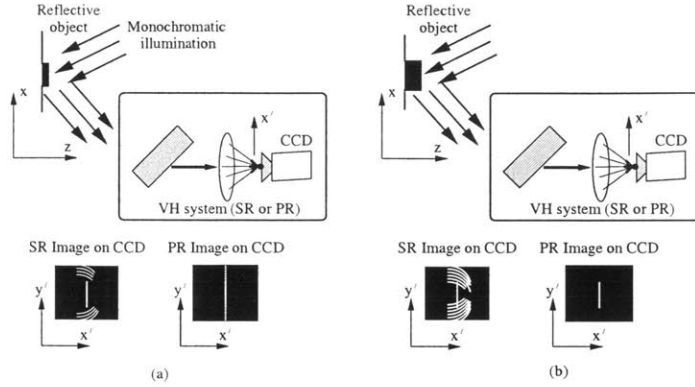


Figure 2-18: VHI by exploiting the y -degeneracy by using a camera at the detector plane (a) Line scanning of object with small surface features (b) Line scanning of object with large surface features.

from the large defocus blur) and the Bragg matched slit. This band makes further image processing and deconvolution very susceptible to noise artifacts. On the other hand, the large surface features ensure that the slit image out-of-focus surface is much fainter than the Bragg matched slit. As a result, it is preferable to use PR-VHI with method 2 in this case.

2.2.3 Design of the objective optics

We now revert back to our discussion on the resolution of PR-VHI employing an integrating detector and discuss whether it is possible to improve depth resolution by appropriate choice of objective optics. From (2.56) we observe that the Δz_{FWHM} of the PR-VHI system varies quadratically with f but only inverse linearly with a . This is a significant difference compared to SR-VHI systems, where the dependence on the physical aperture R of the hologram was inverse quadratic (see eq. 2.19). Below, we show how to design objective optics for the PR case to exploit this property.

Consider the objective optical system shown in Figure 2-19. The first and second principal planes of this system are denoted as PP_1 and PP_2 , respectively. The working distance d is measured between the object and the entrance pupil of the objective optics. The radius of the entrance pupil is a . The effective numerical aperture of the

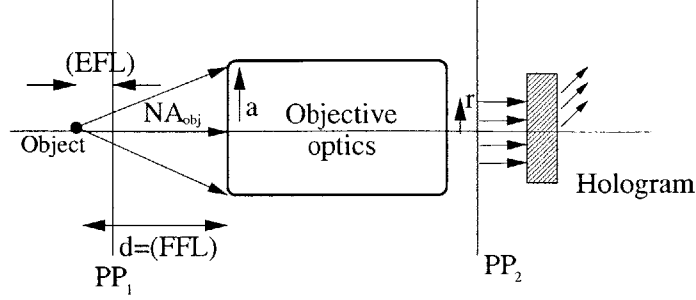


Figure 2-19: Schematic for design of an objective optical system to obtain high depth resolution at large working distances in VHI systems.

optical system is

$$(NA)_{\text{obj}} = \frac{a}{d}, \quad (2.44)$$

which is of course identical to (2.24).

The purpose of the objective optics is to illuminate the hologram with a collimated beam when the object is in-focus, *i.e.* located exactly at d . Therefore, the front focal length (FFL) must be equal to d . Let (EFL) denote the effective focal length of the objective optics, and r the radius of the collimated beam. In the simplest case, the objective optics is a single thin positive lens, as described in sections 2.2.1 and 2.2.2. Then (EFL) = (FFL) = $f = d$ and $r = a$.

For an out-of-focus object, eq. 2.42 can be rewritten in terms of (EFL) and r as

$$\Delta z_{\text{FWHM}}(\text{PR}) = \frac{G_{\text{PR}}(\text{EFL})^2}{r \times L}. \quad (2.45)$$

From Figure 2-19, we see that $r = (NA)_{\text{obj}} \times (\text{EFL})$ which on substitution in (2.45) yields

$$\Delta z_{\text{FWHM}}(\text{PR}) \sim \frac{r}{NA_{\text{obj}}^2 \times L}. \quad (2.46)$$

In terms of the physical apertures, this expression can be rewritten as

$$\Delta z_{\text{FWHM}}(\text{PR}) = \frac{G_{\text{PR}} r d^2}{a^2 \times L} \quad (2.47)$$

This indicates that the quadratic degradation of $\Delta z_{\text{FWHM}}(\text{PR})$ with increasing d

can be offset by reducing the physical size r of the collimated beam illuminating the hologram. Equivalently, this is accomplished by designing the objective optics so that PP_1 is as close to the probe as possible. An example of a standard optical system with this property is a telephoto lens, which is analyzed in detail in the section 2.2.4.

A side-effect of making r arbitrarily small is that the ray bundle exiting the objective optics would cease to behave like a plane wave. To make sure that this does not happen, we need to place a lower bound r_{\min} on r . A reasonable method to calculate the lower bound is to ensure that the spread of the ray bundle due to diffraction beyond the exit pupil and throughout the length L of the hologram remains a small fraction of r itself. This leads to a condition of the form [2]

$$r_{\min} = c\sqrt{\lambda L}, \quad (2.48)$$

where c is selected depending on the amount of diffraction that we are willing to tolerate. For example, in the mid-visible range of wavelengths and for $L = 2\text{mm}$, $r_{\min} \approx 100\mu\text{m}$ ensures less than 5% diffraction.

Replacing (2.48) in (2.47) we find that the best achievable depth resolution $\Delta z_{\text{FWHM}}(\text{PR})_{\text{opt}}$ for PR-VHI varies as

$$\Delta z_{\text{FWHM}}(\text{PR})_{\text{opt}} \frac{G_{\text{PR}} r_{\min} d^2}{a^2 \times L}. \quad (2.49)$$

Therefore, the resolution of the optimized PR-VHI system still degrades quadratically with working distance d , but the objective optics provide a favorable (reduced) constant of proportionality by a factor r_{\min}/a compared to the value without objective optics.

It is also possible to design objective optics for PR-VHI such that the resolution degrades with d at a rate slower than quadratic, e.g. linear or even constant. This is accomplished by using zoom optics in the objective to vary r as function of d . For example, if we maintain $r \propto d^{-1}$ then we obtain $\Delta z_{\text{FWHM}} \sim d$. However, because of the constraint on the minimum allowable r , the sub-quadratic behavior is possible only if we are willing to tolerate $\Delta z_{\text{FWHM}}(\text{PR}) > \Delta z_{\text{FWHM}}(\text{PR})_{\text{opt}}$.

Before we conclude this section, it is worthwhile to summarize the different effect that objective optics have in the SR and PR cases. In the SR case, the objective optics permit the use of a smaller hologram for a given $(NA)_{obj}$ without any inherent gain in longitudinal resolution. In the PR case, the objective optics move the effective focal distance much closer to the object than the actual working distance d . Therefore, resolution is improved by as much as r_{min}/a , where a is the physical aperture of the objective optics and r_{min} , the minimum allowable collimated beam diameter. Immediately below we quantify these differences for the specific case of a PR-VHI system implemented with a telephoto lens.

2.2.4 Design of telephoto objective optics for PR-VHI systems

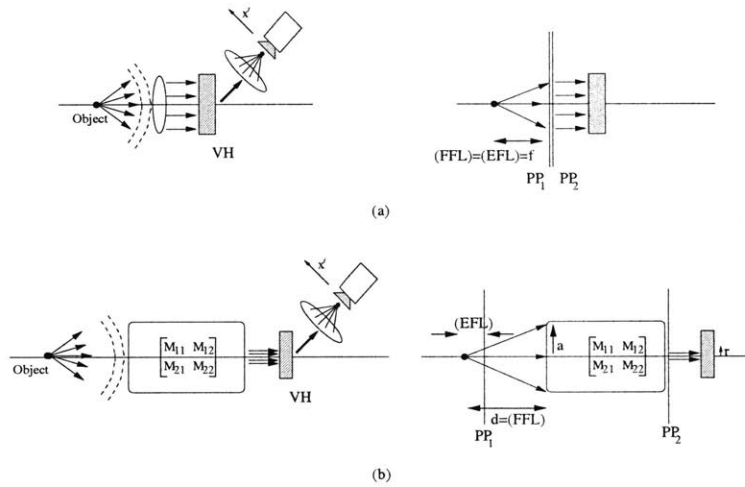


Figure 2-20: Appropriately designed objective optics can improve the Δz_{FWHM} of a PR VHI system. (a) PR VHI schematic without objective optics (b) PR VHI schematic with objective optics.

To analyze objective optical systems, we consider a system similar to the one depicted in Fig. 2-20 and use the generalized ray-tracing matrix representation [17]

$$\underline{\mathbf{M}} = \begin{bmatrix} M_{11} & M_{12} \\ M_{21} & M_{22} \end{bmatrix}. \quad (2.50)$$

The key parameters determining resolution and working distance are then given by

$$M_{12} = -\frac{1}{(\text{EFL})} \quad (2.51)$$

and

$$M_{11} = \frac{(\text{FFL})}{(\text{EFL})}. \quad (2.52)$$

A telephoto system comprises two lenses of focal lengths f_1 , f_2 , with $f_2 < 0$. The lenses are separated by distance t . For the matrix elements M_{11} , M_{12} specified by (2.51-2.52), the focal lengths are selected as

$$f_1 = \frac{M_{11}t}{M_{11} - 1 - M_{12}t} \quad (2.53)$$

$$f_2 = \frac{t}{1 - M_{11}}. \quad (2.54)$$

The separation t is selected to locate PP_2 immediately behind the second lens (otherwise the r_{\min} requirement becomes more stringent.) PP_2 is exactly on the second lens if $t = f_1$, so in practise we select a slightly higher value for t . It should be noted that the same improvement in resolution can be accomplished by use of a demagnifying telescope or other optical systems; yet the telephoto is one of the most compact and widely available implementations.

Fig. 2-21 shows that a telephoto system can be used to increase the working distance without any degradation in the Δz_{FWHM} for PR-VHI. The stand alone PR-VHI system had $(\text{NA})_{\text{obj}} \approx 0.08$ using a collimating objective lens with $d = f = 50$ mm and radius $a = 4$ mm to record the hologram and $\theta_s = 12^\circ$. The telephoto system comprised of two lenses with $f_1 = 250$ mm and $f_2 = -25$ mm separated by a distance $t = 500$ mm. The object was placed at a working distance $d = (\text{FFL}) = 500$ mm in front of the positive lens which had an aperture $a = 12.7$ mm. Thus, for the telephoto system, $(\text{NA})_{\text{obj}} \approx 0.025$. The actual size of the recorded hologram was $r = 2$ mm and $\theta_s = 12^\circ$. It is seen that both PSFs have the same $\Delta z_{\text{FWHM}} \approx 1$ mm despite the fact that the stand alone PR-VHI system has working distance $d = 50$ mm and the telephoto PR-VHI system has a working distance $d = 500$ mm.

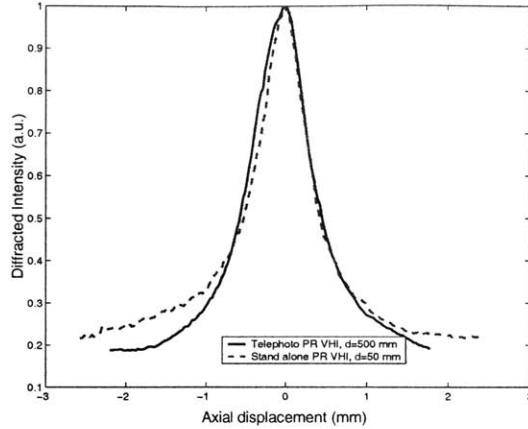


Figure 2-21: An appropriately designed telephoto system can improve working distance d without any degradation in the resolution. PSFs for stand alone PR VHI system (dashed line) and telephoto PR-VHI system (solid line) show that both systems have $\Delta z_{FWHM} \approx 1$ mm for $d = 50$ mm and $d = 500$ mm respectively.

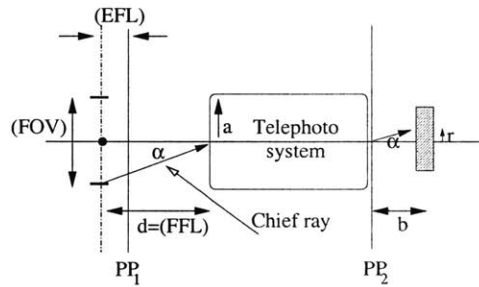


Figure 2-22: Calculation of FOV for telephoto PR VHI system, the chief ray makes an angle α with the optical axis.

For the telephoto system, the hologram must be placed at the the second principal plane PP_2 of the system. When we image using method 2 (line-scan), an additional consideration for the size r of the collimated beam is that it acts as a field stop. To see why, consider Figure 2-22, where the hologram is placed sub-optimally at a distance b behind PP_2 . The field of view (FOV) of this telephoto system is

$$(\text{FOV}) = \frac{2r(\text{EFL})}{b + L}. \quad (2.55)$$

Thus it is beneficial to select b as small as possible to fully utilize the parallelism of

method 2.

2.2.5 Experimental validation

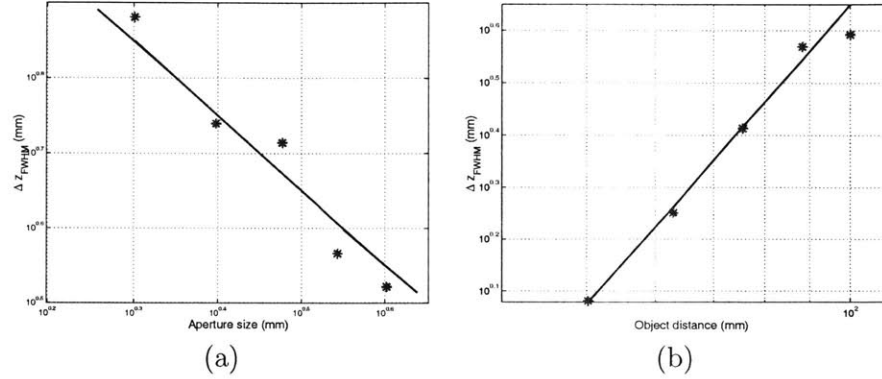


Figure 2-23: (a) Theoretical (solid line) and experimental (crosses) Δz_{FWHM} vs a for fixed f and L , confirming the inversely proportional relationship to (NA) in this case. (b) Theoretical (solid line) and experimental (crosses) Δz_{FWHM} vs f for fixed a and L , confirming the quadratic dependence on f .

We numerically integrated equation (2.41) for different values of a , L and f and fit the numerical data to the equation

$$\Delta z_{FWHM} = \frac{G_{PR}\lambda f^2}{aL}, \quad (2.56)$$

where G_{PR} is a factor that depends linearly on θ_s . For $\theta_s = 13.6^\circ$ (signal beam angle inside the hologram), a least-squares fit yielded $G_{PR} \approx 9.3$. We performed a series of experiments to determine the experimental value of G_{PR} in the identical geometry, and found experimental $G_{PR} = 10.09$ as shown in Figure 2-23. The small disagreement with the theory can be explained due to aberrations in our experimental system that were not accounted for in our paraxial theory.

Fig. 2-24 compares the theoretical and experimental diffraction patterns captured on a camera for a displacement of $\delta = 8$ mm from Bragg match. A collimating objective lens of focal length $f = 50.2$ mm and radius $a = 3.5$ mm was used to record the hologram. The signal beam was inclined at an angle $\theta_s = 12^\circ$ inside the hologram

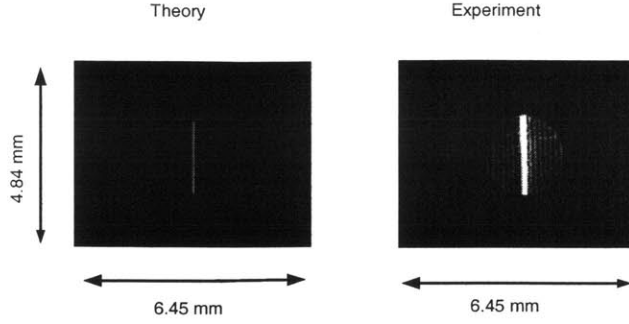


Figure 2-24: Theoretical and experimental diffracted patterns on CCD for PR VHI with a point source displaced $\delta = 8$ mm from Bragg match.

and the Fourier transforming lens had a focal length $F = 63.9$ mm. We see that the experimental and theoretically predicted diffracted patterns match well. Again, pixel saturation results in the experimental degeneracy line being slightly thicker.

Fig. 2-25 presents line scan (method 2) PR VHI images of the “MIT” artifact which is shown in Figure 4-2(a). For the imaging experiments, we employed 2D scanning using two orthogonal Newport CMA-25CCCL actuators and a CCD camera to acquire images of the object one slit at a time by exploiting the straight line y -degeneracy of PR VHI. The entire experimental setup for image acquisition was controlled via MATLAB. The experimental setup was identical to the one described with reference to Figure 2-24. Fig. 2-25(a) is a PR image of the object with the surface of the letter M located at the Bragg matched height. As a result, the letter M appears brightest. The letters I and T are 2 and 4 mm away from the Bragg matched location and thus appear progressively darker. Fig. 2-25(b) is the PR VH image with the surface of the letter I located at the Bragg matched height. Note that the letters M and T appear equally dark. Fig. 2-25(c) is the PR VH image with the surface of the letter T located at the Bragg matched height, note that the letters I and M now again appear progressively darker². To quantify the Bragg mismatch, we define $P_{i,j}$ to be the average intensity of the letter i when the letter j is at the Bragg matched location. The average values of the intensity are given in Table 2.1. The corresponding

²These experiments were conducted by me and Wenyang Sun and I would like to thank him for his assistance

ratios are given in Table 2.2, which are in good agreement with the estimates from the PSF calculation and experiments (Fig. 2-16).

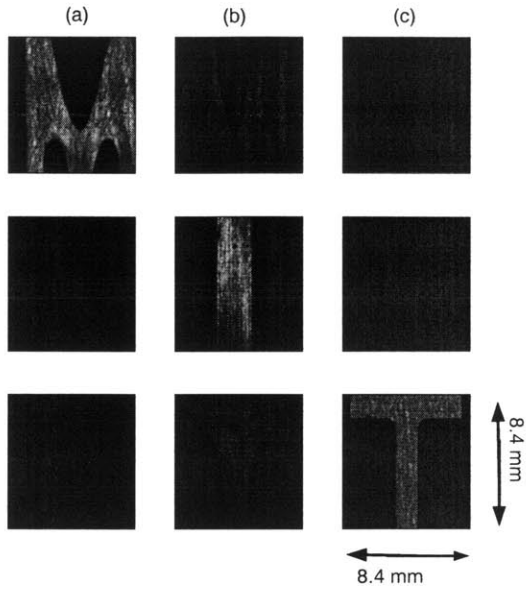


Figure 2-25: PR VH images of the fabricated letters MIT placed 50.2 mm away from the entrance pupil of the system. (a) is the actual CAD rendering of the object, (b) is a PR volume holographic image of the object obtained by a 1D scan with surface of the letter M being placed at Bragg matched location, (c) is an image of the object obtained by a 1D scan with surface of the letter I being placed at Bragg matched location and (d) is an image of the object obtained by a 1D scan with surface of the letter T being placed at Bragg matched location.

Finally, Fig. 2-26 presents PR VHI images of the same object with use of telephoto objective optics. The telephoto consisted of a thin positive lens of focal length $f_1 = 250$ mm separated from a thin negative lens of focal length $f_2 = -25$ mm by a distance $t = 500$ mm. The object was placed at a working distance $d = (\text{FFL}) = 500$ mm in front of the positive lens which had an aperture $a = 12.7$ mm. The actual size of the recorded hologram was $r = 2$ mm. From the PSF of Fig. 2-21, we see that the collector optics allow us to achieve a $\Delta z_{\text{FWHM}} \approx 1$ mm for an object located $D = 500$ mm away. Fig. 2-26 shows a progression of images referenced at the three characteristic heights of the artifact similar to Fig. 2-25. The average powers and power ratios are given in Tables 2.3 and 2.4 respectively. Again, good agreement

Measured Intensity	Measured Intensity	Measured Intensity
$P_{M,M} = 10.6 \pm 0.13$	$P_{M,I} = 2.51 \pm 0.25$	$P_{M,T} = 1.80 \pm 0.24$
$P_{I,M} = 2.05 \pm 0.28$	$P_{I,I} = 9.21 \pm 0.14$	$P_{I,T} = 2.05 \pm 0.31$
$P_{T,M} = 1.89 \pm 0.27$	$P_{T,I} = 2.18 \pm 0.29$	$P_{T,T} = 9.59 \pm 0.13$

Table 2.1: Measured intensity values for stand alone PR VHI (a.u.).

Measured Intensity	Measured Intensity	Measured Intensity
$\frac{P_{I,M}}{P_{M,M}} = 0.19 \pm 0.05$	$\frac{P_{M,I}}{P_{I,I}} = 0.27 \pm 0.04$	$\frac{P_{M,T}}{P_{T,T}} = 0.19 \pm 0.05$
$\frac{P_{T,M}}{P_{M,M}} = 0.17 \pm 0.03$	$\frac{P_{T,I}}{P_{I,I}} = 0.24 \pm 0.07$	$\frac{P_{I,T}}{P_{T,T}} = 0.21 \pm 0.04$

Table 2.2: Ratios of intensity values calculated from Table 2.1.

Measured Intensity	Measured Intensity	Measured Intensity
$P_{M,M} = 10.3 \pm 0.14$	$P_{M,I} = 2.06 \pm 0.28$	$P_{M,T} = 1.50 \pm 0.24$
$P_{I,M} = 1.96 \pm 0.35$	$P_{I,I} = 9.83 \pm 0.16$	$P_{I,T} = 1.89 \pm 0.35$
$P_{T,M} = 1.55 \pm 0.3$	$P_{T,I} = 2.00 \pm 0.33$	$P_{T,T} = 9.40 \pm 0.15$

Table 2.3: Measured intensity values for PR VHI with telephoto system (a.u.).

Measured Intensity	Measured Intensity	Measured Intensity
$\frac{P_{I,M}}{P_{M,M}} = 0.19 \pm 0.07$	$\frac{P_{M,I}}{P_{I,I}} = 0.21 \pm 0.04$	$\frac{P_{M,T}}{P_{T,T}} = 0.16 \pm 0.05$
$\frac{P_{T,M}}{P_{M,M}} = 0.15 \pm 0.04$	$\frac{P_{T,I}}{P_{I,I}} = 0.20 \pm 0.07$	$\frac{P_{I,T}}{P_{T,T}} = 0.20 \pm 0.05$

Table 2.4: Ratios of intensity values calculated from Table 2.3.

with the PSF data of Figure 2-21 is observed. The corresponding ratios, given in Table 2.4 are also in good agreement with the estimates from the PSF calculation and experiments (Fig. 2-21).

2.3 Exploiting a-priori object information to enhance depth resolution

We have seen that the optimal depth resolution for PR-VHI is given by (2.49). This is a worst case result applicable when we do not have any prior information about the object being imaged. In many cases, such as surface metrology and inspection applications, prior information is available and can be utilized to yield improved

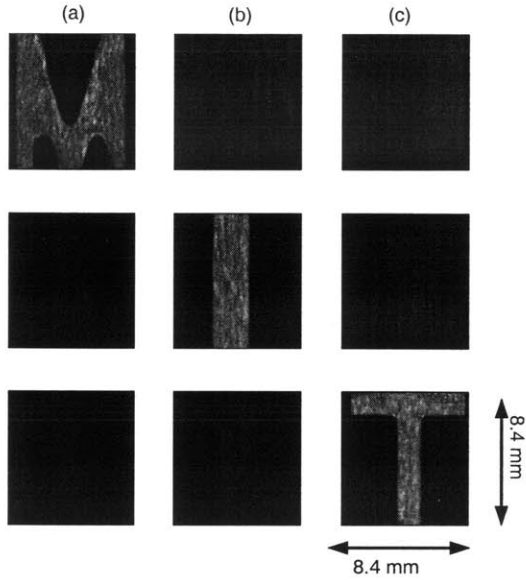


Figure 2-26: PR VH images using collector optics of the fabricated letters MIT placed 500 mm away from the entrance pupil of the system. (a) is a PR volume holographic image of the object obtained by a 1D scan with surface of the letter M being placed at Bragg matched location, (b) is an image of the object obtained by a 1D scan with surface of the letter I being placed at Bragg matched location and, (c) is an image of the object obtained by a 1D scan with surface of the letter T being placed at Bragg matched location.

resolution. For instance, most microchips and MEMS devices have only flat surface features of various heights since silicon manufacturing technology is predominantly planar.

Consider the case when the object is known to consist only of flat surfaces, as shown in Fig. 2-27. A PR-VHI system can obtain a surface profile of the object by a complete point/line scan as described in section 2.2.2. The direction along which scanning is done has a significant bearing on the system's longitudinal resolution [83].

In Fig. 2-27(a), the object (or equivalently the PR-VHI sensor) is scanned such that both the longitudinal scan direction and the angle of incidence of the active illumination is parallel to the optical axis of the sensor. In this case, the resolution of the system is indicated by the dashed ellipse. Notice that the quadratic dependence of depth resolution results in the depth resolution (Δz) being poorer than the lateral

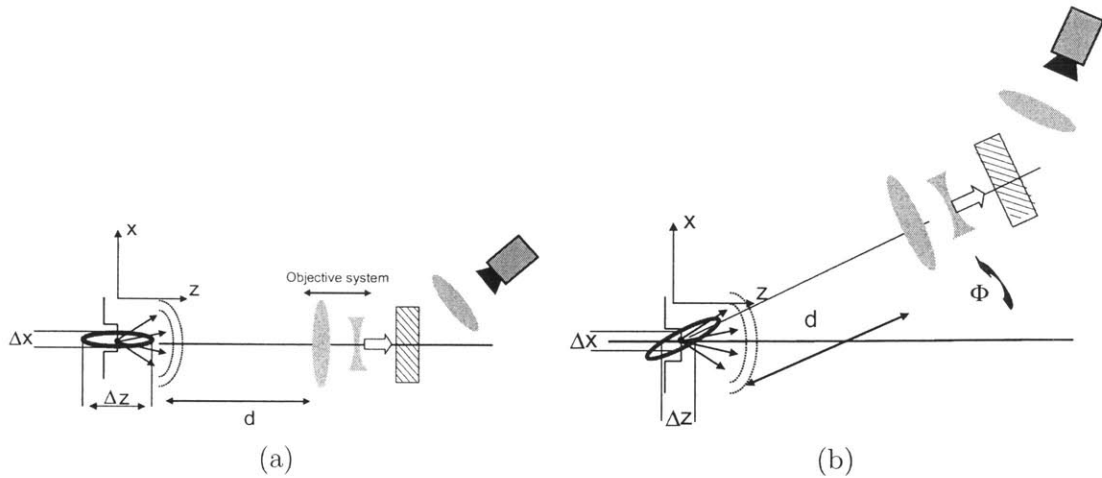


Figure 2-27: (a) PR-VHI metrology system at normal incidence (b) Inclined PR-VHI system to exploit a-priori object information.

resolution (Δx).

However, we can take advantage of the fact that the object consists only of flat surfaces by altering the scan direction. This is shown in Fig. 2-27(b). The object with flat surfaces is scanned in a direction inclined (or equivalently the PR-VHI sensor and/or the active illumination direction are inclined) at an angle ϕ with respect to the optical axis. The depth resolution of the PR-VHI system along the optic axis is still Δz , but since the surfaces of the object are inclined at an angle ϕ with the axis, the PR-VHI can resolve lateral features of size $\approx \Delta x \cos \phi$ and surface height features $\approx \Delta x \sin \phi$. In other words, the superior lateral resolution (the width of the Bragg slit) manifests itself as an “apparent” depth resolution of the object’s surface features. It is important to note that this benefit is possible only because we know the nature of the object surface and are using this knowledge. Note that an inclined (non-flat) surface would reflect the incident active illumination in a different direction and no light would enter the PR-VHI system.

Figure 2-28 compares the resolution between a PR-VHI system imaging a flat surface for the case of scanning the object along the optical axis and scanning the object at an angle $\phi = 30^\circ$ inclined with respect to the optical axis. Notice that the inclined sensor has much better resolution on account of the sinc squared envelope

imposed by the Bragg selectivity of the volume hologram.

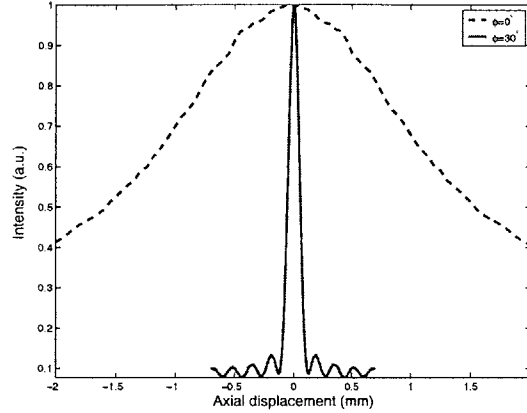


Figure 2-28: Depth resolution improves by taking advantage of a-priori object information. The PR-VHI sensor had $f = 460$ mm, $a = 5$ mm and $F = 50.2$ mm for the same LiNbO_3 crystal used in Fig.2-17.

2.4 PR-VHI using broadband illumination

We now derive the properties of a PR-VHI system when it is read out by illumination of wavelength that is different from the one used to write the volume hologram. In this case, the setup is still the same as described in section 2.2.1 *i.e.* the volume hologram is the 3D interference pattern of two mutually coherent planar beams; a normally incident reference beam and a signal beam that is inclined at an angle $\theta_s \ll 1$ rad with respect to the \hat{z} -axis. The recording wavelength is λ_f . All angles and wavelengths are measured inside the volume hologram that is assumed to have a refractive index n and is L units thick.

The reference beam $\mathbf{E}_f(\mathbf{r})$ can be written as

$$\mathbf{E}_f(\mathbf{r}) = \exp \left\{ i2\pi \frac{z}{\lambda_f} \right\}. \quad (2.57)$$

The signal beam $\mathbf{E}_s(\mathbf{r})$ can be expressed in the paraxial approximation as

$$\mathbf{E}_s(\mathbf{r}) = \exp \left\{ i2\pi \left(1 - \frac{\theta_s^2}{2} \right) \frac{z}{\lambda_f} + i2\pi\theta_s \frac{x}{\lambda_f} \right\}. \quad (2.58)$$

The volume hologram is the recorded 3D interference pattern of the reference and signal beams. It is stored as a weak modulation $\Delta\epsilon(\mathbf{r}) \propto |\mathbf{E}_f + \mathbf{E}_s|^2$ of the dielectric constant. The Bragg matched term of the modulation is given by

$$\Delta\epsilon(\mathbf{r}) = \exp \left\{ \frac{i2\pi}{\lambda_f} \left(x\theta_s - z\frac{\theta_s^2}{2} \right) \right\}. \quad (2.59)$$

For the purpose of this derivation, we will assume that the hologram has infinite lateral extent.

The readout procedure is also exactly the same as described in section 2.2.1. An objective lens of focal length f and aperture a is placed in front of the volume hologram to collimate the field arising from a probe point source located at $\mathbf{r}_p = (x_p, y_p, z_p)$ and is emitting at a wavelength λ_p . If a probe of wavelength $\lambda_p = \lambda_f$ is placed at the Bragg matched location $(0, 0, -f)$, then the objective lens can perfectly collimate the probe and a normally incident probe beam is incident on the volume hologram. The volume hologram would then diffract a continuation of the signal beam, *i.e.* a plane wave propagating in direction θ_s . A Fourier transform lens (of focal length F) that is placed behind the hologram focuses the diffracted plane wave onto the detector. However, if the probe is not exactly Bragg matched, then the objective lens can no longer ensure that the field input to the hologram is a normally incident plane wave. In this situation, only the Bragg matched components of the input field are diffracted by the hologram.

To examine the effect of Bragg mismatch, we still use the “transfer function” [95] approach. The 3D Fourier transform of the dielectric constant modulation $\Delta\epsilon$ evaluated at $\mathbf{k}_p - \mathbf{k}_d$, *i.e.*

$$\tilde{A}(\mathbf{k}_p, \mathbf{k}_d) = S \int_{\mathcal{V}} \Delta\epsilon(\mathbf{r}) \cdot \exp \{ i(\mathbf{k}_p - \mathbf{k}_d) \cdot \mathbf{r} \} d^3\mathbf{r} \quad (2.60)$$

specifies the spatial response of the hologram to a single spatial frequency in the input field. Hence, it can be thought of as the spatial frequency response, or transfer function, of the volume hologram. In (2.60), S is a constant determined by the polarization and index modulation; our analysis will normalize the diffracted intensities, so this factor can be ignored. Under the paraxial approximation, the probe wave vector is

$$\mathbf{k}_p = 2\pi \left(f_x \hat{\mathbf{x}} + f_y \hat{\mathbf{y}} + \frac{1}{\lambda_p} \left(1 - \frac{\lambda_p^2 (f_x^2 + f_y^2)}{2} \right) \hat{\mathbf{z}} \right) \quad (2.61)$$

In (2.61), $f_x = \cos \theta_x / \lambda_p$ and $f_y = \cos \theta_y / \lambda_p$ are the spatial frequency components of the input probe field. θ_x and θ_y represent the angle that the plane wave component makes with the $\hat{\mathbf{x}}$ and $\hat{\mathbf{y}}$ axes respectively.

Similarly, because of the Fourier lens, we can express the diffracted wave vector in the paraxial approximation as

$$\mathbf{k}_d = 2\pi \left(\frac{x'}{\lambda_p F} \hat{\mathbf{x}} + \frac{y'}{\lambda_p F} \hat{\mathbf{y}} + \frac{1}{\lambda_p} \left(1 - \frac{(x'^2 + y'^2)}{2F^2} \right) \hat{\mathbf{z}} \right). \quad (2.62)$$

In (2.62), the spatial frequency components $x'/\lambda_p F$ and $y'/\lambda_p F$ are defined based on the detector coordinates (x', y') . For the planar reference hologram of infinite lateral extent and thickness L described in (2.31), $\tilde{A}(x'/\lambda_p F, y'/\lambda_p F; f_x, f_y)$ is given by [90]

$$\tilde{A} \left(\frac{x'}{\lambda_p F}, \frac{y'}{\lambda_p F}; f_x, f_y \right) = \delta \left(f_x - \frac{x'}{\lambda_p F} + \frac{\theta_s}{\lambda_f} \right) \delta \left(f_y - \frac{y'}{\lambda_p F} \right) \text{sinc} \left(L \left(\frac{(x'^2 + y'^2)}{2\lambda_p F^2} - \frac{\lambda_p (f_x^2 + f_y^2)}{2} - \frac{\theta_s^2}{2\lambda_f} \right) \right) \quad (2.63)$$

Eqn. (2.63) can be used to calculate the spatial spectrum of the diffracted field $\tilde{\mathbf{E}}_d$ if the spatial spectrum of the input field $\tilde{\mathbf{E}}_p$ is known according to

$$\tilde{\mathbf{E}}_d \left(\frac{x'}{\lambda_p F}, \frac{y'}{\lambda_p F} \right) = \iint \tilde{\mathbf{E}}_p(f_x, f_y) \tilde{A} \left(\frac{x'}{\lambda_p F}, \frac{y'}{\lambda_p F}; f_x, f_y \right) df_x df_y. \quad (2.64)$$

We first examine the response of a probe source emitting at a wavelength λ_p located at the front focal plane of the objective lens. It will be convenient in the later

part of the analysis to define a normalized wavelength parameter

$$\mu = \frac{\lambda_p}{\lambda_f}. \quad (2.65)$$

It is possible to Bragg match this probe source [89] on account of the wavelength selectivity property of volume holographic gratings. To Bragg match the hologram, a probe beam must be displaced in the \hat{x} direction by an amount x that depends on μ as can be seen from (2.63) and (2.64). This probe is then called Bragg-degenerate. The required displacement is

$$\frac{x}{f} = \frac{\theta_s(1 - \mu)}{2}. \quad (2.66)$$

Based on (2.63) and (2.66), a Bragg-degenerate probe is mapped on to a specific location x' on the detector that satisfies the relation

$$\frac{x'}{F} = \frac{\theta_s(1 + \mu)}{2}. \quad (2.67)$$

The planar reference hologram is also degenerate in the \hat{y} direction [90]. As a result, the volume hologram can image a slit in the Bragg plane. From (2.67), we see that the volume hologram can also simultaneously map different spectral frequencies onto different locations on the detector plane. As a result, the planar reference volume hologram can be used to design a real-time spectrum analyzer based on the dispersive properties of the volume holographic grating. This is discussed further in section 4.3.

We now examine a probe source that is axially displaced by δ from the Bragg matched location (2.66). Therefore, the objective lens can no longer collimate the probe field. Instead, the field incident on the hologram is a spherical wave originating at the virtual object position

$$z_p = \frac{f(f - \delta)}{\delta} \approx \frac{f^2}{\delta} \quad (2.68)$$

for $\delta \ll f$. Only the on-axis Fourier component of this spherical probe is Bragg matched; therefore, the overall intensity diffracted from the hologram is reduced.

The analysis of the diffracted field is done in manner similar to [90] by using Weyl's identity to define the spatial spectrum of a spherical wave and using equations (2.63) and (2.64). The observed diffracted intensity on the detector is

$$\frac{I(x', y', \mu)}{I_b} \approx \text{circ} \left(\frac{|\mathbf{r}'|}{Fa\delta/f^2} \right) \text{sinc}^2 \left(\frac{L\theta_s}{\lambda_p} \left(\frac{x'}{F} - \frac{\theta_s(1+\mu)}{2} \right) \right), \quad (2.69)$$

where $I_b = I(x' = \theta_s F, y' = 0, \delta)$ is the peak intensity produced by the probe and

$$|\mathbf{r}'|^2 = \left[x' - F \left(\frac{\theta_s(1+\mu)}{2} - \frac{\delta\theta_s(1-\mu)}{2f} \right) \right]^2 + (y')^2 \quad (2.70)$$

represents the geometrical image of the aperture of the objective lens (equivalently, the defocused image of the probe) outside which the diffracted power is approximately zero. It is interesting to note that when $\lambda_p = \lambda_f$, *i.e.* $\mu = 1$, the Bragg slit remains centered inside the geometrical image of the aperture for all δ . However, if $\mu \neq 1$, the center of the defocused spot changes with δ according to (2.70), and the Bragg slit appears to move relative to the disk. This phenomenon has a significant effect on the depth resolution of a broadband PR-VHI system, which we discuss in section 2.5.

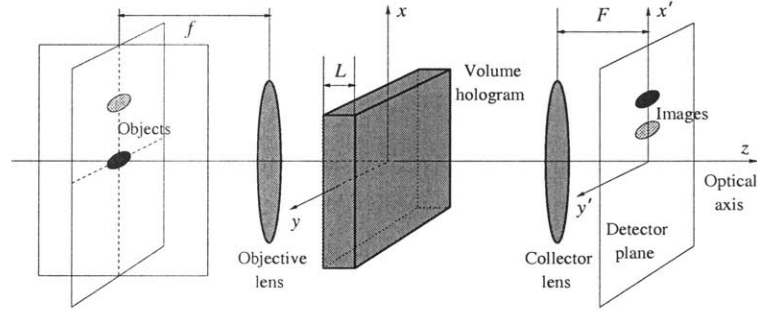


Figure 2-29: Setup for experimental verification of diffracted field for two color readout

We now present experimental verification of the theoretical analysis discussed above. Fig. 2-29 shows a schematic of the experimental setup used. The objective lens had focal length $f = 50.2$ mm and aperture $a = 4$ mm, the fourier transforming lens had $F = 75$ mm, the volume hologram was recorded in a 2 mm thick crystal of

LiNbO₃ using a doubled Nd:YAG laser ($\lambda_f = 532\text{nm}$) with a normal reference beam and signal beam inclined at $\theta_s = 0.2$ rad; the diffraction efficiency of the hologram was $\approx 5\%$ and the camera used a JAI CV 235 industrial CCD with pixel size = $9\mu\text{m}$. The PR-VHI system was read out in turn by two probe sources. The first probe was emitting at $\lambda_p = 532$ nm; it was created by focussing the light from the Nd:YAG laser and was Bragg matched on-axis. The second probe was emitting at $\lambda_p = 632.8$ nm; it was created by focussing the light from a 20 mW He-Ne laser and the Bragg matched location was displaced off-axis as specified by (2.66). When the PR-VHI system was read out with $\delta = 0$, both probe sources gave rise to focused images on the CCD. The location of the images was specified by (2.67) with $\mu_1 = 1$ for the green probe and $\mu_2 = 1.19$ for the red probe. This is shown in Fig. 2-30(a). The focused images are separated by 1.42 mm, consistent with (2.67). When the probes were defocused by $\delta = 4$ mm, the diffraction patterns on the CCD were specified by (2.69). This is seen in Fig. 2-30(b). The diffraction pattern arising from the on-axis green probe remains symmetric with the Bragg slit centered within the defocus disk. However, the Bragg slit for the off-axis red probe is no longer centered within the disk and shifts by $117\mu\text{m}$ as predicted in (2.70).

2.5 Depth resolution of PR-VHI under broadband illumination

We still define the depth resolution for a broadband PR-VHI system as the FWHM of the longitudinal PSF measured by an integrating detector placed behind the volume hologram. For a monochromatic PR-VHI system, the normalized PSF has been calculated as (2.41),

$$\frac{I_d}{I_o} = \frac{1}{\pi} \int_0^{2\pi} d\phi \int_0^1 d\rho \rho \operatorname{sinc}^2 \left(\frac{aL \sin \theta_s \delta}{\lambda f^2} \rho \sin \phi \right), \quad (2.71)$$

where I_o represents the peak Bragg matched power at $\delta = 0$. The depth resolution Δz_{FWHM} for a monochromatic (wavelength = λ_p) point source located at the Bragg

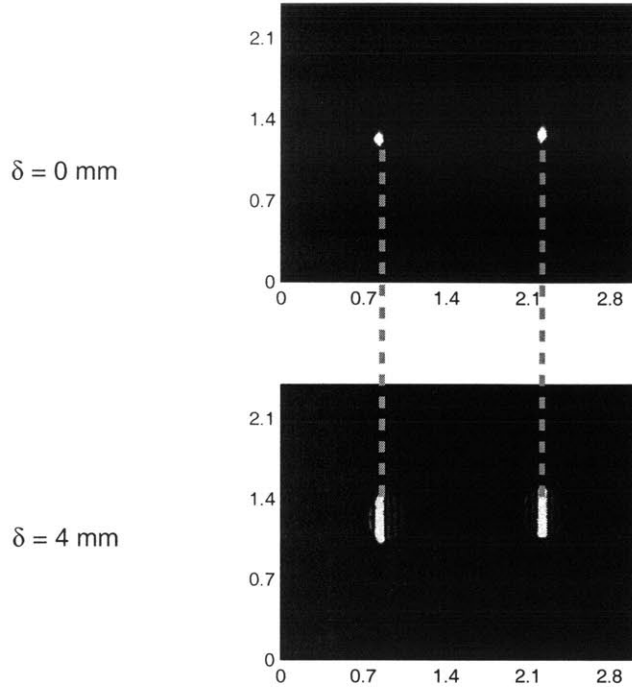


Figure 2-30: Experimentally observed diffracted field for readout using two mutually incoherent Bragg matched point sources emitting at $\lambda_p = 532$ nm and $\lambda_p = 632.8$ nm. (a) Defocus $\delta = 0$ (b) $\delta = 4$ mm. All lateral dimensions are in mm.

matched position specified in (2.66) is [90]

$$\Delta z_{\text{FWHM}} = \frac{5.34 f^2 \lambda_p}{a \theta_s L}. \quad (2.72)$$

All the variables in (2.72) have been defined in section 2.4. In addition to the wavelength dependence of Δz_{FWHM} specified in (2.72), the depth resolution for the monochromatic source with $\mu \neq 1$ is also effected by the fact that the Bragg slit does not remain centered inside the defocus disk as δ changes (2.70). This results in the wavelength-normalized PSF for $\mu \neq 1$ being slightly narrower than the $\mu = 1$ PSF. This effect is extremely small as shown in the theoretical curve of Fig. 2-31(a). The narrowing effect was not observable in our experiments with the red and green probes (see Fig. 2-31(b)) described in section 2.4.

Now consider a broadband probe source of spectral profile $S'(\lambda_p)$. We can trans-

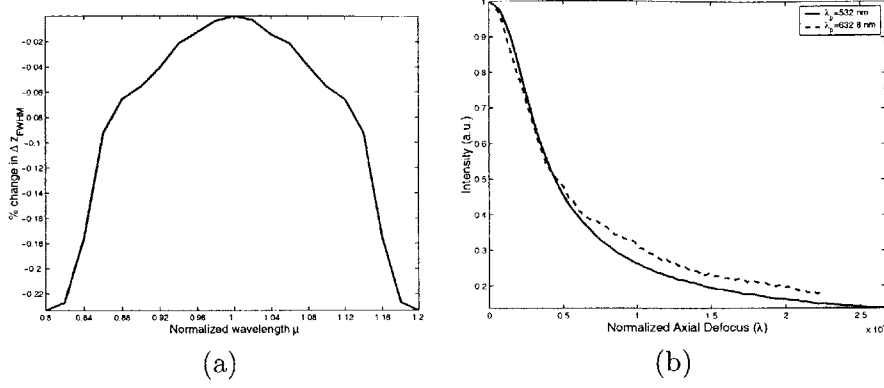


Figure 2-31: (a)Percentage change in wavelength–normalized Δz_{FWHM} as a function of normalized wavelength μ . We note that the PSF narrowing effect is very small and can be neglected for most practical purposes as seen in (b) Experimentally observed longitudinal PSFs for the two point sources described in Fig.2-30.

form $S'(\lambda_p)$ and express it in terms of the parameter μ defined in (2.65) to obtain the new spectral profile $S(\mu)$. Let us assume that the spectral profile is centered at μ_c and has bandwidth $2\Delta\mu$. Since the probe source is emitting over a broad range of wavelengths, it can simultaneously illuminate several Bragg slits (each corresponding to a particular wavelength) of the PR-VHI system. From (2.66), we see that the broadband probe source can be placed over a range of off-axis locations

$$x_c \pm \Delta x = \frac{f\theta_s(1 - \mu_c)}{2} \pm \frac{f\theta_s\Delta\mu}{2}, \quad (2.73)$$

and still Bragg match the hologram. In other words, the field of view (FOV) of the probe source increases with illumination bandwidth. A monochromatic point source $\mu = \text{constant}$ can be Bragg matched and is visible only at one location on the object focal plane. However, a broadband source $\mu_c \pm \Delta\mu$ can be Bragg matched and is visible over the range specified by (2.73). The observed diffracted pattern $I_{BB}(x', y')$ for a broadband probe source can be calculated as a superposition of the diffraction patterns arising from each spectral component of the broadband source, that is

$$I_{BB}(x', y') = \int I(x', y', \mu)S(\mu)d\mu. \quad (2.74)$$

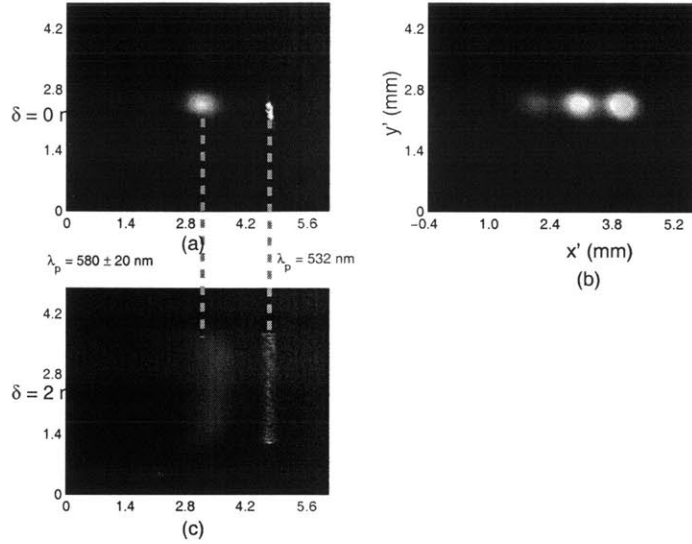


Figure 2-32: Experimentally observed diffraction pattern observed for broadband fluorescent object emitting at $\lambda_p = 580 \pm 20 \text{ nm}$. (a) Comparing Bragg matched laser $\lambda_p = 532 \text{ nm}$ and fluorescent source. (b) Fluorescent source stays visible for a large lateral translation $\Delta x' = 3 \text{ mm}$. (c) Bragg slit at $\delta = 2 \text{ mm}$ for the fluorescent source is wider than the laser Bragg slit.

The diffraction pattern for a fluorescent broadband source is shown in Fig. 2-32. The probe was emitting at a bandwidth $580 \pm 20 \text{ nm}$. the setup was similar to the schematic shown in Fig. 2-33(a). The volume hologram was a $200\mu\text{m}$ thick photopolymer manufactured by Aprilis Inc. It was pre-recorded using $\lambda_f = 488 \text{ nm}$ and provided by Ondax, Inc. The diffraction efficiency was $\eta \approx 60\%$. Both the objective and Fourier lenses had focal length 50.2 mm . Fig. 2-32(a) shows the observed intensity for $\delta = 0$ when the hologram is read out using a monochromatic laser source $\lambda_p = 532 \text{ nm}$ and the broadband source with $\mu \approx 1.19 \pm 0.04$. Note that both generate in-focus images. Fig. 2-32(b) shows the persistence of the diffracted intensity on the detector as the broadband probe is translated in the lateral direction. Fig. 2-32(c) shows the diffraction pattern for defocus $\delta = 2 \text{ mm}$ for both the monochromatic and broadband probes. The monochromatic probe gives rise to a single Bragg slit specified by (2.69). On the other hand, the broadband source gives rise to a wider Bragg slit on account of the superposition of several spectral terms according to (2.74).

It is intuitive to expect that there is a price to be paid for the improved FOV

offered by broadband illumination. This tradeoff manifests itself in a degradation of the depth contrast of the broadband PR-VHI system when compared with the corresponding monochromatic case.³ Consider the schematic of Fig. 2-33(a). We assume that the on-axis probe simultaneously emits two different wavelengths: a Bragg matched component $\mu_1 = 1$ and a Bragg mismatched term μ_2 . The PSF of the μ_1 component follows exactly the same pattern as (2.41). This PSF is shown by the solid curve in Fig. 2-33(b). The maximum diffracted power is observed at $\delta = 0$.

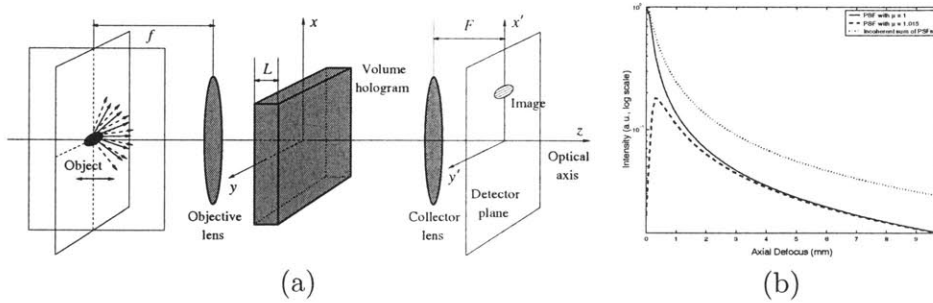


Figure 2-33: Depth resolution under broadband illumination. (a) Simulation setup used, the object is assumed to emit at two discrete wavelengths $\lambda_{p,1} = 532\text{nm}$ and $\lambda_{p,2} = 540\text{nm}$, $a = 12.7\text{ mm}$, $f = 50.2\text{ mm}$, $L = 2\text{ mm}$ and $\theta_s = 30^\circ$ (b) Theoretical PSFs: Solid line $\mu = 1$; dashed line $\mu = 1.015$; the dotted line is the incoherent sum of the two PSFs and is broader than the monochromatic PSF.

The μ_2 component behaves differently. At $\delta = 0$, this component is Bragg mismatched and hence the diffracted power is very low. The defocus disk is centered at $(\theta_s F, 0)$ on the detector plane. Its radius $|r'|$ depends on δ as

$$|r'| = \frac{F a \delta}{f^2} \quad (2.75)$$

The Bragg matched slit corresponding to μ_2 is located at

$$x' = \frac{F \theta_s (\mu_2 + 1)}{2}. \quad (2.76)$$

³Our colleague Chris Moser has pointed out that reflection geometry VHI might possibly be better suited for high depth resolution broadband applications because of its high wavelength selectivity

Thus, when

$$|r'| \geq \frac{F\theta_s(\mu_2 - 1)}{2}, \quad (2.77)$$

the diffracted power on account of the μ_2 component starts increasing since a larger portion of the defocus disk is Bragg matched. As a result, the PSF associated with μ_2 peaks at $\delta = 0.5$ mm as shown by the dashed curve in Fig. 2-33.

The net diffracted power is the incoherent sum of both the spectral components and is the dotted curve in Fig. 2-33. It is seen that the broadband PSF is wider than the corresponding monochromatic PSF. The expression for the polychromatic axial PSF is

$$I(\delta) = \iint I_{BB}(x', y') dx' dy', \quad (2.78)$$

where $I_{BB}(x', y')$ can be calculated using (2.74). Thus, we see that a tradeoff exists between the FOV and depth contrast of PR-VHI system. Figure 2-34 compares the depth resolution of the monochromatic and broadband sources described in Fig. 2-32. As expected, the wider Bragg window for the fluorescent probe results in poorer rejection of out-of-focus light and results in a much broader longitudinal PSF for the fluorescent probe.

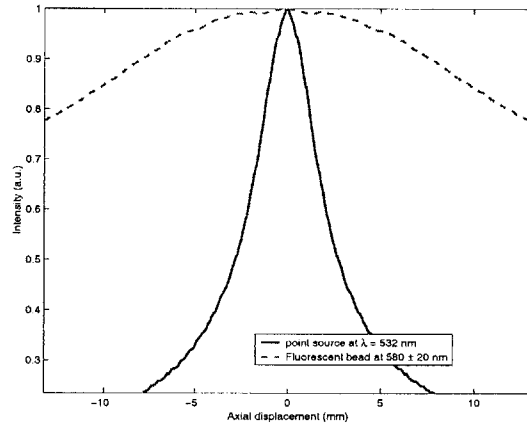


Figure 2-34: Comparing depth resolution for monochromatic and broadband illumination. The broadband PSF (dashed line) is broader than the monochromatic PSF (solid line).

The experimental results of Fig. 2-35 depict surface profilometry using broadband

VHI. Figure 2-35(a) shows a digital picture of the the object, the bottom chassis of a toy car. When narrow band light is used to image the object, the FOV is limited as shown in Fig. 2-35(b); however, the contrast between surfaces at different heights, which is a measure of the depth resolution, is very high as shown in Fig. 2-35(d). On the other hand, Fig. 2-35(c) shows the same object being imaged using broadband illumination. The FOV of the system now incorporates the entire object of interest and it is possible to take a one shot image of the object. However, the depth resolution *i.e.* the contrast in between the surfaces at different heights has deteriorated as a consequence of increasing the FOV. We estimated that the depth resolution degraded by a factor of 2.8 (see Fig. 2-35(e))as the illumination bandwidth was increased.

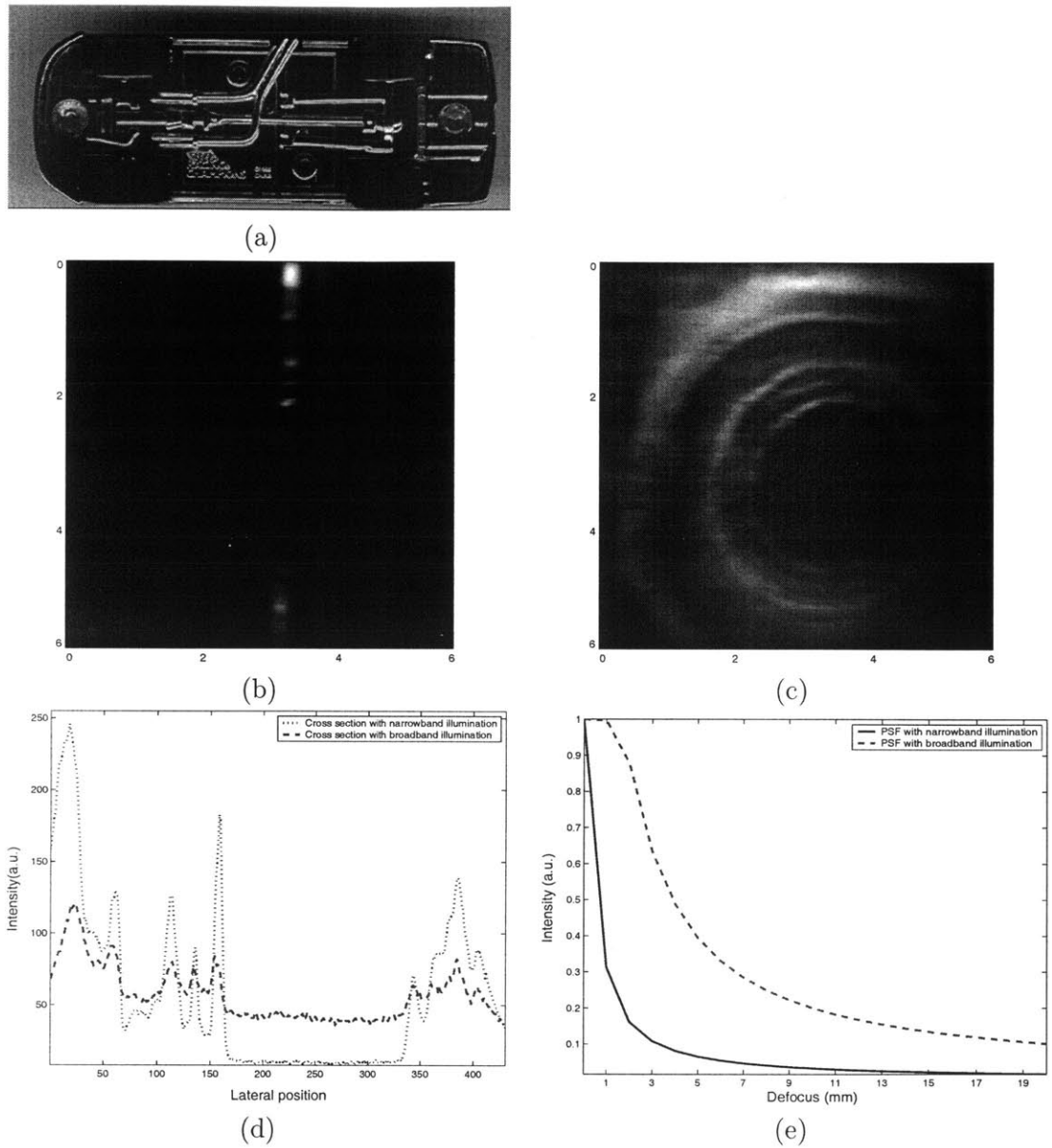


Figure 2-35: Tradeoff involved in between field of view and depth resolution for broadband VHI. (a) Object of interest is the bottom screw in the chassis of the toy car. (b) & (c) The FOV for narrowband (green light with $\Delta\lambda \approx 10$ nm) illumination is much lesser than that of broadband illumination (white light with $\Delta\lambda \approx 120$ nm). All lateral dimensions are in mm. (d) Depth resolution, or equivalently the contrast in between surface features at different heights is much better for the narrowband illumination as also shown in (e) the theoretical PSF curves under narrowband and broadband illumination.

Chapter 3

N-ocular Volume Holographic Imaging

We have shown previously in Chapter 2 that a volume holographic imaging system utilizes Bragg selectivity to optically “slice” the object space and measure up to four-dimensional object information with high resolution. In this chapter, we discuss an imaging system with multiple volume holographic sensors that can significantly improve the resolution for broadband objects located at long working distances. We refer to this setup as *N*-ocular volume holographic imaging.

3.1 Resolution of PR-VHI systems

In this section, we go over the trends observed in the depth resolution for PR-VHI systems. For resolution studies, we focus on two cases:

1. Imaging is done under conditions of monochromatic illumination with the imaging/readout wavelength $\lambda_p = \lambda_r$.
2. The illumination used for imaging is broadband with a spectral profile $S'(\lambda_p)$ defined over a wavelength range $\lambda_c \pm \Delta\lambda$.

For an on-axis point source, we have estimated the FWHM of the longitudinal PSF in section 2.2.2 to be

$$\Delta z_{\text{FWHM}} = \frac{5.34\lambda_f d^2}{\theta_s a L}. \quad (3.1)$$

In (3.1), $d = f$ is the working distance of the PR-VHI system. Further, the lateral resolution of the system corresponds to the width of the Bragg slit which is given by

$$\Delta x_{\text{B}} = \frac{2\lambda_f d}{\theta_s L}. \quad (3.2)$$

From (3.1), we see that the depth resolution of the PR-VHI system degrades quadratically with increasing object distance [82]. In section 2.2.2, we showed that the resolution can be optimized by appropriately designed objective optics for a particular working distance. However beyond this, one is still subject to the quadratic degradation of resolution. A similar quadratic degradation is observed in most systems that resolve longitudinal features [1]. In addition to this quadratic degradation, we have also seen in section 2.5 that depth resolution also degrades with increased illumination bandwidth. This results in very poor longitudinal resolution when imaging distant objects with broadband VHI.

The lateral resolution, however, depends only linearly on the working distance as shown in (3.2). Consequently, at long working distances, we can improve the depth resolving ability of the PR-VHI system by exploiting the superior lateral resolution. This can be done by using a priori object information [83] or by using multiple PR-VHI systems to simultaneously image a single object in a manner similar to binocular systems that perform triangulation [44]. We discuss this in section 3.2.

3.2 Overcoming depth resolution degradation using multiple PR-VHI sensors and digital post-processing

In the previous section, we have seen that for a PR-VHI system, a combination of long working distance and large illumination bandwidth results in a loss of depth resolution. In this section, we discuss one way to solve this problem by using multiple PR-VHI sensors that are pre-configured to look at the object of interest from different perspectives. The images from each PR-VHI sensor are then combined digitally to obtain a high resolution 3D image of the object. This solution is inspired by stereo vision [44], found in many animals as well as artificial machine vision systems.

However, there are several important differences between triangulation and the multiple PR-VHI sensor setup. Triangulating systems need to establish correspondence [96] between the location of a particular object feature on the multiple acquired images (Many active triangulation schemes [97, 98] do not need correspondence, but they require structured illumination). The Bragg selectivity and wavelength degeneracy properties of volume holograms [65, 89] ensure that there is no need to establish correspondence if the location of the PR-VHI system is known precisely. Moreover, since multiple ($N \geq 2$) sensors might be configured to be looking at the same object, it is possible to achieve N -ocular imaging. Below, we describe the working principle involved in improving the depth resolution. If two sensors, with their respective optical axes forming an angle ϕ , are observing the same object, their PSFs are also inclined relatively by the same angle. Provided that the sensors are oriented such that their optical axes intersect, the location of the source of the diffracted light is actually constrained to lie at the intersection of the volumes of the two PSFs (assuming that the optical axis orientations are known). This means that the 3D location of the light source is triangulated without the need for establishing correspondence. A simple ad-hoc way to characterize the constrained system is to define its PSF as the product of the individual PSFs. Hence, the resolution of combined system is better

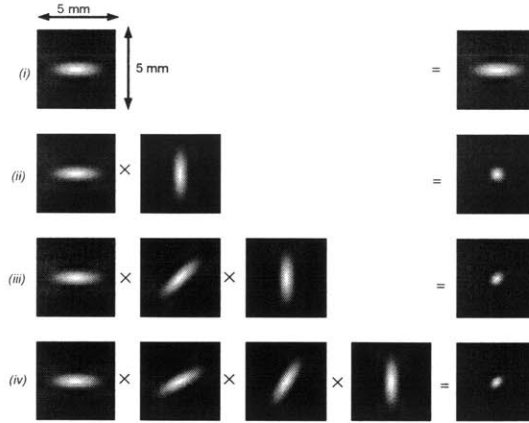


Figure 3-1: Theoretical performance of imaging with multiple sensors. (i) PSF of single sensor. (ii) PSF of two sensors at $\phi = 90^\circ$. (iii) PSF of three sensors at 45° . (iv) PSF of four sensors at 30° .

than the resolution of each individual sensor. The use of a product in the definition is justified if we interpret the PSF as an “ambiguity volume.” The point object may be located anywhere within the ambiguity volume, with probability proportional to the local value of the PSF.

Fig. 3-1 illustrates the successive improvements in resolution obtained as one moves from a single sensor system to a system with multiple sensors. The most significant improvement in resolution is obtained when comparing a single sensor to two sensors that are mutually perpendicular to each other (*i.e.*, at $\phi = 90^\circ$). Beyond this, adding sensors improves the resolution only marginally. However, multiple sensors can allow signal detection even when the depth resolution is very poor and can allow for better over-constraining of an object location. In Fig. 3-2, we plot the theoretical depth resolution against the distance of the object for 4 different cases. The plots represent the expected depth resolution for N-ocular imaging assuming ϕ is the viewing angle available to look at the object. The Δz_{FWHM} is calculated by point multiplication of individual sensor measurements. We note that for large working distances, the depth resolution scales linearly with distance anytime $N > 2$ sensors are used.

Fig. 3-3 is an experimental demonstration of improvement in PR-VHI resolution

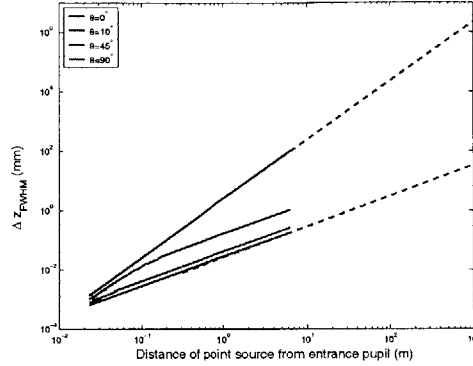


Figure 3-2: Theoretical depth resolution (FWHM) for different imaging geometries. ϕ refers to the viewing angle available to the VHI sensors (except when $\phi=0$, which refers to a monocular system). The number of sensors is taken to be 4 and we plot the expected value of the depth resolution for an arrangement of sensors from a uniform probability distribution.

by use of two sensors at angle $\phi = 10^\circ$ (limited because of lack of room on our optical table). Despite the relatively small angle, the resolution of the binocular system is still considerably better than the corresponding resolution for individual sensors. Optimum $\phi = 90^\circ$ as was pointed out earlier.

We will discuss two N -ocular VHI configurations, namely, improving depth resolution for surface profilometry in section 3.2.2 and improving depth resolution for imaging 3D objects in section 3.2.2.

3.2.1 N -ocular VHI for surface profilometry

We have seen that point multiplying intensity measurements taken from different perspectives allows us to locate a point source more accurately than a single measurement. However, point multiplication of the PSF for an extended object (many point sources) would require a very high sampling rate to recover the object surface from the data. Additionally, point multiplying PSFs tends to perform poorly with noisy data. To solve this problem, we have devised a method to apply the theory of inverse problems to the N -ocular VHI system which we describe below.

Let $I(\mathbf{r})$ denote the intensity distribution of the object as function of the spatial

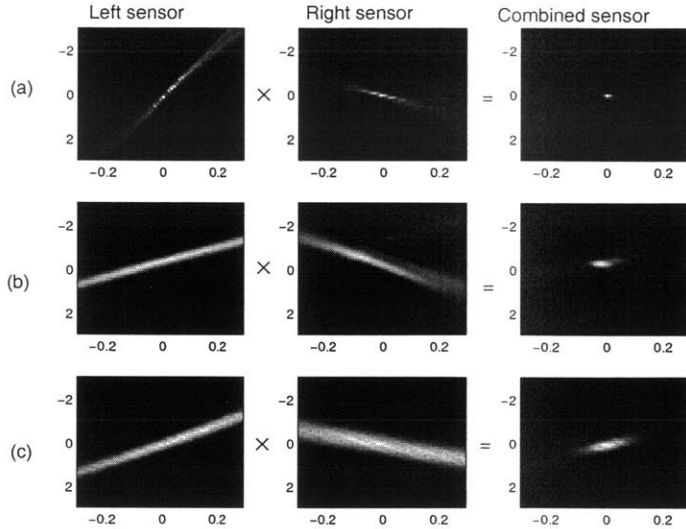


Figure 3-3: Experimental PSFs for two individual sensors oriented at $\phi = 10^\circ$ for point sources located at different distances in front of the sensor. (a) 29 cm; (b) 45 cm; (c) 72 cm.

coordinate \mathbf{r} in object space ($\mathbf{r} \in \mathcal{V}_s$.) After passing through an arbitrary linear optical system, the light intensity is transformed according to Hopkins' integral [1]

$$\tilde{I}(\mathbf{r}') = \int_{\mathcal{V}_s} h(\mathbf{r}, \mathbf{r}') I(\mathbf{r}) d^3 \mathbf{r}, \quad (3.3)$$

where $h(\mathbf{r}, \mathbf{r}')$ is the incoherent impulse response of the system. The output intensity $\tilde{I}(\mathbf{r}')$ is observed in an appropriate detector space, typically restricted to lie on a plane. Equation (3.3) is a Fredholm integral equation of the first kind, which is commonly encountered in inverse problems. It is generally known that these problems are ill-posed because the kernel $h(\mathbf{r}, \mathbf{r}')$ de-localizes the spatial contents of the source at the detector space. Moreover, in the case of volumetric imaging there is a dimensional mismatch between the object and detector spaces (3D and 2D, respectively.) The obvious way around the mismatch is to discretize the problem and make sure that there are at least as many intensity measurements available as desired samples from the object intensity distribution. Additionally, we also recognize that all the obtained object information consists of discrete data points. Thus, we assume that the source

is also discrete.

To treat the discrete model, we form a vector $\underline{\mathbf{I}}$ of object intensities, and a vector $\tilde{\underline{\mathbf{I}}}$ of intensity measurements. The intensity measurement vector should contain *all* the measurements pertinent to the imaging task at hand. For example, in the case of VHI, $\underline{\mathbf{I}}$ is formed by all the point-wise measurements. The superposition integral (3.3) then becomes a simple matrix equation

$$\tilde{\underline{\mathbf{I}}} = \underline{\mathbf{H}} \underline{\mathbf{I}}. \quad (3.4)$$

In this description, element $\underline{\mathbf{H}}_{jk}$ of system matrix $\underline{\mathbf{H}}$ quantifies the contribution of the k -th source $\underline{\mathbf{I}}_k$ to the j -th measurement $\tilde{\underline{\mathbf{I}}}_j$. In the absence of noise, we could invert the measurements to obtain the signal as

$$\underline{\mathbf{I}} = \underline{\mathbf{H}}^{-1} \tilde{\underline{\mathbf{I}}}. \quad (3.5)$$

However, noise in the measurements makes the inversion of equation (3.5) unstable. To quantify the effect of noise on our measurements, we write the imaging equation as

$$\tilde{\underline{\mathbf{I}}}_m = \underline{\mathbf{H}}_m \underline{\mathbf{I}}_m + \text{noise}. \quad (3.6)$$

In equation (3.6), the subscript m refers to the m^{th} data set obtained from sensor $\#m$. For an N -ocular system, N such measurements are available to us. In addition, we also know that since all the measurements correspond to the same signal (in this case the depth of the object); therefore the solution to the inverse problem for each of these measurements should yield the same solution. In other words, we can concatenate the data from each individual sensor and express the result as a single large vector $\underline{\mathbf{M}} = [\tilde{\underline{\mathbf{I}}}_1 \dots \tilde{\underline{\mathbf{I}}}_N]^T$ and $\underline{\mathbf{H}} = [\underline{\mathbf{H}}_1 \dots \underline{\mathbf{H}}_N]^T$. Writing the concatenated equation, we see that

$$\underline{\mathbf{M}} = \underline{\mathbf{H}} \underline{\mathbf{I}} + \text{noise}. \quad (3.7)$$

We can now solve for $\underline{\mathbf{I}}$ as

$$\underline{\mathbf{I}} = \underline{\mathbf{H}}^p \underline{\mathbf{M}}. \quad (3.8)$$

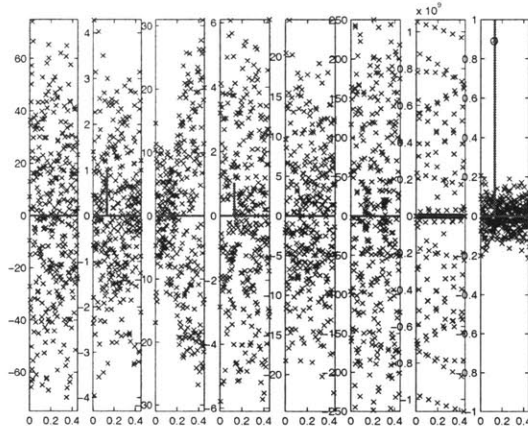


Figure 3-4: Theoretical performance of 7-ocular 1D sensor after post processing using a pseudo inverse. The SNR of each measurement is 10. The sensors are oriented in steps of 15° starting at 0° . The red curve indicates the original signal. It is seen that the pseudo inverse solution (extreme right) returns the correct location of the source whereas individual inversions do not.

In equation.(3.8), $\underline{\mathbf{H}}^p = (\underline{\mathbf{H}}^T \underline{\mathbf{H}})^{-1} \underline{\mathbf{H}}^T$ is the pseudo inverse of $\underline{\mathbf{H}}$. The pseudo inverse is a process that achieves a least squares error minimization to obtain the optimal solution to the over-constrained system (3.7). Fig. 3-4 shows the behavior of the inversion process for a 1D signal in the presence of extreme noise. We see that the inversion does not yield meaningful results for individual sensors. However, concatenating the measurements and performing a pseudo inverse on this vector yields the exact location of the signal. Thus, we see that post-processing allows us to recover object data beyond the nominal resolution limit (Δz_{FWHM}) of the system. Thus, N-ocular VHI yield superior resolution and SNR compared to a single sensor.

3.2.2 N-ocular VHI for 3D Imaging

For a single source, it is sufficient to point-multiply individual measurements to obtain accurate position information about the point object. A generic 3D object consists of several such sources distributed over a volume. Our goal is to efficiently recover a 3D image of the form $I(x, y, z)$, *i.e.* a complete three dimensional intensity distribution from the multiple VHI images. For such a 3D object, the point multiplication method would require extensive scanning to obtain the 3D image. This is time consuming

and we seek an alternate method that can efficiently recover the image with fewer measurements.

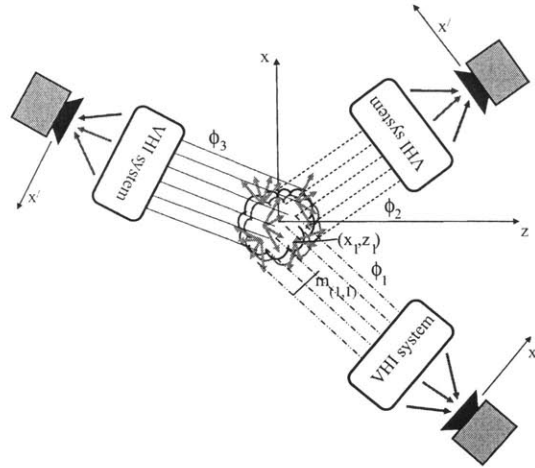


Figure 3-5: Schematic of N -ocular VHI system. For illustration purposes, we have depicted $N = 3$.

Figure 3-5 shows the schematic of an N -ocular PR-VHI system. For the purpose of this paper, we assume that the sensor can image the entire 3D object of interest without any defocus blur. For a simple camera, this assumption is equivalent to using an objective optical system whose depth of field [17] is larger than the longitudinal extent of the 3D object.

The Bragg slit of the PR-VHI system automatically eliminates the defocus blur in the \hat{x} direction and leaves only the degenerate out-of-plane \hat{y} direction susceptible to defocus effects. Thus for VHI, the no defocus assumption is equivalent to assuming that the objective optical system is chosen such that it eliminates the \hat{y} defocus. Consequently, we will ignore the degenerate \hat{y} direction in our discussion. Although this assumption may not be strictly true, our experimental results demonstrate that the effect of \hat{y} defocus is negligible in practice. Alternatively, one could incorporate a cubic or logarithmic phase mask [38, 99] into the volume hologram to deliberately extend the depth of field and eliminate defocus. However, a detailed discussion on wavefront coding techniques to extend the depth of field of volume holograms is beyond the scope of this paper.

In Fig. 2-33, we see that a broadband VHI system has very little Bragg selectivity in the longitudinal direction *i.e.* the longitudinal PSF is almost flat with very little drop of diffracted power observed with defocus. Consequently, it is not possible to recover the longitudinal position of a broadband object by simply monitoring the diffraction intensity on a powermeter. Thus the broadband VHI image is somewhat similar to an image from a lens with large depth of field in the sense that an object remains in focus with little change in image intensity over a long displacement.

However, the volume hologram and lens differ fundamentally in the way they form images. A lens is a linear shift-invariant system [2] that can map an object plane to an image provided certain conditions are satisfied (the lens-law for example). For an achromatic lens, the imaging operation is independent of the wavelength of the illumination and no color dispersion is observed in the image plane.

On the other hand, the Bragg selectivity of the volume hologram makes it strongly shift-variant. Only Bragg matched sources are imaged in a PR-VHI system. Consider a point emitting at a relative wavelength μ . The point source has to satisfy a location constraint [85]

$$x = \frac{f\theta_s(1 - \mu)}{2}. \quad (3.9)$$

in order to be Bragg matched and visible to the hologram, which follows from equation 2.69. This Bragg matched source is then imaged by the PR volume hologram to the detector location

$$x' = \frac{F\theta_s(1 + \mu)}{2}. \quad (3.10)$$

Alternatively, one can say that a point sensor located at x' measures contributions from all point sources along the line

$$x = f\theta_s \left(1 - \frac{x'}{F\theta_s} \right). \quad (3.11)$$

These contributions are dispersed according to (3.10). This is shown schematically in Fig. 3-6.

Consider a broadband object emitting over a bandwidth $\mu_c \pm \Delta\mu$. The broadband

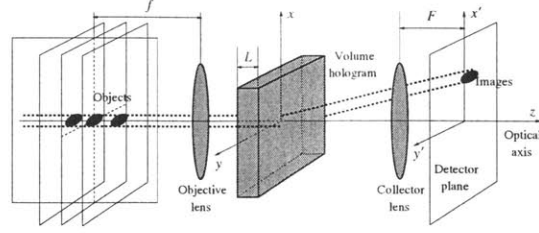


Figure 3-6: All voxels located along a line in the object space are mapped on to the same lateral location on the detector.

illumination results in a band of lines

$$x_c \pm \Delta x = \frac{f\theta_s(1 - \mu_c)}{2} \pm \frac{f\theta_s\Delta\mu}{2}, \quad (3.12)$$

that are mapped to the detector locations

$$x'_c \pm \Delta x' = F\theta_s \left(1 - \frac{x_c}{f\theta_s} \right) \pm \frac{F\Delta x}{f}. \quad (3.13)$$

From (3.12) and (3.13), we see that the broadband PR-VHI has a larger lateral field of view than the corresponding monochromatic PR-VHI sensor. Several lines similar to (3.11), each corresponding to a different wavelength, are simultaneously mapped to the detector to form a “Bragg rainbow.” As a result of this, the broadband PR-VHI images show significant color dispersion as different colors are mapped to different detector locations [84]. Further, this unique mapping method restricts the locus of possible locations that can contribute to a particular measurement point x' to a single line in the object space according to (3.11). This is shown in Fig. 3-7, where three different wavelengths are simultaneously imaged by the volume hologram.

However, at least two lines are required to triangulate the location of a point source. Thus, we need at least two PR-VHI sensors to determine a source location. We will discuss a general system with N PR-VHI sensors available for imaging.

Fig. 3-8 is a simplified schematic of N -ocular VHI. We depict $N = 3$ for illustrative purposes. The object is assumed to be 2D with an intensity distribution $I(x, z)$. We would like to reiterate here that the \hat{y} direction is degenerate and will be ignored

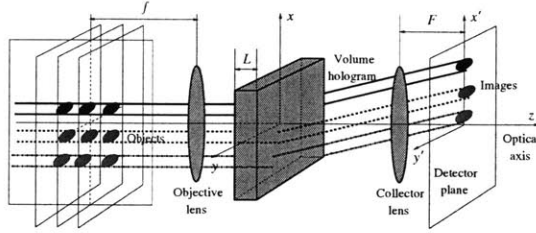


Figure 3-7: Several point sources that satisfy (3.12) are *simultaneously* imaged by the PR volume hologram according to (3.13).

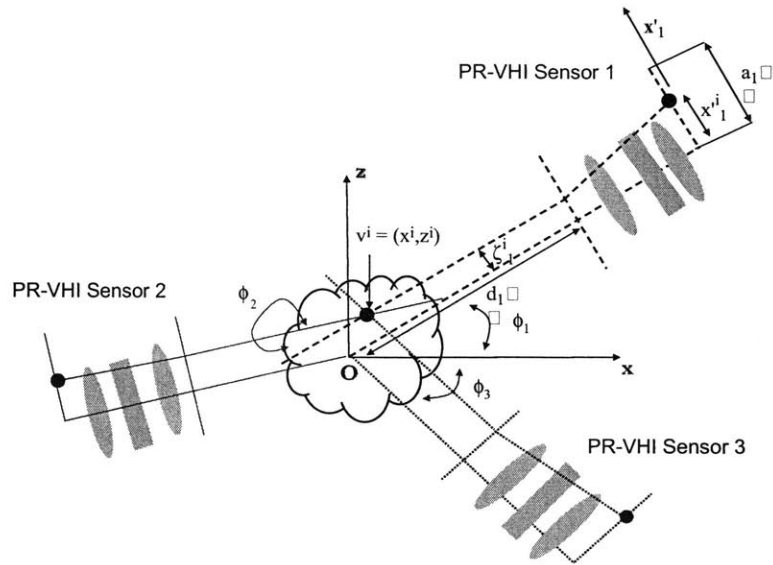


Figure 3-8: Inversion scheme to reconstruct 3D object data from 2D VHI images.

throughout this analysis. Several y -slices can be recovered simultaneously by using a detector array with several rows of pixels.

The point of intersection of the optical axes of the different PR-VHI sensors is taken to be the origin O of the $x - z$ coordinate system shown (Note that the assumption that the optical axes of all the VHI sensors intersect at O simplifies our analysis, but it is not necessary, as we discuss later). The optical axis of the j^{th} sensor is inclined at an angle ϕ_j with respect to the x axis and the sensor is located at a perpendicular distance d_j from O . The 1D detector array is a_j units long and the x'_j axis is oriented along the detector array. The detector returns a 1D measurement

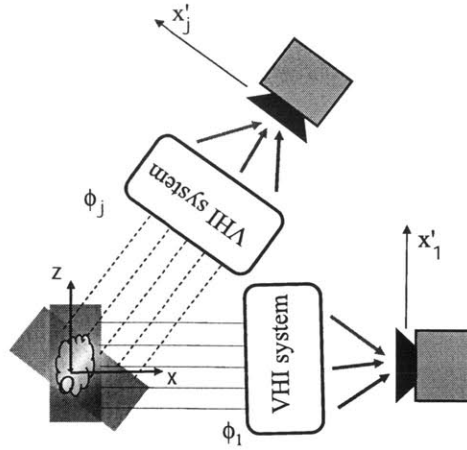


Figure 3-9: A broadband PR-VHI system measures the Radon transform of an object along a direction specified by the inclination of the sensor.

$I_j(x'_j)$ of the object.

Our goal is to recover the 2D intensity distribution $I(x, z)$ from the multiple VHI measurements. For this purpose, we choose an arbitrary point $\mathbf{v}^i \equiv (x^i, z^i)$ in the object and endeavor to recover the intensity $I^i = I(x^i, z^i)$ of this point from the 1D VHI measurements $I_j(x'_j)$ for $j = 1 \dots N$. We will discuss two inversion schemes suitable for this task in the following sections.

Inversion using the Fourier slice theorem

In this section, we discuss a scheme that performs 3D reconstruction by combining multiple PR-VHI images via the Fourier slice theorem. As before, the degenerate \hat{y} direction is neglected for this analysis. As mentioned earlier, the wavelength degeneracy of volume holograms ensures that all the voxels that lie at the same transverse ($\hat{\mathbf{x}}$) location are mapped to the same pixel (\mathbf{x}') location on the CCD. This is shown in Fig. 3-9. If the longitudinal PSF of the VHI system is approximately flat over the extent of the object of interest, we can see that the pixel located at (3.10) measures a line integral in object space of point sources located along (3.9). This is exactly the Radon transform of the 3D object for the j^{th} sensor inclined at an angle ϕ_j . Multiple sensors measure the Radon transform in different directions. The actual structure of

the object can be recovered by inverting the Radon transform data using the Fourier slice theorem and the filtered backprojection algorithm [100].

We now present some experimental results to demonstrate N -ocular VHI imaging and the accompanying 3D reconstruction. In the experimental setup used to implement N -ocular PR-VHI, the object of interest was placed on a computer controlled rotational stage (A Newport M-URM150 precision motorized stage controlled by a Newport ESP300 controller via Matlab). A single PR-VHI system similar to Fig. 2-33(a) with $f = 100$ mm, $F = 100$ mm and $a = 12.7$ mm was used to image the object. The volume hologram used was the same Aprilis photopolymer described in section 2.5. We obtained PR-VHI images from different perspectives by rotating the object and capturing the image on the CCD camera (This allowed us to use just a single PR-VHI sensor to obtain the N -ocular measurements and also ensured that the optical axes of the sensors always intersected). The object we imaged is shown in Fig. 3-10(a). Two fluorescent beads emitting at a bandwidth $\lambda_p = 580 \pm 20$ nm with diameters 0.66 mm and 0.72 mm were separated by an aluminum spacer of length 2.91 mm. The beads were translucent while fluorescing and hence useful to experimentally demonstrate 3D VHI. Figures 3-10(b) and (c) are sample VHI image captured by a CCD camera. The inclinations were $\phi_b = 0^\circ$ and $\phi_c = 45^\circ$ for the two images shown.

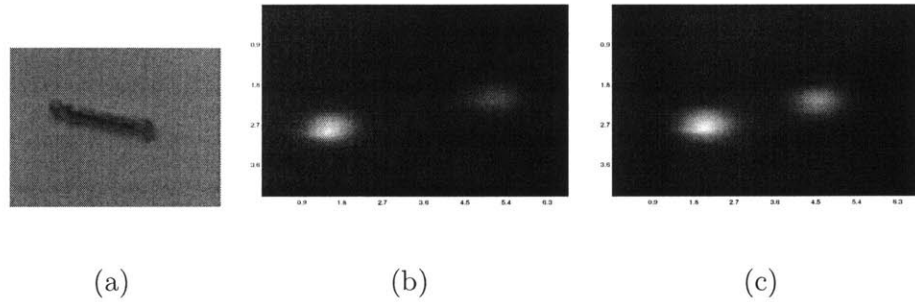


Figure 3-10: N -ocular PR-VHI of broadband objects. (a) The object of interest consisted of two fluorescent beads of diameter 0.66 mm and 0.72 mm separated by an aluminum spacer of length 2.91 mm. (b) and (c) are VHI PR-images of the object at inclination angles $\phi_b = 0^\circ$ and $\phi_c = 45^\circ$ respectively.

Figure 3-11 shows the experimentally obtained reconstruction using measurements from 7 rotation angles $\phi = (0^\circ, 30^\circ, 60^\circ, 90^\circ, 120^\circ, 150^\circ, 180^\circ)$ and the filtered back-

projection algorithm. The choice of 7 perspective views with angular separation 30° between views was arbitrary. It would be interesting to study the tradeoff between the quality of the 3D reconstruction and the number of perspectives used for various SNR levels. However, such a study is beyond the scope of this discussion. Note that the $x - z$ “slices” of the reconstruction appear noisy because the filtered backprojection algorithm amplifies higher spatial frequencies. A regularized backprojection scheme can suppress these noise artifacts.

The separation in between the centers of the two beads that constituted the object was $\Delta = 3.60 \pm 0.02$ mm. The margin of error is on account of the resolution of the callipers that were used to measure the object. We chose to compare the separation between the intensity centroids of the reconstructed beads with Δ as a metric to evaluate the efficacy of the reconstruction method. We calculated the distance in between the centroids of the beads in the 3D reconstruction to be 3.60 ± 0.01 mm. The margin of error here corresponds to the size of a single voxel.

Thus, we see that the N -ocular PR-VHI sensor can accurately recover the 3D intensity distribution. We note that although the metric described above may not necessarily be the best method to describe the resolution of the N -ocular PR-VHI system, we believe that it does help experimentally validate the ability of N -ocular PR-VHI to resolve small object features. We are currently looking into other information-theoretic metrics [92] to characterize the quality of the 3D reconstruction.

Inversion using least-squares optimization

We saw in the last section that the backprojection algorithm can be used to obtain a 3D reconstruction from multiple PR-VHI images. We saw that the reconstructions were noisy because of the amplification of high spatial frequencies and thus more perspectives are required for accurate reconstructions. In this section, we discuss a least-squares optimization method to recover the object intensity. Consider Fig. 3-8 again. We limit our discussion to the PR-VHI sensor inclined at ϕ_1 for simplicity. From the geometry, the lateral location ζ_1^i of point $\mathbf{v}^i \equiv (x^i, z^i)$ with respect to the

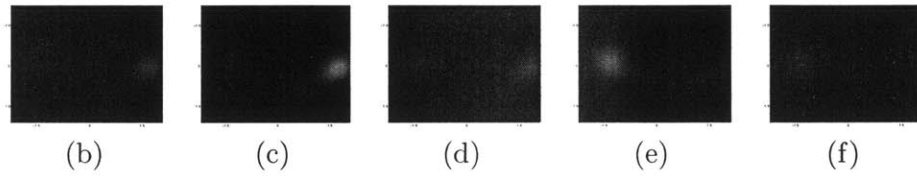
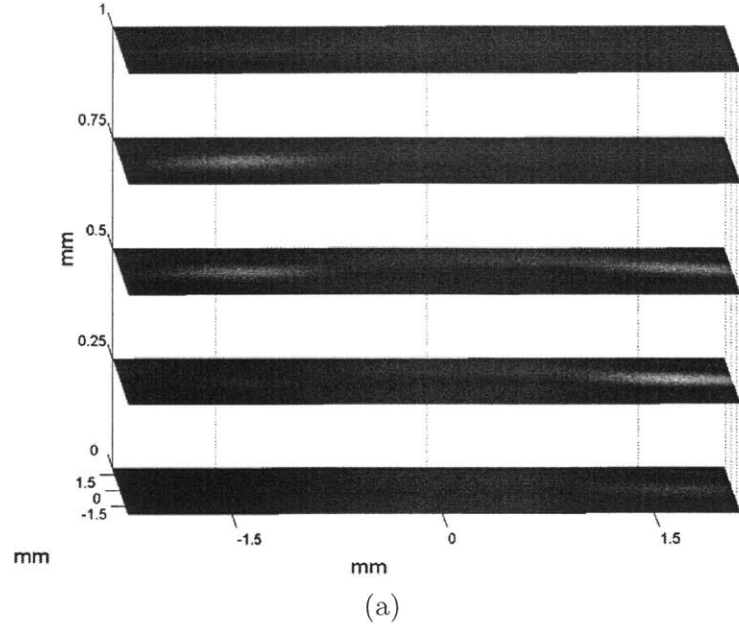


Figure 3-11: 3D image of object shown in Fig. 3-10 using the inverse Radon transform approach. (a) shows 5 slices through the object and (b) - (f) show the same slices at $y = 0, 0.25, 0.5, 0.75$ and 1 mm side by side. All dimensions are in mm. The separation between the centroids of the two reconstructed beads was calculated to be 3.6 ± 0.01 mm.

optical axis of sensor $j = 1$ is found to be

$$\zeta_1^i = x^i \cos \phi_1 - z^i \sin \phi_1. \quad (3.14)$$

The wavelength degeneracy of the volume hologram ensures that sources along a lateral line in the object space are *always* mapped to the same location on the detector as specified by (3.11). Substituting, we get

$$x_1^i = F\theta_s \left(1 - \frac{\zeta_1^i}{f\theta_s} \right). \quad (3.15)$$

The intensity measurement corresponding to this particular location is

$$\hat{I}_1^i = I_1(x_1^i). \quad (3.16)$$

We can calculate the measurement point and corresponding intensity for each of the other ($j \neq 1$) sensors as

$$x_j^i = F\theta_s \left(1 - \frac{x^i \cos \phi_j - z^i \sin \phi_j}{f\theta_s} \right) \quad (3.17)$$

$$\hat{I}_j^i = I_j(x_j^i) \quad (3.18)$$

We take the desired intensity \hat{I}^i to be the value that minimizes the mean square error [100] of the different measurements

$$\hat{I}^i = \arg \min \left[\sum_j \left(\hat{I}^i - \hat{I}_j^i \right)^2 \right] \quad (3.19)$$

This operation results in a least-square estimate for $I(x^i, z^i)$. This procedure is repeated for all points to recover the entire 2D intensity distribution $I(x, z)$.

It is useful to reiterate here that equations (3.17) and (3.18) are only valid because the volume hologram automatically establishes correspondence by virtue of the wavelength degeneracy. This approach would not work for a simple lens system without establishing correspondence between multiple images prior to the inversion.

As we mentioned earlier, the assumption that the optical axes of the multiple sensors intersect is not necessary. Sensors with non-intersecting axes still yield equations similar to (3.17), however in this case x_j^i needs to be modified by taking the actual location of the optical axis into account. If the optical axis of the VHI sensor is located at a perpendicular distance χ from O , equation 3.17 is rewritten as

$$x_j^i = F\theta_s \left(1 - \frac{\chi + (x^i \cos \phi_j - z^i \sin \phi_j)}{f\theta_s} \right) \quad (3.20)$$

Figure 3-12 shows the experimentally obtained reconstruction of the object of

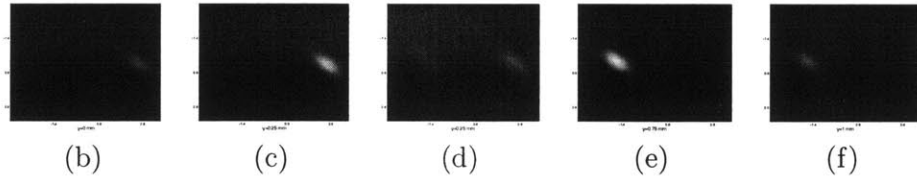
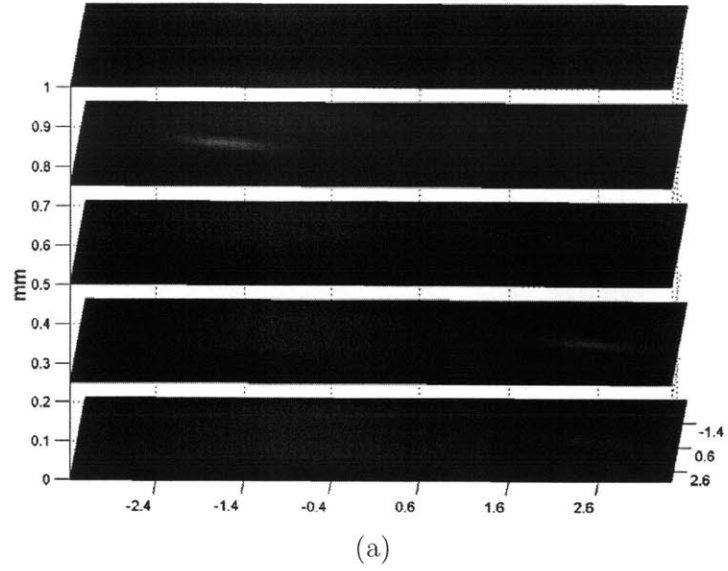


Figure 3-12: The least squares inversion is able to recover the object shown in Fig. 3-10(a) shows 5 slices through the object and (b) - (f) show the same slices at $y = 0, 0.25, 0.5, 0.75$ and 1 mm side by side. All dimensions are in mm.

Fig. 3-10(a) using 5 rotation angles $\phi = (0^\circ, 30^\circ, 45^\circ, 60^\circ, 90^\circ)$. The different perspectives were obtained by angular scanning. The separation in between the centers of the two beads that constituted the object was 3.60 ± 0.02 mm. We calculated the distance in between the centroids of the beads in the 3D reconstruction to be 3.59 ± 0.01 mm. Thus, we see that the N -ocular PR-VHI sensor can accurately recover the 3D intensity distribution.

Chapter 4

Volume Holographic Imaging Systems

In this chapter, we demonstrate how a VHI system can be configured for diverse imaging applications ranging from surface profilometry to real time hyperspectral microscopy. We first describe various classes of imaging systems with particular emphasis on their VHI implementation and we then present various VHI systems that we have demonstrated and discuss each in detail.

4.1 Classification of VHI systems

A VHI system can be classified based on:

4.1.1 Type of object/illumination

The material properties of the object and the type of illumination determine the nature of the image as follows:

1. *Reflective surfaces* are opaque. A system imaging a reflective surface typically returns an image of the form $\{z(x, y), r(x, y)\}$. The function r specifies the reflectivity of the surface as a function of the lateral coordinates (x, y) . The function $z(x, y)$ is referred to as the surface “profile” of the object and the

imaging instrument is called a surface profilometer.

2. *3D point scatterers* consist of a several small point sources distributed over a volume. A system imaging this object returns an image $I(x, y, z)$ where the function I specifies the scattering strength at object location (x, y, z) . Fluorescent particles suspended within a fluid are a good example of this kind of object.
3. A *3D translucent/absorptive object* has some refractive index and absorption variation within the object volume. A system imaging this object would return an image $n(x, y, z) + i\alpha(x, y, z)$ where n refers to the refractive index and α the absorption coefficient at object location (x, y, z) . Tomographic imaging systems like MRI are used to image 3D absorptive objects.

Further, the nature of the illumination used for imaging can be classified as:

1. *Active illumination* relies on external sources to pump light to the object. The imaging system collects the reflected/backscattered light for imaging.
2. *Passive illumination* schemes rely on either self-luminescence or ambient light to provide the necessary illumination for imaging.

VHI can be implemented for all of these classes of objects and illumination as we discuss later in section 4.2.

4.1.2 Single hologram / Many multiplexed holograms

The Bragg selectivity property of volume diffraction allows several gratings to be multiplexed inside the same volume of the photosensitive material [65]. This means that a VHI system can comprise

1. One single volume holographic grating that acts as a lens for imaging or,
2. Several gratings *i.e* several lenses multiplexed [101] within the same volume element. Each of these gratings can independently process the optical information; this reduces both the back end digital computation and the scanning time

required. However, there is a tradeoff involved since the diffraction efficiency decreases [102] as the number of multiplexed gratings increase.

We discuss both schemes later in section 4.2.

4.1.3 Single / Multiple VHI sensors in the imaging system

The resolution of VHI, like most other imaging systems, degrades [1] with increasing object distance. Often, traditional lens based imaging systems use triangulation methods to accurately determine depth information about objects even though each sensor by itself can image only in 2D. In triangulation [44], several sensors image the same object from different directions. The different images are combined geometrically to yield a high resolution profile the object. A similar approach can be used for VHI to offset the degradation of depth resolution by using multiple VHI sensors to acquire different perspectives of the object of interest and improve image resolution by reconciling these perspectives into one consolidated image. Thus, a VHI system could comprise

1. A *single VHI sensor* to acquire the object information on its own or,
2. *Multiple VHI sensors* to acquire multiple perspectives of the same object. The perspectives can be reconciled using various numerical techniques such as point-multiplication of the individual point spread functions (PSFs), least squares error optimization or an expectation maximization algorithm. We refer to this setup as N -ocular VHI.

We discuss both single and N -ocular VHI schemes in section 4.2.

4.1.4 Type of objective optical system

A volume hologram is very sensitive to the incident illumination and diffracts only the Bragg matched components of the illumination. Often, it is possible to manipulate the illumination to Bragg match the hologram at different object distances by using specific objective optical systems, for instance,

1. *Microscope objective optics* placed in front of the volume hologram can configure the VHI system to image objects at short working distances with very high resolutions.
2. *Telescope and telephoto objective optics* placed in front of the hologram can configure the VHI system to image objects at long working distances also with high resolution.

We will discuss both microscope and telescope schemes in section 4.2.

4.2 VHI implementations

Volume holograms possess Bragg selectivity which helps a VHI system to optically segment [5] the object space and selectively identify special attributes (for instance spatial locations, spectral signatures etc.) of interest. We have previously [90] derived the impulse response as a function of axial defocus for both SR and PR-VHI systems. In chapter 2, we derived the diffracted field intensity as a function of the detector coordinates for an SR-VHI system. The result was (2.14) and is rewritten here for clarity

$$\frac{I(x', y'; \delta)}{I_b(\theta_s f_2, 0; \delta)} = \left| \mathcal{L} \left(\frac{2\pi a^2 \delta}{\lambda d^2}, \frac{2\pi a}{\lambda f_2} \sqrt{(x' - \theta_s f_2)^2 + y'^2} \right) \operatorname{sinc} \left(\frac{(x'^2 + y'^2 - (\theta_s f_2)^2)L}{2\lambda f_2^2} \right) \right|^2. \quad (4.1)$$

Similarly, for a PR-VHI system the diffracted field intensity from (2.37) is

$$\frac{I(x', y'; \delta)}{I_b(\theta_s f_2, 0; \delta)} = \operatorname{circ} \left(\frac{\sqrt{(x' - \theta_s f_2)^2 + y'^2}}{f_2 a \delta / f_1^2} \right) \operatorname{sinc}^2 \left(\frac{L \theta_s}{\lambda} \left(\frac{x'}{f_2} - \theta_s \right) \right). \quad (4.2)$$

The corresponding depth resolutions are:

$$\Delta z_{\text{FWHM}}(\text{SR-VHI}) = \frac{18.2d^2\lambda}{a^2\theta_s L}, \quad (4.3)$$

and

$$\Delta z_{\text{FWHM}}(\text{PR-VHI}) = \frac{5.34d^2\lambda}{a\theta_s L}. \quad (4.4)$$

VHI systems in several of the sub-categories mentioned in section 4.1 have been designed based on the simple SR and PR-VHI models. We present a brief overview and working principle for each implementation.

4.2.1 {Reflective object + Active illumination, Single hologram, Single sensor, No objective optics}

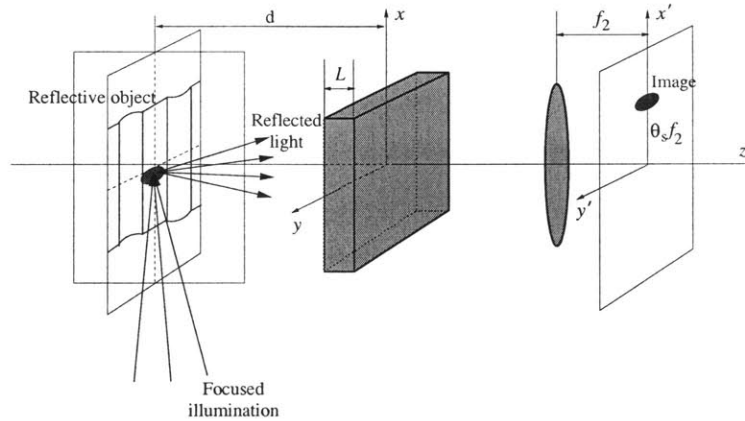


Figure 4-1: VHI for {Reflective object + Active illumination, Single hologram, Single sensor, No objective optics}. An intensity detector monitors the beam by the SR hologram diffracted while the object is scanned in 3D.

Figure 4-1 is the setup for stand-alone VHI without any objective optics. The single volume hologram is recorded using a spherical reference and planar reference beam that is inclined at an angle θ_s with respect to the optical axis. The origin of the spherical reference is the Bragg matched location for the SR-VHI system. The impulse response of the SR-VHI system is known [90] and the resolution has been verified experimentally [90, 82].

The surface profile is recovered as follows: A laser beam is focused on the object surface and the SR-VHI system captures the reflected light. If the focused spot lies exactly on the object surface, the SR-hologram is Bragg matched and a strong diffracted signal is measured. On the other hand, if the focused spot does not coincide with the object surface, the volume hologram is Bragg mismatched and the diffracted

signal is much weaker. The entire object surface is recovered by scanning completely in 3D by moving the focused spot.

Figure 4-2 [90] presents SR VHI images of an aluminum artifact which we fabricated specifically for this purpose. The artifact consisted of the three letters “MIT” at different heights as a staircase with 2mm step size. “M” was the tallest letter and “T” the shortest. A CAD rendering from the model used to machine the artifact is given in Figure 4-2(a). 3D scanning was performed using three orthogonal Newport CMA-25CCCL actuators and a Newport 2832C power meter, both controlled through National Instruments’ Labview software.

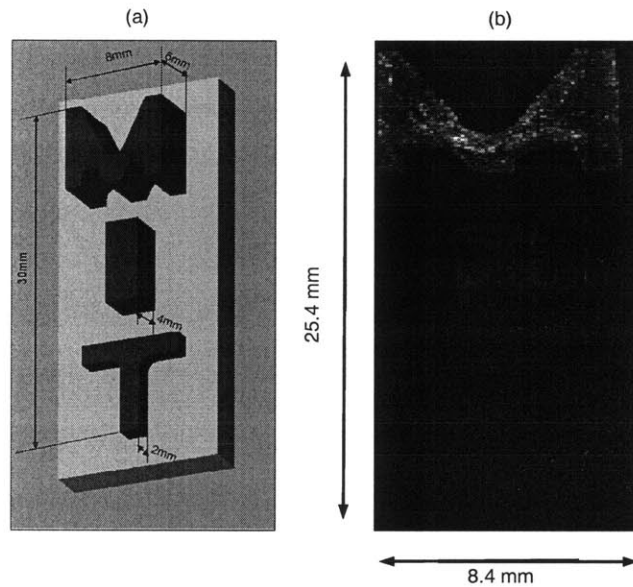


Figure 4-2: Experimental VH image of a fabricated artifact obtained using 2 mm thick crystal of LiNbO_3 with diffraction efficiency $\eta \approx 5\%$ recorded at $\lambda = 532 \text{ nm}$. The working distance $d = 5 \text{ cm}$; $a = 3.5 \text{ mm}$; $\theta_s = 30^\circ$ and $\Delta z_{\text{FWHM}} \approx 1 \text{ mm}$. (a) is the actual CAD rendering of the object and (b) is a volume holographic image of the object obtained by a complete lateral scan with surface of the letter M being placed at Bragg matched location, which consequently appears to be bright.

Figure 4-2(b) shows a point-by-point scan using a pixel size of $100 \mu\text{m}^2$ of the artifact at the reference height of the letter M (*i.e.*, the surface of this letter was Bragg matched during the scan.) The letters I and T are consequently weaker because they were mismatched. To quantify the Bragg mismatch, we averaged numerically the

intensities obtained experimentally over the entire bright part of the matched letter M and compared with the corresponding values for the mismatched letters I and T. We will denote these values as P_M , P_I and P_T , respectively. From the experiment we found $P_M = (5.82 \pm 2.7) \times 10^{-7}$, $P_I = (1.35 \pm 0.67) \times 10^{-7}$, and $P_T = (0.79 \pm 0.25) \times 10^{-7}$. The ratios

$$\frac{P_I}{P_M} = 0.23 \pm 0.22$$

$$\frac{P_T}{P_M} = 0.13 \pm 0.07$$

are slightly higher compared to the estimates from the PSF calculation and experiments of Figure 2-6. This is because point scanning is susceptible to surface irregularities on the artifact. At local rough spots, most of the scattered light does not reach the detector. This effect is evident in the high values of standard deviation for P_M , P_I and P_T .

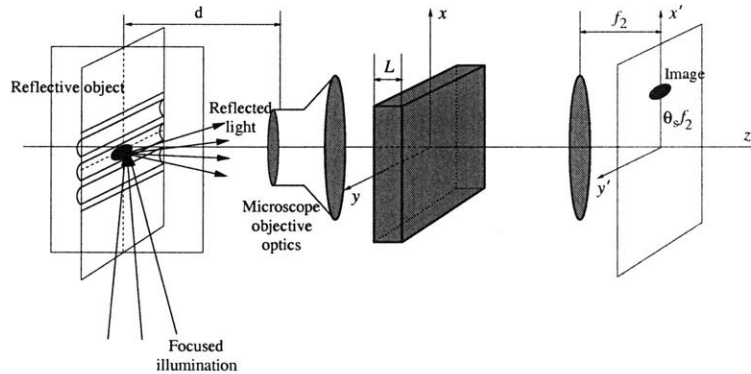


Figure 4-3: VHI for {Reflective object + Active illumination, Single hologram, Single sensor, Microscope optics}. The microscope objective collimates the light reflected from the surface and an intensity detector monitors the diffracted beam as the active probe is scanned with respect to the object.

4.2.2 {Reflective object + Active illumination, Single hologram, Single sensor, Microscope objective optics}

Figure 4-3 shows the schematic for VHI with microscope objective optics. A single PR-volume hologram is used. The imaging is done by focusing laser light on the surface of reflective object. The light reflected by the object surface is collected by a microscope objective lens placed in front of the hologram. If the focused spot on the surface lies at the front focal point of the microscope lens, the light is collimated and a Bragg matched plane wave is incident on the hologram.

The detector monitors the diffracted beam from the hologram as the object is scanned in 3D to recover the entire surface profile. Fig. 4-4 shows experimental results for PR-VHI with microscope objective optics. The object is an analog tunable MEMS grating. The grating was located at a working distance of $d = 2$ cm from the microscope objective and the depth resolution for the system was $\Delta z_{\text{FWHM}} \approx 2\mu\text{m}$.

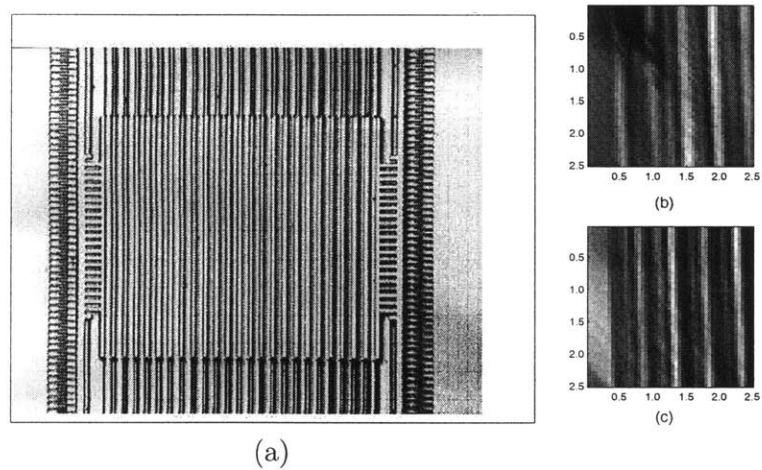


Figure 4-4: VH image of MEMS grating using microscope objective optics using the same LiNbO_3 crystal but recorded with a normally incident planar reference beam instead of the spherical reference. The microscope objective optics had a working distance of $d = 2$ cm with $a = 0.5$ cm. (a) is a picture of MEMS grating being imaged; the height difference in between the top and bottom of the reflective grating is $24\mu\text{m}$. (b) VH image with laser point focused on the bottom of the grating and (c) VH image after the focus is raised $24\mu\text{m}$ to focus on the top of the grating surface. Note that there is a complete contrast reversal to indicate that the surfaces are indeed at different heights.

4.2.3 {Reflective object + Active illumination, Single hologram, Single sensor, Telescope/telephoto objective optics}

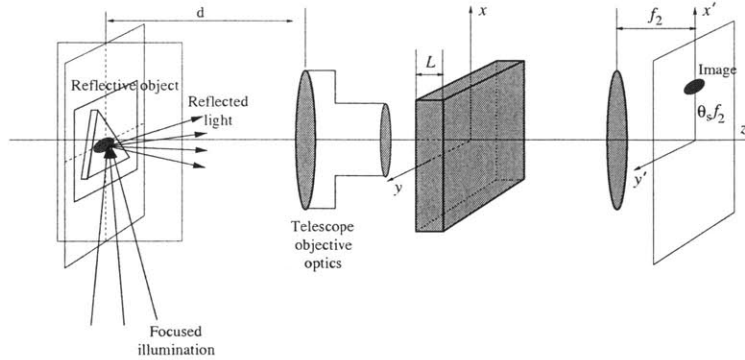


Figure 4-5: VHI for {Reflective object + Active illumination, Single hologram, Single sensor, Telescope optics}. The telescope creates a real image of the distant object in front of the SR hologram which then diffracts according to the Bragg condition. An intensity detector monitors the diffracted beam. The entire object surface is recovered by scanning.

Figure 4-5 shows the schematic for VHI with objective optics for long range surface profilometry applications. This scheme can be implemented for both SR and PR holograms. The depth resolution for most optical systems degrades quadratically with increasing object distance [1]. One way to offset this is by using optical elements with large apertures. This is expensive and impractical for volume holograms. A properly designed demagnifying telescope can have a large entrance pupil while ensuring that the field incident on the hologram placed behind the telescope is of the correct lateral extent. This permits us to increase the effective aperture of the imaging system and offset some of the degradation of depth resolution [82].

A PR-VHI system requires collimating objective optics to Bragg match the PR-hologram. In this case, a telephoto system can yield the optimal depth resolution [90] for a particular working distance. This is achieved by designing the objective optical system such that the first principal plane is as close to the object as possible. This reduces the effective focal length of the system and enhances the depth resolution to

the optimal diffraction limited value.

Fig. 4-6 [82] shows the surface profile of a MEMS-fabricated turbine located at a working distance $d = 16$ cm away from the aperture of the objective telescope. The demagnifying telescope allowed us to resolve surface features at a resolution $\Delta z_{\text{FWHM}} \approx 100\mu\text{m}$.

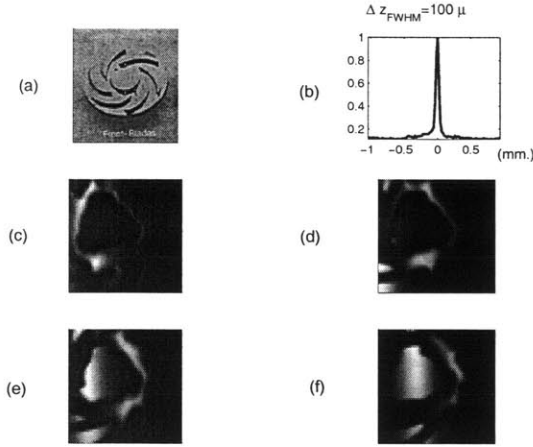


Figure 4-6: VH image of microturbine. The hologram was the same LiNbO_3 crystal described in Fig. 4-2. The telescope had angular magnification $M_\alpha = 1.5$ with $d = 16$ cm and $a = 1.2$ cm. (a) Image of the microturbine captured with a standard digital camera; the microturbine was manufactured to have surface height features of $225\mu\text{m}$. (b) Experimental depth response for a point source object at the same distance $\Delta z_{\text{FWHM}} \approx 100\mu\text{m}$; (c - f) VH telescope scans at progressive increments of $100\mu\text{m}$ through the object. At any given depth, the Bragg-matched portions of the object are brightest.

4.2.4 {Reflective object + Active illumination, Single hologram, Single sensor, Inclined telephoto objective optics}

Figure 4-7 is a schematic for active VHI for reflective objects incorporating a priori object information to enhance depth resolution. It was noted in section 4.2.3 that telephoto objective optics can achieve the optimal diffraction limited depth resolution for a particular working distance when nothing is known in advance about the object.

However, it is possible to incorporate a priori object information and enhance depth resolution even more. For instance, consider the case when it is known that the

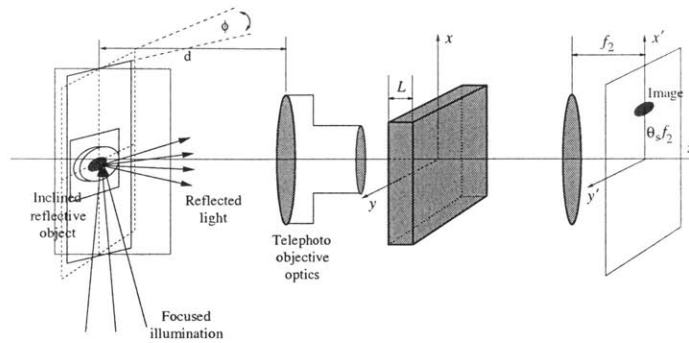


Figure 4-7: VHI for {Reflective object + Active illumination, Single hologram, Single sensor, Inclined telephoto optics}. If it is known that the object consists only of flat surfaces, depth resolution can be improved by inclining the object surface with respect to the scanning direction at an angle ϕ as indicated. This approach exploits the superior depth resolution to improve the apparent depth resolution.

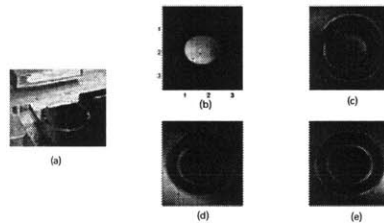


Figure 4-8: Surface scan of nanogate which has surface features $\approx 150\mu\text{m}$ using an inclined telephoto PR-VHI sensor with $d = 46\text{ cm}$ (a) Image of nanogate captured using standard CCD, (b) PR-VHI image of device with the top surface in focus, (c)& (d) PR-VHI images focused $50\mu\text{m}$ and $100\mu\text{m}$ below the top surface. (e) PR-VHI image focused on the base of the turbine $150\mu\text{m}$ below the top surface. Note that there again is a complete contrast reversal in between images (b) and (e).

reflective object consists of segments of flat surfaces [83]. In this case, a single PR-VHI sensor inclined with respect to the object surface can achieve substantially better depth resolution. This is possible because the a priori knowledge of the object surface allows us to translate the superior lateral resolution of the telephoto PR-VHI system into an “apparent” depth resolution by scanning the object in a direction that is inclined with respect to the object surface. Fig. 4-8 [83] shows the surface profile

of a MEMS device, the nanogate [103] located at a working distance of $d = 46$ cm measured using an inclined PR-VHI sensor inclined at angle $\phi = 30^\circ$ with respect to the object surface. This sensor can resolve depth features at a resolution $\Delta z_{\text{FWHM}} \approx 50\mu\text{m}$.

4.2.5 {Reflective object + Active illumination, Single hologram, Two sensors, Telescope objective optics}

The 3D resolution of a stand-alone hologram imaging a reflective target is comparable to triangulation based binocular imaging systems with considerable angular separation between the two cameras [82]. The resolution of VHI systems can be even further improved using multiple VHI sensors to look at the same object, as shown in Fig. 4-9. The multiple images are reconciled by point multiplying the PSF of each image. The resulting image has better resolution [104] because of the measurement is now overconstrained by the multiple measurements.

There are several ways to combine the multiple measurements by using digital processing like least squares optimization, expectation maximization etc. The point multiplication method was implemented in the experiment of Fig. 4-10. Note that the point multiplied image has better resolution than both the normal VHI and the inclined VHI sensor. However, the improvement over the inclined sensor is only marginal because the inclined sensor itself has excellent resolution. This was discussed in section 4.2.4.

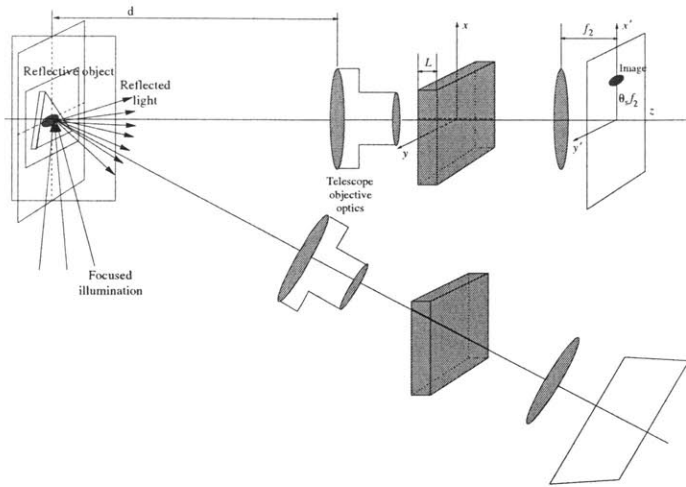


Figure 4-9: VHI for {Reflective object + Active illumination, Single hologram, Multiple sensors, Telescope optics}. Multiple VH sensors similar to the one described in Fig. 4-6 are used to simultaneously image the object. This leads to overconstraining the solution to the imaging inverse problem and results in better resolution.

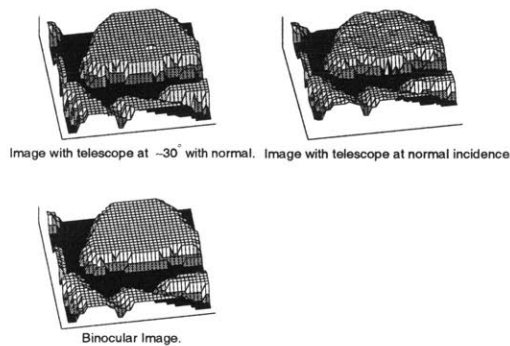


Figure 4-10: Surface profiles obtained using two VHI sensors imaging the turbine described in Fig. 4-6. One sensor was normal to the turbine surface, the other was inclined at an angle $\phi = 30^\circ$ with respect to the turbine surface. The resultant binocular VH image is obtained by point multiplying the individual images. Note that there is a significant improvement in between the binocular and normal VHI images. However, the improvement is not as discernible in between the inclined sensor and the binocular image on account of the phenomenon described in section 4.2.4.

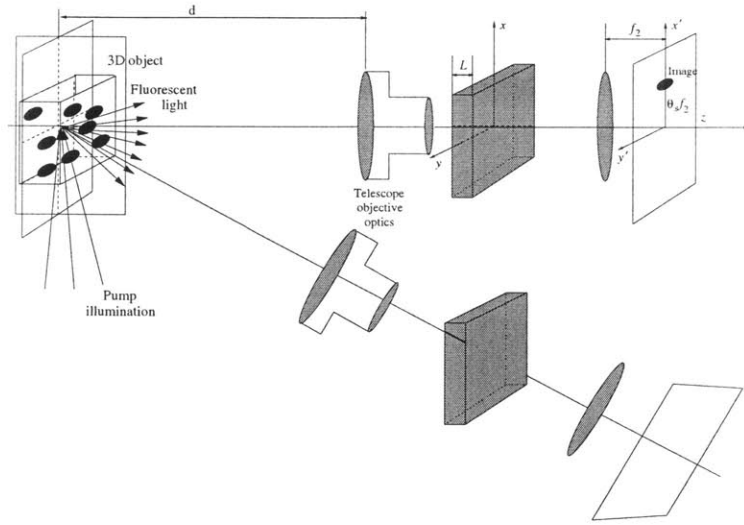


Figure 4-11: VHI for {3D fluorescent object + Active illumination, Single hologram, Multiple sensors, Telephoto optics}. Multiple VH sensors similar to that described in Fig. 4-8 acquire different perspectives of the fluorescent 3D object. The multiple measurements allow for an over-constrained solution to overcome the degradation of depth resolution on account of the broadband nature of the fluorescence.

4.2.6 {3D fluorescent object + Active illumination, Single hologram, Three sensors, Telephoto objective optics}

Figure 4-11 is the schematic for VHI of a 3D point scatterer type object. The individual sources in this case are small beads that fluoresce on being pumped by laser illumination. Each of the three VHI sensors contains a single PR-hologram with telephoto objective optics for collecting the fluorescent light. The bandwidth of the fluorescent light results in an increased field of view (FOV) with accompanying degradation of depth resolution [84, 85].

In this case, it is beneficial to use reconcile the three VHI images using a least squares optimization to obtain the actual 3D intensity distribution of the object. The experimental results are shown in Fig. 4-11 [105]. The 3D object was a helical arrangement of fluorescent beads that was recovered by three VHI sensors by over-constraining the measurements using a matrix pseudo-inverse method.

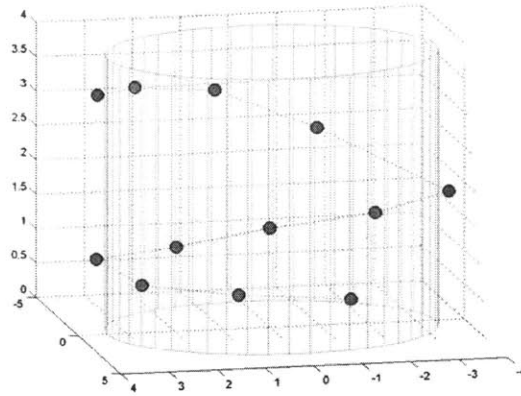


Figure 4-12: 3D image of a set of fluorescent particles arranged in a helical pattern. The object was located at a working distance of $d = 10$ cm from three broadband N -ocular PR-VHI sensors. The image inversion was done using pseudo inverse techniques.

4.2.7 {Reflective object + Broadband passive illumination, Single hologram, Single sensor, Telephoto objective optics}

Figure 4-13 shows the schematic when a reflective object is used with a single hologram VHI sensor under conditions of broadband illumination at a long working distance. The volume hologram still has some depth resolution on account of Bragg selectivity. However, the broader the illumination bandwidth, the worse the depth resolution [85]. As a result, it is not advisable to image reflective objects using broadband VHI on account of the reduced contrast and depth resolution. This is shown in Fig. 4-14, which compares the contrast between surfaces for the same object as the illumination bandwidth is increased. The object is the bottom chassis of a toy car. Notice that the contrast between object surface features at different heights degrades as the illumination bandwidth is increased.

However, this phenomenon can be exploited to build VHI based spectrum analyzers to measure the spectral profile of the illumination [85]. We shall discuss this in section 4.3

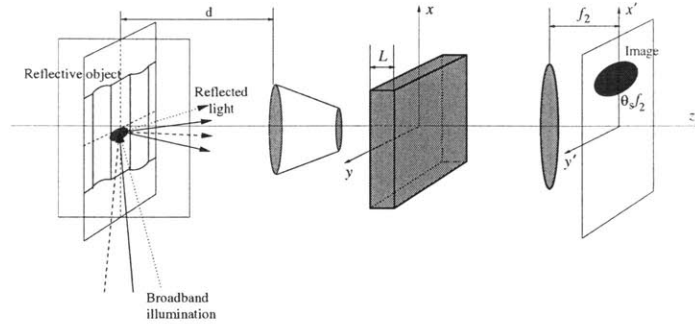


Figure 4-13: VHI for {Reflective object + Broadband illumination, Single hologram, Single sensor, Telephoto optics}. Increased illumination bandwidth improves the field of view of the VHI system thus reducing the amount of scanning required. However, this is accompanied by degradation of the depth resolution.

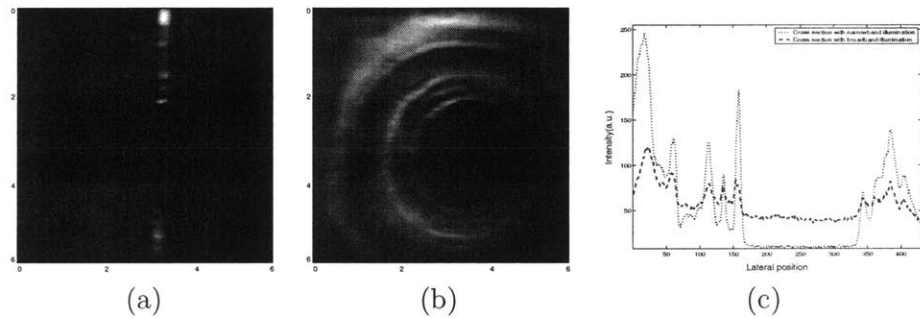


Figure 4-14: From section 2.5, surface profiles obtained using broadband illumination and PR-VHI. The object is the bottom chassis of a toy car of Fig. 2-35 . The particular region of interest is a raised screw on the chassis. (a) is the VH image obtained under narrowband illumination whereas in (b) the field of view improves under broadband illumination. However (c) indicates that the depth resolution degrades as the illumination bandwidth increases *i.e.* there is a price to pay for the enhanced field of view with respect to poorer depth discriminating ability.

4.2.8 {3D fluorescent object + Active illumination, Multiple holograms, Single sensor, Microscope objective optics}

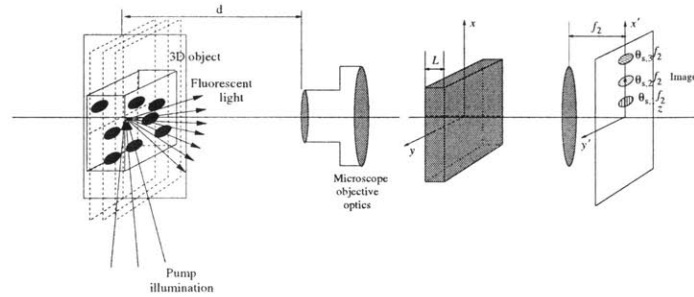


Figure 4-15: VHI for {3D fluorescent object + Active illumination, Multiple holograms, Single sensor, Microscope optics}. Multiple gratings can be recorded inside the same hologram volume. This results in reduced scanning as the VHI system can simultaneously image multiple locations within the object. This is illustrated in the figure. There are three multiplexed gratings, each observing a different depth slice of the object and then diffracting to a different location on the detector. Thus, the VHI system can simultaneously monitor three locations without any scanning.

Figure 4-15 is the schematic of a real time hyperspectral microscope [84]. The object is a 3D distribution of fluorescent beads. Three PR-holograms are multiplexed inside the holographic material. Each hologram is Bragg matched at a different depth and diffracts in a direction specified by the corresponding recording signal beam. As a result, this VHI system can simultaneously image multiple depth layers of the 3D object. Moreover, since the fluorescent illumination is broadband, it is possible to image wide slices of each layer. The width of the slice depends on the fluorescence bandwidth. The experimental results of imaging three slices are shown in Fig. 4-16. To our knowledge, this is the first experimental demonstration of a real time hyperspectral microscope in three spatial dimensions.

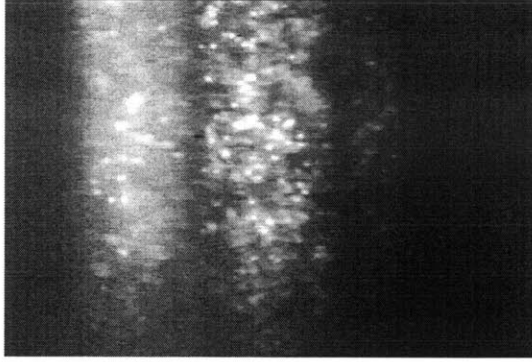


Figure 4-16: Experimental demonstration of real time hyperspectral microscope. Three holograms were multiplexed within the same volume to look at three different depth layers of a 3D object that consisted of fluorescent microspheres of diameter $15\mu\text{m}$. The Bragg selectivity of the hologram allows us to simultaneously image three depth slices (one slice is much fainter than the other on account of some recording irregularities); the width of each slice corresponds to the fluorescence bandwidth.

4.3 Volume holographic spectrometer

We now examine the operation of a volume hologram as a spectrometer. Consider the schematic of Fig. 4-17, where the specimen of unknown spectrum is placed at the front focus of the objective lens. The PR-VHI system is designed so that the width of the Bragg slit is smaller than the pixel size on the detector to reduce crosstalk between two adjacent wavelengths. In other, the detector pixel width $\Delta x'$ must satisfy

$$\Delta x' \geq \frac{F\lambda_{p,\max}}{L\theta_s}. \quad (4.5)$$

In (4.5), $\lambda_{p,\max}$ is the longest wavelength that the PR-VHI system can map onto the detector, and it is limited by the aperture of the objective lens. Additionally, the wavelength resolution of the PR-VHI spectrum analyzer $\Delta\lambda_p$ is

$$\Delta\lambda_p = \frac{2\lambda_f\lambda_{p,\max}}{L\theta_s^2}. \quad (4.6)$$

The k -sphere formulation[95] can also be used to design a PR-VHI spectrum analyzer and is a very useful graphical construct to understand the behavior of the system.

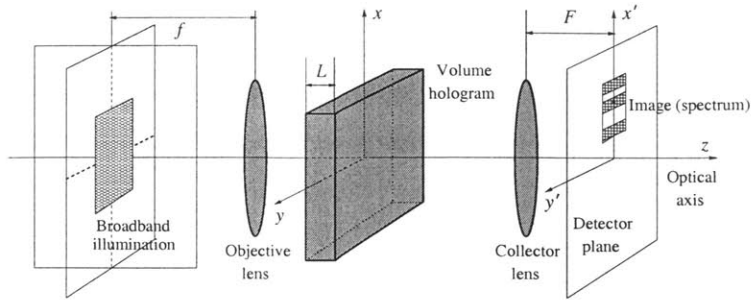


Figure 4-17: Schematic of PR-VHI spectrometer. The illumination whose spectrum is unknown is placed at the Bragg matched plane of the PR-VHI system; the illumination spectrum is the measured 1D intensity function (appropriately scaled) on the detector.

We will not go into the details of the k -sphere in this thesis but more information can be found in [86].

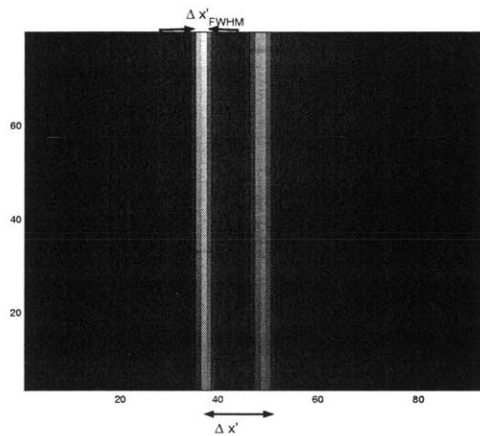


Figure 4-18: Measured spectrum using two narrow bandpass optical filters 488 ± 10 nm and 532 ± 10 nm (green). The separation in between the green slit and blue slit corresponds to 43.92 nm and the actual wavelength separation is 44 nm.

We experimentally implemented the simple PR-VHI spectrum analyzer of Fig. 4-17. The illumination was a broadband incoherent white light source manufactured by Cuda Inc. Different narrow bandpass spectral filters were alternately placed at the focal plane of the objective lens of focal length $f = 100$ mm. The volume hologram was recorded in a crystal of LiNbO_3 using two mutually coherent beams ($\lambda_f = 532$

nm): A normally incident reference and a signal beam inclined at an angle $\theta_s = 16^\circ$ with respect to the normal. A Jai CV235 industrial CCD camera with was used to capture the diffraction patterns. Each camera pixel was $9\mu\text{m}$ wide and 8 pixels were binned together to form a single spectral measurement pixel of width $\Delta x' = 72\mu\text{m}$. We chose $F = 75$ mm to satisfy $\lambda_{p,\text{max}} = 540$ nm in (4.5). From, these values, the spectral resolution was estimated from (4.6) to be $\Delta\lambda_p \approx 3.66$ nm. Figure 4-18 shows the Bragg slits observed on the camera using the PR-VHI system. Each slit corresponds to one bandpass spectral filter. The filter used were 488 ± 6 nm (blue) and 532 ± 6 nm (green). The centers of the slits are separated by 12 pixels corresponding to a 43.92 nm difference in between the center wavelengths (the actual separation is 44 nm) and the full width at half maximum (FWHM) of each slit is approximately 3 pixels corresponding to a spectral width of 10.98 nm.

Chapter 5

Comparison of VHI with Other 3D Imaging Systems

So far, we have demonstrated that VHI systems can be configured for a wide range of imaging applications. In this chapter, we compare the performance of a VHI system with other systems that can image in 3D. We choose two systems to compare with VHI: a traditional lens-based binocular camera system and a pinhole based confocal microscope. The lens based binocular camera is the most commonly used system for computer vision and commercial profilometry applications. The confocal microscope is widely used in commercial 3D imaging systems. This chapter compares these systems with VHI in order to bring forth the advantages offered by VHI and also points out certain drawbacks associated with VHI.

5.1 Comparison of Depth Resolution

In this section, we compare the depth resolution (quantified by the Δz_{FWHM}) of a binocular system and a confocal microscope with a VHI system.

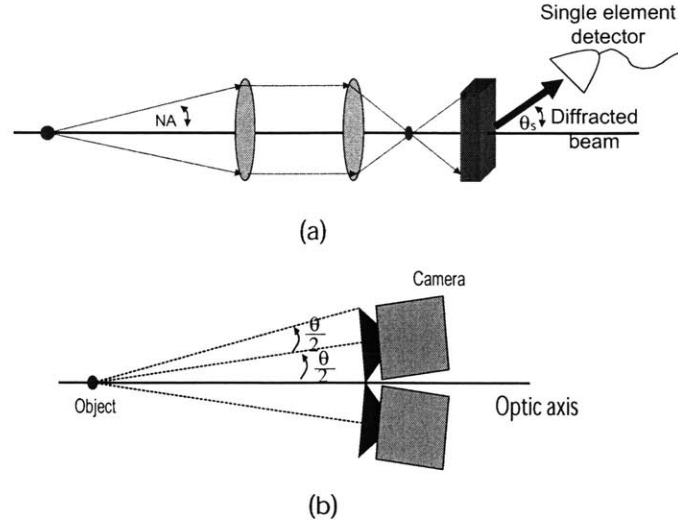


Figure 5-1: Setup for comparison of (a) VHI with objective telescope with (b) binocular system

5.1.1 Comparison of Δz_{FWHM} of a Binocular System and telescopic VHI system

Figure 5-1(a) shows the schematic of a VHI system with telescope objective optics. The lateral and longitudinal resolution [82] of a stand alone volume hologram (of thickness $L = 2\text{mm}$ corresponding to LiNbO_3 crystal used in the experiments) are given by

$$\Delta x_{FWHM} \approx \frac{0.5\lambda}{\theta_s \times NA} \quad \text{and} \quad \Delta z_{FWHM} \approx \frac{1.7\lambda}{NA^2}. \quad (5.1)$$

In equation (5.1), θ_s is the angle that the off axis signal beam makes with the optical axis, NA is the numerical aperture of the telescope objective optics and λ is the operating wavelength. For $NA \approx 3.581^\circ$, the telescope VHI system has depth resolution $\Delta z_{FWHM} \approx 100\mu\text{m}$ [82].

We have mentioned in chapter 1 that a single camera would not yield depth information for a similar setup. However, it is possible to obtain depth information by triangulating two camera pictures of the object at different angles with respect to the optical axis, as shown in Fig. 5-1(b). To compare the binocular imaging system

with the VH telescope of Fig. 5-1(a), it is important to ensure that the two systems operate under the same NA. Thus, we assume that the half-angle subtended by each camera is equal to the NA of the VH-telescope i.e. $\sin(\frac{\theta}{2}) = \text{NA}$. The depth resolution of the binocular system is given by

$$\Delta z_{\text{FWHM}} = \frac{\Delta x_{\text{FWHM}} \times M_{\alpha}}{\tan(\frac{\theta}{2})}, \quad (5.2)$$

where Δx_{FWHM} is the diffraction-limited lateral resolution of the camera. For the geometry of Fig. 5-1(b), the lateral resolution is limited by the aperture of the camera and is given by

$$\Delta x_{\text{FWHM}} = \frac{0.61\lambda}{\text{NA}_c}, \quad (5.3)$$

where $\text{NA}_c = \sin \frac{\theta}{2}$ is the numerical aperture of each individual camera. Substituting (5.3) in (5.2) yields a value of $\Delta z_{\text{FWHM}} \sim 250\mu\text{m}$. Thus we see that the VH telescope has better longitudinal resolution as compared to a standard binocular arrangement of the same numerical aperture.

5.1.2 Comparison of Δz_{FWHM} of a Confocal Microscope and VHI system

Fig. 5-2 compares the optimum depth resolution for a PR-VHI system with a SR-VHI system and a confocal (CF) system as function of working distance d on a log-log scale. We substitute the values $\theta_s = 13.6^\circ$, $L = 2$ mm, $a = 12.7$ mm, $r_{\min} = 100\mu\text{m}$ and pinhole radius $1.22\lambda d/4a$ in the expressions for depth resolution for each of these systems given by (2.47), (2.26) and (2.28) respectively. The resulting equations are

$$\begin{aligned} \Delta z_{\text{FWHM}}(\text{PR})_{\text{opt}} &= 1.5 \times 10^{-6} d^2, \\ \Delta z_{\text{FWHM}}(\text{SR}) &= 20.45 \times 10^{-6} d^2, \\ \Delta z_{\text{FWHM}}(\text{CF}) &= 3.50 \times 10^{-6} d^2. \end{aligned}$$

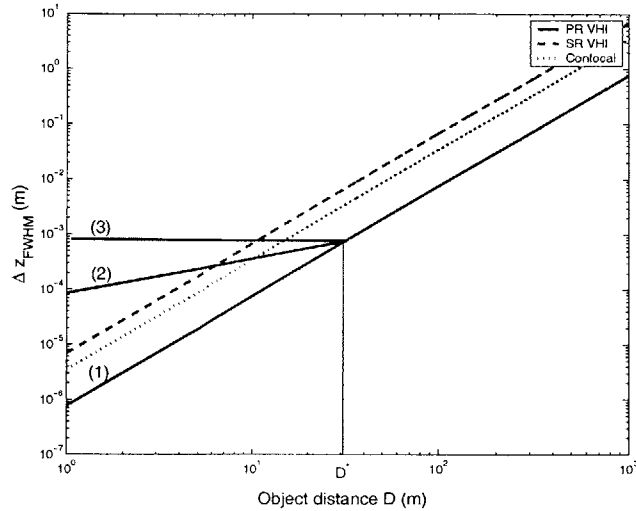


Figure 5-2: Plots of Δz_{FWHM} versus object distance d for PR VHI (solid lines), SR VHI (dashed line), Confocal systems (dotted line).

Thus, the PR-VHI system has better resolution than the confocal system which in turn has better resolution than the SR-VHI system. Additionally, it is possible to design zoom objective optics for a PR-VHI system to operate along the lines (1), (2) or (3) as shown in Fig. 5-2. Operating along (1) achieves the optimal depth resolution. However, if we are willing to sacrifice some depth resolution, the PR-VHI system can operate anywhere between lines (3) and (1). In (2), some depth resolution is sacrificed in order to ensure that the resolution degrades linearly with increasing $d < d^*$ and in (3), more depth resolution is sacrificed to ensure that the depth resolution stays constant over the range $0 \sim d^*$.

5.2 Information Theoretic Analysis of VHI

The ability to acquire three-dimensional (3D) information about objects non-invasively has led to significant advances in many scientific areas over the past two or three decades. Medical imaging and bioimaging have benefited especially from these developments. Optical, acoustical, magnetic, radiometric, etc. imaging have been employed widely in laboratories as well as clinically. Each modality has competitive

advantages in different applications or areas of interest. Optical imaging is necessary to accomplish spatial resolution of the order of a few micrometers, but it can be employed successfully only on objects with small absorption and scattering coefficients at the optical regime. Assuming that absorption and scatter do not present problems, the performance of an optical imaging system is still limited by several factors, such as the capabilities of the optical elements used to construct the system, the amount of optical power available from the object, and the post-processing of the image data. In this section we use a well-known image performance metric, Shannon's mutual information [106, 107, 108, 109], to model the performance of volume holograms [5, 81].

As mentioned earlier, the imaging of 3D objects is fundamentally an ill-posed problem, since detector arrays are necessarily two-dimensional. Several imaging techniques, e.g. confocal microscopy [14, 94], optical coherence tomography (OCT) [11], coherence imaging [110, 28, 35, 32, 36], etc. resolve the ill-posedness by limiting the 3D field of view and scanning across the 3D object. For example, a confocal microscope at any given instance in time acquires a point (zero-dimensional) measurement; volumetric reconstruction is obtained by scanning in three dimensions. The same is true for an OCT imager. A coherence imager, such as a rotational shear interferometer (RSI) can, in principle, acquire an entire two-dimensional cross-section at once; therefore, one-dimensional scanning suffices to reconstruct the object in 3D. Typically, however, additional scans need to be acquired in order to reduce phase noise in the data [34].

The principle of VHI is shown in Figure 5-3. The hologram is illuminated by the radiation from the object, and diffracts portion of the radiation towards a detection plane where one or several intensity measurements are taken. The portion of the object radiation which is not diffracted by the hologram but instead propagates straight through the hologram can be discarded. Better yet, the undiffracted light can be used as input to some other imaging system operating at the same time (see sections 5.2.2-5.2.3 for an example.) The intensity measurements are then processed to reconstruct the intensity distribution of the object. It has been shown [5] that the information

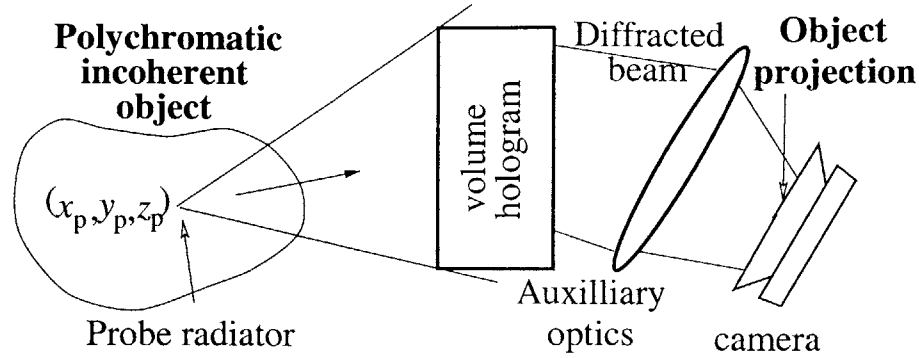


Figure 5-3: Schematic of a general-purpose volume-holographic imaging system.

recovered from the object can span all three spatial dimensions as well as the spectral dimension. Therefore, the hologram may be used to perform four-dimensional (4D) imaging. However, we limit the discussion to spatial imaging in 3D only.

The object→image mapping properties of the volume hologram are also explained by virtue of the matched filter behavior of volume holograms with respect to their input illumination, which is well known from the context of holographic storage and optical pattern recognition. In other words, a volume hologram, unlike thin diffractive elements, diffracts selectively; among all components of a complex illuminating beam, significant scattering is produced only by those that yield phase-matched diffraction along the entire length of the volume hologram. Thus, matched filtering of the field input to the hologram is achieved by virtue of the Bragg matching process. Bragg matching along the lateral spatial dimensions (*i.e.*, perpendicular to the optical axis) forms the basis of image correlators [111, 112] as well as angle and shift multiplexed [113, 87] holographic memories. Bragg matching in the spectral dimension forms the basis of wavelength multiplexing [113].

For comparing VHI with other systems, we formulate generic 3D imaging as a linear inverse problem and express imaging performance in terms of the information-theoretic metric of Imaging Mutual Information (IMI). The development and associated assumptions are given in section 5.2.1. Quantifying the imaging performance of volume holographic instruments presents a challenge because of the competition

between matched filtering (which increases resolution) and low diffraction efficiency (which decreases dynamic range and, hence, resolution.) We use the IMI metric to attack this problem. The numerical comparison with a simple lens-based microscope with the same numerical aperture are given in section 5.2.3.

5.2.1 Imaging Mutual Information of Incoherent Imaging Systems

For ease of comparison, we assume that the object is a primary source of light distributed within volume \mathcal{V}_s . We also assume that the object is spatially incoherent and monochromatic. Fluorescent objects match these properties quite well in practice.

Let $I(\mathbf{r})$ denote the intensity distribution of the object as function of the spatial coordinate \mathbf{r} in object space ($\mathbf{r} \in \mathcal{V}_s$.) After passing through an arbitrary linear optical system, the light intensity is transformed according to Hopkins' integral [1, pp. 577-578]

$$\tilde{I}(\mathbf{r}') = \int_{\mathcal{V}_s} h(\mathbf{r}, \mathbf{r}') I(\mathbf{r}) d^3\mathbf{r}, \quad (5.4)$$

where $h(\mathbf{r}, \mathbf{r}')$ is the incoherent impulse response of the system. The output intensity $\tilde{I}(\mathbf{r}')$ is observed in an appropriate detector space, typically restricted to lie on a plane.

In many optical systems, it is valid to assume that the object is also planar. This is true, for example, for a microscope observing a thin specimen, for projection systems, etc. With the additional assumption that the regions of interest are not affected by vignetting, the intensity response (5.4) may be modeled as shift-invariant, leading to

$$\tilde{I}_{2D}(\mathbf{r}') = \int_{\mathcal{V}_s} h(\mathbf{r} - \mathbf{r}') I_{2D}(\mathbf{r}) d^2\mathbf{r}, \quad (5.5)$$

which is, of course, a convolution. As mentioned in 1, in 3D optical systems the shift invariance assumption does not hold. For example, a confocal microscope relies *exactly* on vignetting to achieve depth slicing. Volume holograms are also shift-variant (refer sections 2.1.1 and 2.2.1). Therefore, we will subsequently assume that

the imaging transformation is given by the general form (5.4) rather than the more restrictive convolution formula (5.5).

Returning to (5.4), one immediately recognizes a Fredholm integral equation of the first kind, which is commonly encountered in inverse problems [100]. It is generally known that these problems are ill-posed because the kernel $h(\mathbf{r}, \mathbf{r}')$ de-localizes the spatial contents of the source at the detector space. Moreover, in the case of volumetric imaging there is a dimensional mismatch between the object and detector spaces (3D and 2D, respectively.) The obvious way around the mismatch is to discretize the problem and make sure that there are at least as many intensity measurements available as desired samples from the object intensity distribution.

We will make the additional assumption that the source is also discrete. This assumption is not necessary, but it simplifies the estimation of imaging quality that follows, without seriously compromising the qualitative nature of the conclusions. The truth of the last statement depends, of course, on the sampling scheme. We will here assume that this has been done correctly. A brief discussion of sampling and space-bandwidth product issues can be found at the end of this chapter.

To treat the discrete model, we form a vector $\underline{\mathbf{I}}$ of object intensities, and a vector $\tilde{\underline{\mathbf{I}}}$ of intensity measurements.¹ The intensity measurement vector should contain *all* the measurements pertinent to the imaging task at hand. For example, in the case of a confocal microscope, $\underline{\mathbf{I}}$ is formed by all the point-wise measurements. The superposition integral (5.4) then becomes a simple matrix equation

$$\tilde{\underline{\mathbf{I}}} = \underline{\mathbf{H}} \underline{\mathbf{I}}. \quad (5.6)$$

In this description, element $\underline{\mathbf{H}}_{jk}$ of system matrix $\underline{\mathbf{H}}$ quantifies the contribution of the k -th source $\underline{\mathbf{I}}_k$ to the j -th measurement $\tilde{\underline{\mathbf{I}}}_j$.

The resolution limitation of an imaging system is associated with the stability of its corresponding matrix $\underline{\mathbf{H}}$ to inversion. For example, consider the simple case of

¹Note that we use boldface for position vectors in Cartesian space, underscored symbols for vectors of intensity values, such as collections of object and image samples, and underscored boldface for matrices.

imaging two discrete point sources using a system matrix:

$$\underline{\mathbf{H}} = \begin{bmatrix} 1 & \epsilon \\ \epsilon & 1 \end{bmatrix}. \quad (5.7)$$

The ϵ term ($\epsilon < 1$) in eqn. 5.7 quantifies the ‘‘cross-talk’’ that each point source contributes to the measurement of its counterpart (In a typical optical imaging system, ϵ would increase to 1 as the distance between the two sources decreases). Suppose also that the measurement contains noise *i.e.*

$$\tilde{\underline{\mathbf{I}}} = \tilde{\underline{\mathbf{I}}}^{(O)} + \tilde{\underline{\mathbf{I}}}^{(N)}, \quad (5.8)$$

where $\tilde{\underline{\mathbf{I}}}^{(O)} = \underline{\mathbf{H}}\underline{\mathbf{I}}$ is the ideal image and $\tilde{\underline{\mathbf{I}}}^{(N)}$ is the perturbation due to noise. Inverting eqn. 5.7, we obtain the estimate of the object as:

$$\underline{\mathbf{I}}^{(\text{est})} = \underline{\mathbf{I}} + \underline{\mathbf{H}}^{-1} \tilde{\underline{\mathbf{I}}}^{(N)} = \underline{\mathbf{I}} + \frac{1}{1 - \epsilon^2} \begin{bmatrix} 1 & -\epsilon \\ -\epsilon & 1 \end{bmatrix} \tilde{\underline{\mathbf{I}}}^{(N)}. \quad (5.9)$$

From eqn 5.9, it is seen that the error due to the noise is amplified by $\epsilon/(1 - \epsilon^2)$ times the relative value of the noise itself. The amplification factor can grow quite large as $\epsilon \rightarrow 1$. Thus, we see that if the two object sources are too close together (whence $\epsilon \rightarrow 1$), the imaging inversion operation becomes unstable with respect to the noise-induced perturbation in the data. This kind of instability is characteristic of ill-posed problems. (Note that if actually $\epsilon = 1$, then the matrix becomes singular; *i.e.* no image can then be formed.)

The resolution properties of the imaging system described by (5.6) are expressed sufficiently in terms of the stability of the system matrix. Several metrics exist in the literature for measuring the inversion stability of a matrix such as the eigenvalue spectrum [114], Fisher information [115] and the Hotelling trace [116]. We have chosen to measure inversion stability by use of Shannon’s mutual information metric in this section. The justification for this choice is that typically the inversion operation does not end with the measurement $\tilde{\underline{\mathbf{I}}}$. The quality of the image can be much improved

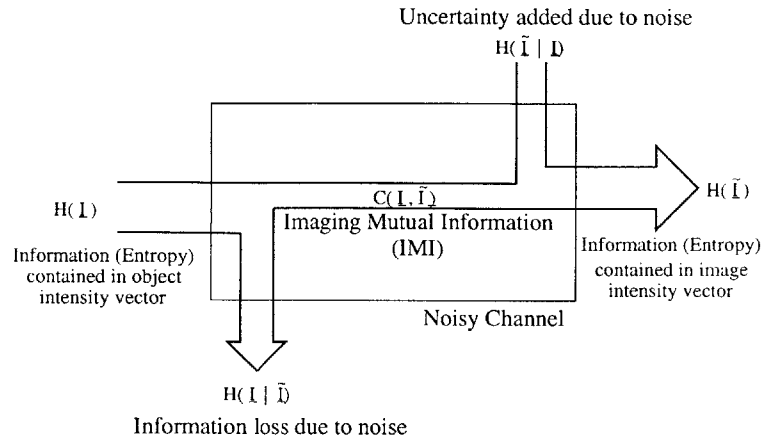


Figure 5-4: The IMI measures the actual amount of information that is obtained after transmission through a noisy channel. The IMI is a measure of the relevant information from a measurement since it disregards contributions from channel noise.

by nonlinear regularization methods or various forms of statistical processing and use of prior information about the object. All these methods essentially attempt to separate the noise content of the measurements from the contributions due to the object itself. Shannon’s theory provides good estimates of the upper bound on post-processed image quality that the system can achieve.

Mutual information may be understood from the illustration of Fig. 5-4. $H(\mathbf{I})$ is the differential entropy² of the object to the imaged. In other words, $H(\mathbf{I})$ nats of information are needed to answer the question “What is the intensity of the object

²Entropy is a measure of the uncertainty associated with a random variable. Uncertainty also measures the information content of the answer to a question. This can be understood by comparing the two following questions:

- (a) “Did you win the lottery yesterday?”
- (b) “Did the coin toss result in a head?”

Both receive a “yes/no” answer; however, answering the first question with a “no” is fairly certain to be correct. Whereas, the answer to the second question is completely uncertain for a fair coin. Information theory shows that the coin question has higher entropy than the lottery question. Information is measured differently for discrete and continuous random variables. For discrete random variables, (the coin toss for example) the information is measured in bits. The answer to the coin toss question is worth exactly one bit for a fair coin. The answer to the lottery question for the state of Massachusetts is worth approximately 2×10^{-5} bits. The information of continuous random variables (for example, light intensity at high photon counts) is measured by the differential entropy in nats ($1 \text{ nat} = \log_2 e$ bits). For example, if the light intensity is a Gaussian with a mean of $1W$ and a variance $0.25W$, the information content of the light intensity distribution is 0.0326 nats.

as a function of the spatial coordinates?" for the problem at hand. Light emitted by the object propagates and reaches the detector and forms an image. The differential entropy of the image is $H(\tilde{\mathbf{I}})$. In the absence of noise, $H(\tilde{\mathbf{I}}) = H(\mathbf{I})$. So in the absence of noise, the object and the image contain exactly the same amount of information. Hence, the imaging operation is perfect. The image is a deterministic function of the object and the object can be inferred from the image without any uncertainty.

However, the presence of noise in the channel introduces some uncertainty in the system's ability to infer the object given complete image information. This uncertainty is quantified by the conditional entropy $H(\mathbf{I} | \tilde{\mathbf{I}})$. In other words, the amount of useful information propagating in the imaging channel is the information contained in the object minus the uncertainty induced by the channel noise. This is illustrated in the left-hand part of Fig. 5-4 and is expressed as:

$$C(\mathbf{I}, \tilde{\mathbf{I}}) = H(\mathbf{I}) - H(\mathbf{I} | \tilde{\mathbf{I}}), \quad (5.10)$$

Alternatively, one may regard the image information and regard it as the sum of the useful object information that the channel carries and some entropy added by the channel noise. This entropy quantifies the conditional uncertainty of the image given the object $H(\tilde{\mathbf{I}} | \mathbf{I})$. In this case, the useful information carried by the channel is quantified by the information content of the image minus the uncertainty added by noise as:

$$C(\mathbf{I}, \tilde{\mathbf{I}}) = H(\tilde{\mathbf{I}}) - H(\tilde{\mathbf{I}} | \mathbf{I}), \quad (5.11)$$

(This is illustrated by the right-hand part of Fig. 5-4.)

In eqns. 5.10 and 5.11, $C(\mathbf{I}, \tilde{\mathbf{I}})$ is the *same* quantity and is known as the mutual information of the channel. It is a measure of the information that is common between the input to and output of the channel. Hence, if the mutual information is maximized, the channel performs optimally under the constraints imposed by channel noise. In the context of imaging, $C(\mathbf{I}, \tilde{\mathbf{I}})$ is referred to as the Imaging Mutual Information (IMI). More rigorously, mutual information is defined as the Kullback-Leibler distance between the joint probability density function (pdf) of object and image

vectors and the product of the corresponding marginals [117, pp. 18-21]. Intuitively, equality between the joint pdf and the products of the marginal pdfs means that object and image are mutually independent. Therefore, one wants the distance between the two pdfs to be as large as possible.

Precise calculation of the IMI requires knowledge of the object statistics as well as the joint statistics of the object and image. Unfortunately, three-dimensional object models in the literature provide up to second-order correlations, whereas calculation of the probability density function requires all orders. Moreover, the problem of determining joint statistics between object and image from the statistics of the object and the statistics of the noise is intractable for realistic noise models (e.g., Poisson.) To develop a simple, tractable model we make the following assumptions:

- the object intensity is Gaussian-distributed around a mean intensity \tilde{I}_0 with variance σ_{obj}^2 , and we may neglect the negative tail of the object distribution;
- the individual sources composing the discretized object are mutually independent (this is a stronger assumption than mutual incoherence;)
- the noise is uncorrelated with the measurement, and it is additive Gaussian white noise with mean zero and variance σ^2 (this model is good for electronic noise added by the detector circuitry, but models Poisson noise very poorly.)

With these assumptions, and for a square system matrix \mathbf{H} , the IMI can be calculated explicitly with help from a result by [117, pp. 230-231] and yields the result

$$C(\mathbf{I}, \tilde{\mathbf{I}}) = \sum_{n=1}^N \log \left(1 + \frac{\tilde{I}_0 \mu_n^2}{\sigma^2} \right), \quad (5.12)$$

where μ_n are the eigenvalues of the $N \times N$ matrix \mathbf{H} . The result remains true for rectangular matrices (*i.e.*, over- or under-determined systems) except then the singular values must be used instead of the eigenvalues. The proofs are straightforward and will not be given here.

Intuitively, eqn. 5.12 is saying that the effective rank or number of degrees of freedom of the system (*i.e.*, how many measurements contribute useful information

towards determining the object) is limited by the noise present in the system relative to the power emitted by the objects. In an imaging system with ideal matrix $\underline{\mathbf{H}}$ (such as the identity matrix for objects with our assumed statistics,) all measurements contribute equal amounts of information about the object (because all eigenvalues are equal.) Generally, off-axis matrix elements bias the eigenvalue spectrum towards lower values, which in turn decreases the IMI.

The question then, becomes: How can one design an imaging system such that the IMI is maximized under general conditions about object and noise statistics? This problem presents interesting challenges, both theoretical and practical. From the theoretical point of view, there are difficulties associated with the statistical calculations as pointed out earlier. Assuming that this problem is solved, the next issue is to implement optical elements in practice such that the desired $\underline{\mathbf{H}}$ is achieved.

5.2.2 Mutual Image Information for fluorescent objects elongated in the direction of the optical axis

Consider an object modelled as N mutually incoherent point sources aligned along the optical axis, as shown in Figure 5-5(a). These sources may be thought of as fluorescent beads under illumination by an appropriate pump beam. The source locations and intensities are z_k and I_k ($k = 1, \dots, N$), respectively. The distance between two successive samples is a constant Δz . In this section, we will compare three alternative imaging systems that can be used to image the sources (*i.e.*, determine the values of I_k .)

The first, pinhole-based imaging system is described in Figure 5-5(b). A combination of objective-collector lenses in tandem is used to take N measurements \tilde{I}_j ($j = 1, \dots, N$) as follows: at the j -th measurement, the objective focuses the pump illumination onto the $k = j$ -th source and simultaneously the same source is at the front focal plane of the collector lens. Note that the illumination along the object is essentially collimated; therefore, this system is, strictly speaking, non-confocal on the illumination side. The measurement itself corresponds to the integrated intensity

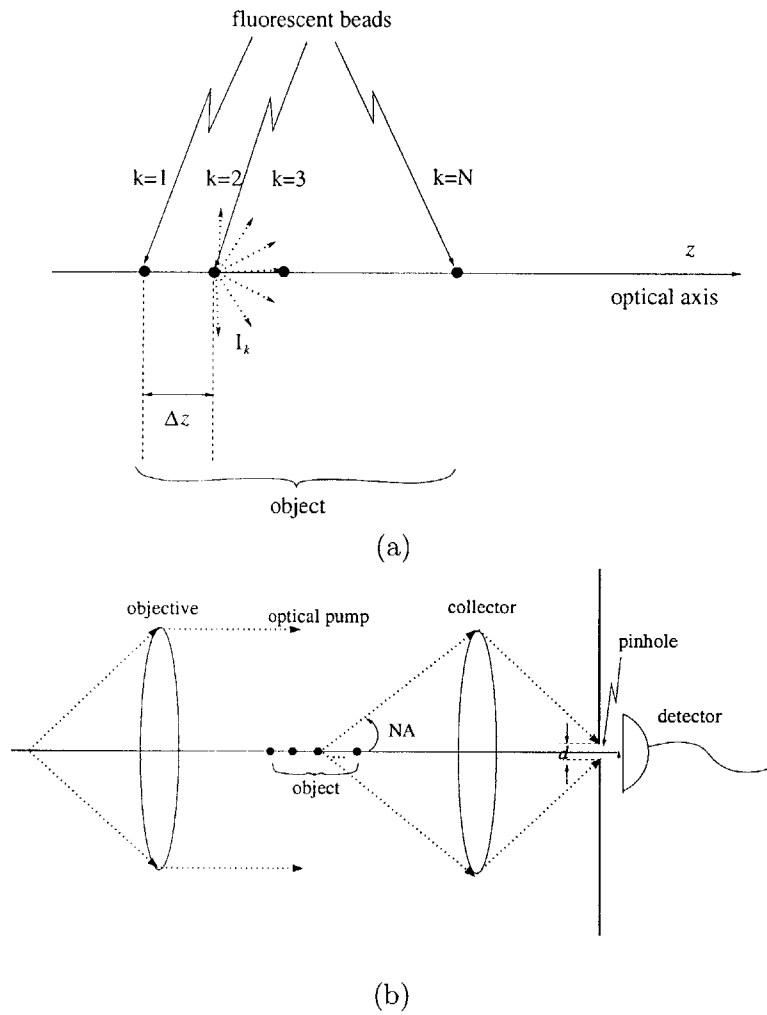


Figure 5-5: (a) Source geometry for the simulations of section 5.2.2. (b) Fluorescence imaging geometry with a lens and a pinhole for depth resolution. (c) Geometry of fluorescence imaging with a volume holographic element. (d) Imaging with a volume holographic element exploiting in parallel the undiffracted beam with the pinhole-based system.

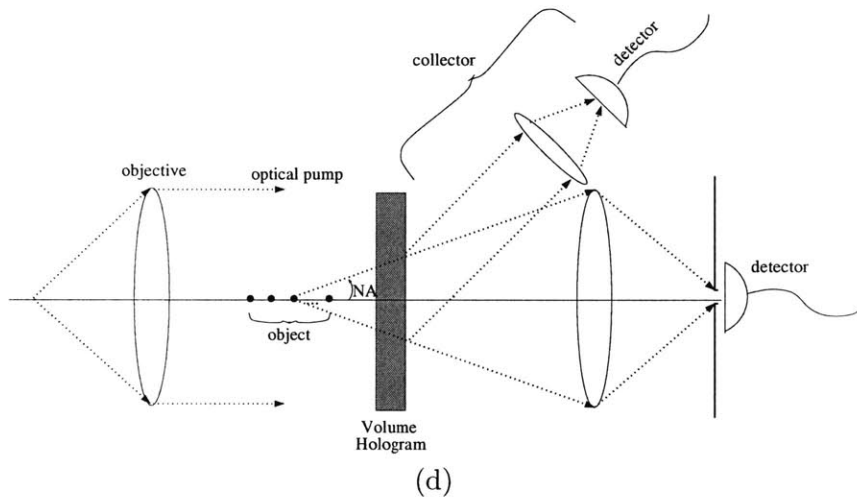
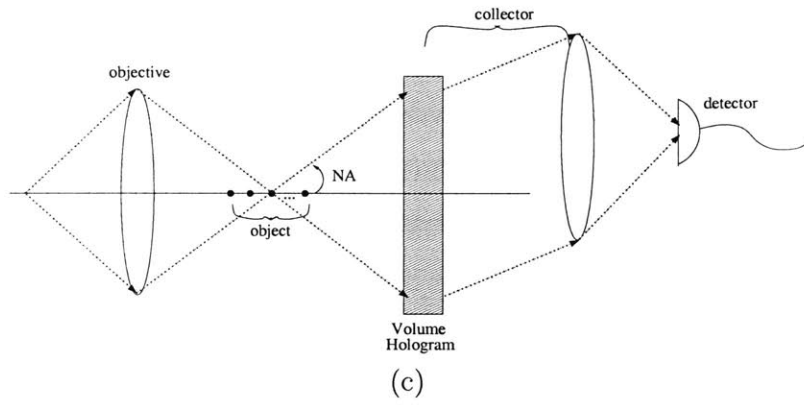


Figure 5-5: (continued)

captured by a detector placed behind a pinhole of diameter d . The numerical aperture of the imaging systems is taken to be (NA) and, for notational simplicity, we assume that the magnification equals 1 on both sides.

The second system, described in Figure 5-5(c), is similar except the collector lens has been replaced by a composite collector element made of a volume hologram and a Fourier lens in tandem, and there is no pinhole. (In practice, of course, care has to be taken that light going straight through the hologram does not reach the detector.) The radii of the hologram and the Fourier lens are taken such that the numerical aperture NA is the same as that of Figure 5-5(b).

The third system, described in Figure 5-5(d), is, in a sense, a combination of the previous two. The collector lens and pinhole placed after the volume hologram utilize the light that passes straight through the hologram without being diffracted, as described by the pin-hole based imaging system. Thus, one obtains redundant information about the object from both the hologram and collector lens and no power is wasted on the collector optics side.

In the next three sections we briefly describe how the corresponding system matrices $\underline{\mathbf{H}}^{(\text{cf})}$, $\underline{\mathbf{H}}^{(\text{vh})}$ are obtained, and then compare the two systems numerically in terms of IMI, according to the theory of section 5.2.1.

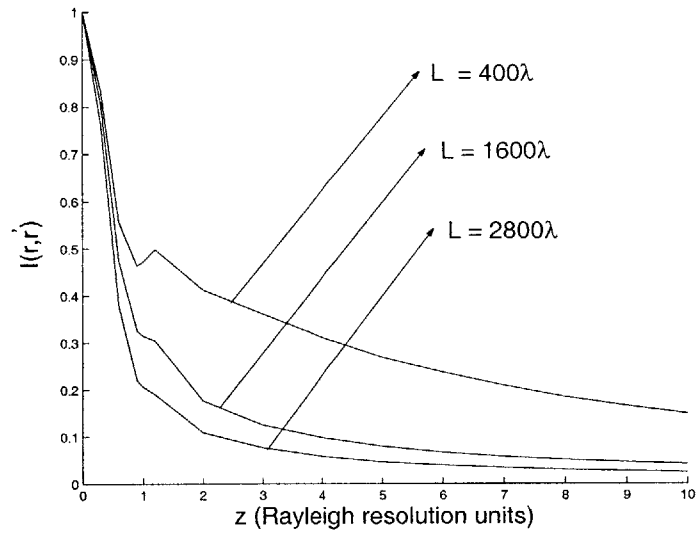
Pinhole-based microscope model

The intensity contributed by the k -th source to the j -th measurement depends on the relative location of that source to the common focal plane of the collector. Large displacement relative to the collector reduces the amount of fluorescence that the pinhole allows to reach the detector.

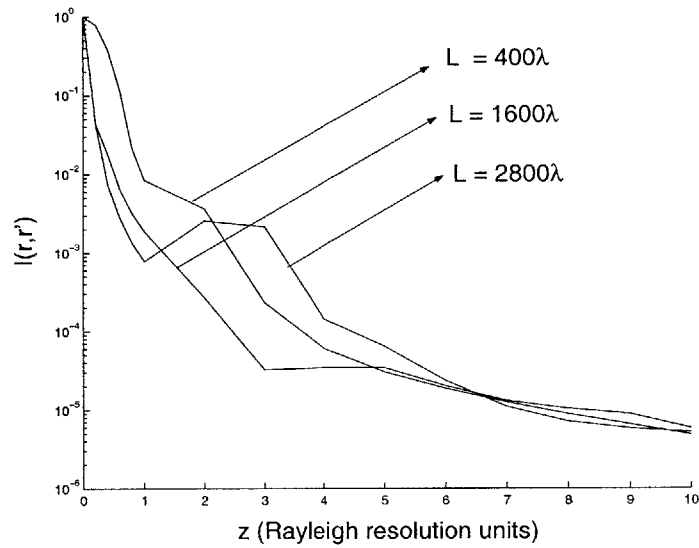
To simplify the notation later, we define the normalized pinhole diameter

$$v_d = \frac{2\pi(\text{NA}) d}{\lambda}. \quad (5.13)$$

Using this definition, the amount of fluorescent power received by the detector per



(a)



(b)

Figure 5-6: Integrated intensity (over infinite detector area) for the volume holographic imaging system of Fig. 5-5(c). The hologram has $u = 0.4$, $R = 1,500\lambda$ and (a) $\mathbf{r}_f = (0, 0, -10^4\lambda)$, (on-axis hologram) (b) $\mathbf{r}_f = (4 \times 10^3\lambda, 0, -10^4\lambda)$ (off-axis hologram). Results for three different thicknesses are shown.

unit of fluorescence emitted by the bead is given by

$$\underline{\mathbf{H}}_{jk}^{(lp)} = \int_0^{v_d} |\mathcal{L}(u, v)|^2 v dv. \quad (5.14)$$

This integral is computed in terms of a series expansion, which significantly accelerates the numerical calculations.

Note that the matrix $\underline{\mathbf{H}}^{(lp)}$ is Toeplitz. Therefore, its eigenvalues can be computed more efficiently by a Fourier transformation for large objects.

Volume hologram model

Equation (2.7) gives the amplitude of the diffracted field as a function of the detector co-ordinates. The intensity contributed by the probe source to the detector plane is

$$\tilde{I}_k(\mathbf{r}') = \left| \tilde{\mathbf{E}}_d(\mathbf{r}') \right|^2. \quad (5.15)$$

The total intensity is the sum of all the contributing point sources, *i.e.*

$$\tilde{I}(\mathbf{r}') = \sum_{k=1}^N \tilde{I}_k(\mathbf{r}'). \quad (5.16)$$

Each element of the system matrix of the volume holographic system is given by the surface integral of the volume-diffracted intensity (5.15) over the *entire* detector area (since there is no pinhole.) To emphasize the lack of a pinhole, we write the expression for the power measured by the detector as

$$\underline{\mathbf{H}}_{jk}^{(vh)} = \sqrt{\eta} \iint_{-\infty}^{+\infty} \left| \int_{-L/2}^{L/2} \exp \{i\pi C(z)\} \mathcal{L}(2\pi A(z)R^2, 2\pi B(z)R) dz \right|^2 dx' dy'. \quad (5.17)$$

Lacking a series expansion equivalent to the series expansion for (5.17) equivalent to, we compute these terms by numerical integration. Also note that the system matrix for the volume hologram is only *approximately* Toeplitz. Some numerical examples are shown in Figure 5-6.

Combined model

The dual imaging system of Figure 5-5(d) acquires information through both the volume hologram and a lens+pinhole system. To model the IMI we concatenate the observation vectors and system matrices of the individual systems as follows:

$$\begin{pmatrix} \bar{\mathbf{I}}^{(\text{lp})} \\ \dots \\ \bar{\mathbf{I}}^{(\text{vh})} \end{pmatrix} = \begin{pmatrix} \sqrt{1-\eta} \mathbf{H}^{(\text{lp})} \\ \dots \\ \mathbf{H}^{(\text{vh})} \end{pmatrix} \begin{pmatrix} \mathbf{I} \end{pmatrix}. \quad (5.18)$$

Matrices $\mathbf{H}^{(\text{lp})}$, $\mathbf{H}^{(\text{vh})}$ are given by (5.14), (5.17), respectively. The IMI is computed according to (5.12), where the μ_n 's are the singular values of the concatenated matrix as mentioned in section 5.2.1. As we show in the next section, the over-determined system (5.18) may be richer or poorer in information return compared to the individual imaging systems composing it, depending on the value of η . We elaborate this point in section 5.2.3 below.

5.2.3 Numerical comparison

We simulated the imaging performance of the pinhole-based system, the volume-holographic system and their combination by computing the IMI for an object as shown in Figure 5-5(a) with $N = 11$, $\Delta z = 1$ Rayleigh unit $= 2\lambda/(\text{NA})^2$ and $(\text{NA})=0.15$. To facilitate the interpretation of the results, we need to point out the fundamental sources of information loss in the two individual optical systems. In the pinhole-based system, information is lost because of the mismatch between the shape of the point-spread function of the lens and the abrupt discontinuity introduced by the pinhole. When the pinhole diameter d is very small, the information loss evidences itself as loss of optical power, which drives down the IMI. On the other hand, if the pinhole is opened up too much it begins to approach a wide-field system with no depth resolution capability whatsoever. Therefore, the IMI as function of d peaks at an optimum diameter, as seen in the plots of Figures 5-7, 5-8. Notice that the optimum IMI occurs at a diameter slightly smaller than the lateral Rayleigh

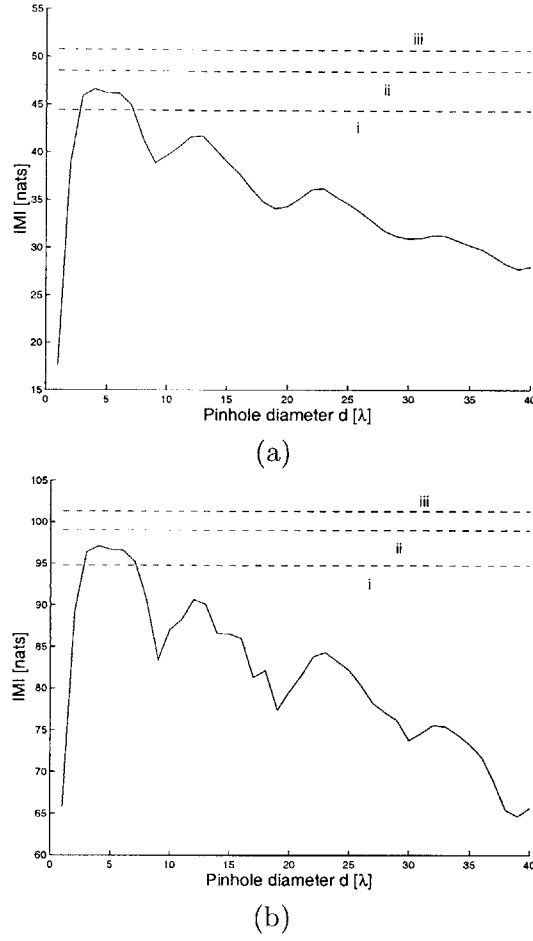
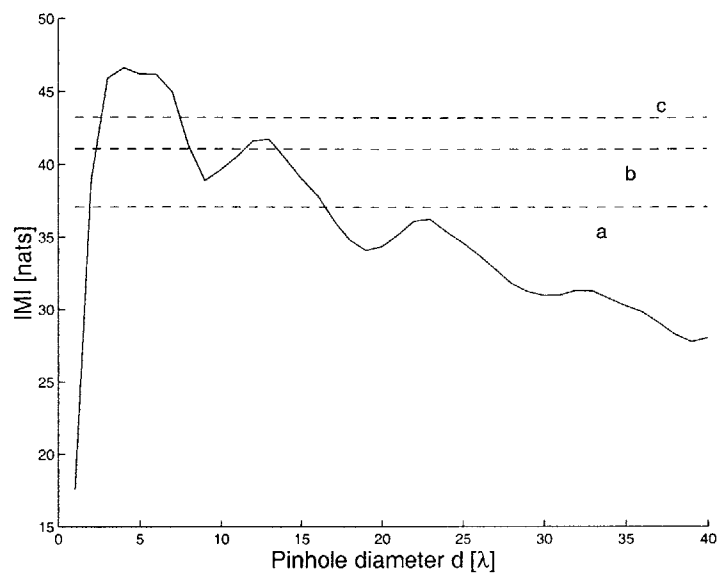
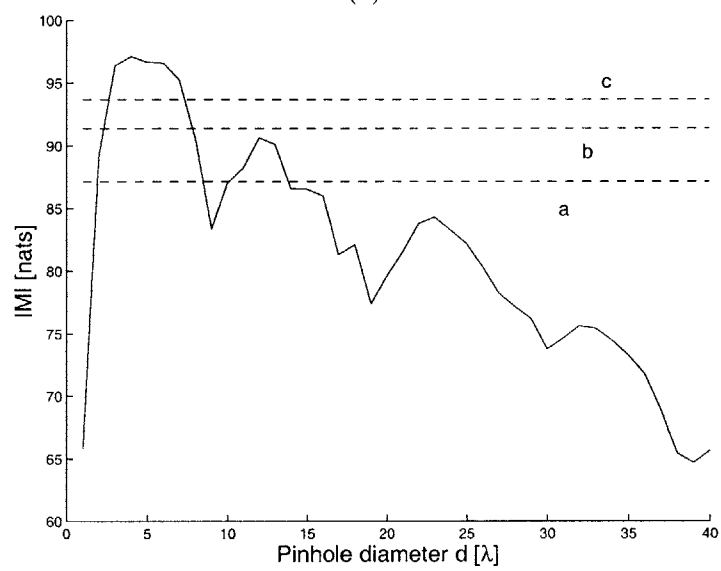


Figure 5-7: Comparison of IMI for the imaging system using a lens plus pinhole of varying diameter (Fig. 5-5b) with that of a volume hologram (Fig. 5-5c). The solid line is the IMI of the confocal and the dashed lines are IMI of various volume holograms. Here the holograms are assumed to be ideal, *i.e.* with diffraction efficiency $\eta = 1$. The hologram data are labelled such that (i) is an $L = 400\lambda$ -thick hologram recorded with an on-axis reference $\mathbf{r}_f = (0, 0, -10^4\lambda)$, plane-wave signal with $u = 0.4$; (ii) is an $L = 1,600\lambda$ -thick hologram recorded with an on-axis reference $\mathbf{r}_f = (0, 0, -10^4\lambda)$, plane-wave signal with $u = 0.4$; and (iii) is an $L = 400\lambda$ -thick hologram recorded with an off-axis reference $\mathbf{r}_f = (4 \times 10^3\lambda, 0, -10^4\lambda)$, plane-wave signal with $u = 0.4$. Increasing L to $1,600\lambda$ in the off-axis geometry leads only to marginal increase in IMI.



(a)



(b)

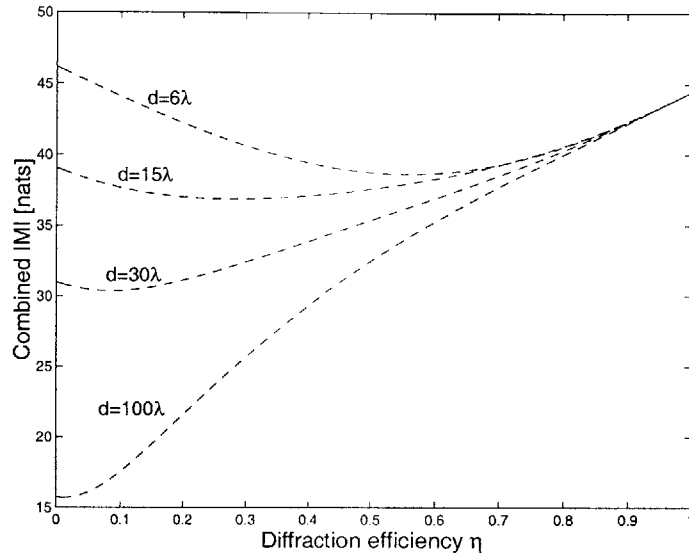
Figure 5-8: Data and layout same as in Figure 5-7, except for a weaker hologram with $\eta = 0.5$.

resolution limit, which in this case is $1.21\lambda/(\text{NA}) = 8.1\lambda$.

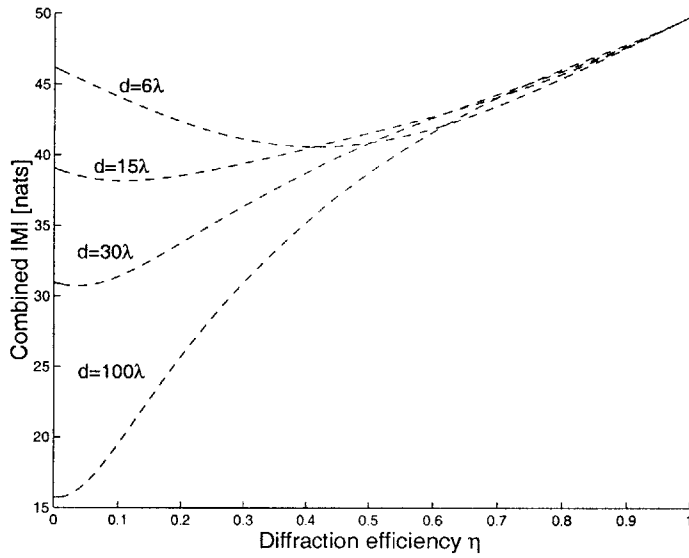
On the other hand, the volume hologram is, by construction, a matched filter. However, the hologram still loses information because it only diffracts fraction η of the incident power. The implication is clear by comparing the data of Figure 5-7, where the hologram was assumed to have $\eta = 1$ and Figure 5-8, where the hologram had the more realistic (but still overly optimistic) value $\eta = 0.5$. We can see that an ideal hologram ($\eta = 1$) of reasonable thickness (more than 1000λ , approximately) outperforms the IMI of the pinhole-based system. This superiority is lost when the diffraction efficiency is limited.

The trade-off between matched filtering and diffraction efficiency from the point of view of the hologram, and pinhole diameter from the point of view of the lens is further elucidated by considering the combined system of Figure 5-5(d). The IMI of the combined system as function of η for various pinhole diameters and holographic geometries is plotted in Figure 5-9. When the pinhole-based system is operating at optimum diameter ($d \approx 6\lambda$), the use of the hologram in parallel makes sense at very high diffraction efficiencies only. This is evidenced by the dip in the IMI curves at intermediate η 's and is due to the inefficient use of optical power at these regimes. On the other hand, when the pinhole is operated at high diameters (e.g. because of geometrical aberrations in the system) the matched-filter operation of the hologram consistently improves imaging performance, even at low diffraction efficiencies. Note also that increasing the hologram thickness generally improves the IMI, as evinced in the curves of Figures 5-7 through 5-8.

We have shown previously in chapter 4 that volume holograms can be useful in numerous imaging contexts, e.g. spectral imaging and imaging through strongly aberrating media [118]. Compared to other applications of volume holography (e.g., optical memories), in imaging it is easier to design and “program” the hologram. Optimizing the IMI metric (equivalently, optimizing the eigenvalue spectrum of the system's H-matrix) can serve as a useful design guideline and comparison metric against competing techniques. Finally, a volume hologram is the most appropriate digital post-processing [5]. These systems can realize the full range of information

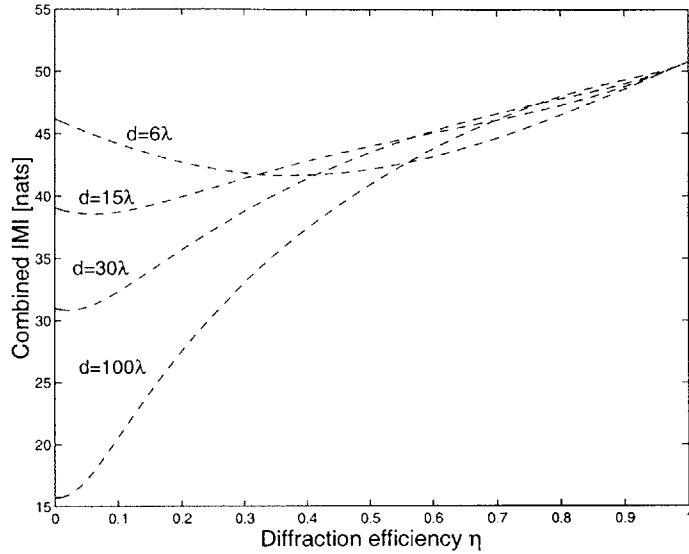


(a)



(b)

Figure 5-9: IMI for the combined imaging system of Fig. 5-5(d). The volume holographic geometries considered are (a) on-axis $\mathbf{r}_f = (0, 0, -10^4\lambda)$ with $L = 400\lambda$; (b) on-axis $\mathbf{r}_f = (0, 0, -10^4\lambda)$ with $L = 2,800\lambda$; (c) off-axis $\mathbf{r}_f = (4 \times 10^3\lambda, 0, -10^4\lambda)$ with $L = 2,800\lambda$.



(c)

Figure 5-9: (continued)

extraction predicted by the IMI metric.

The simulations of section 5.2.3 are intended as demonstrations of the potential of volume holograms for imaging. Despite numerous approximations (ignoring lateral object structure; sampling implemented as isolated, mutually incoherent point sources; Gaussian noise statistics, etc.), the IMI model provides a very convenient tool for understanding trade-offs between light efficiency and resolution. This is particularly appropriate for volume-holographic imaging instruments, where the advantage of matched filtering is offset by the limited diffraction efficiency. We will discuss an optical method to resolve the problem of limited diffraction efficiency next in chapter 6

Chapter 6

Resonant Volume Holography

Thus far, we have described the use of either spherical or plane wave reference beams for VHI. However, both these systems suffer the same disadvantage *i.e.* they are photon limited. Only the diffracted light is used for VHI; the undiffracted light is wasted. The photorefractive crystal LiNbO_3 diffracts only about 10% of the light and so, a significant amount of information is lost in the undiffracted light. We have also shown previously in chapter 5 that this loss of photons results in poorer imaging performance for the VHI system. In this chapter, we discuss an optical method to enhance the diffraction efficiency of weak holograms.

The new method is based on using the hologram inside a resonant optical cavity. We have shown experimentally and theoretically that efficiencies approaching 70–80% can be achieved from weak holograms (3 – 10%) using this method.

6.1 Introduction to Resonant Holography

We have seen that volume holographic optical elements have been used in optical inter-connects [48], data storage [69, 68] and imaging [5]. For most applications, the hologram should diffract the highest amount of incident light possible; the undiffracted light is wasted. We show that diffraction efficiencies approaching 100% are obtained by placing the hologram inside an optical cavity and demonstrate the idea experimentally in the context of two applications: an angle multiplexed holographic

memory with increased dynamic range and an optical three-port element.

Re-entrant diffraction into ring resonators has been used in the past for image storage and associative recall [119, 120] and into Fabry-Perot type optical cavities for optical interconnects [121, 122]. Instead, we tune the cavity to resonate the diffracted beam by multiple passes of the readout beam through the hologram.

Resonant holograms are recorded conventionally by interfering mutually coherent reference and object beams inside a photo-sensitive medium [50]. After recording is complete, the hologram is placed inside an optical cavity and probed with a beam which replicates as closely as possible the reference beam used during the recording phase. For brevity, we limit the discussion to the Bragg diffraction regime. However, our results may also be extended to the Raman-Nath [8] regime by taking multiple diffracted orders into account.

In the resonator of Figure 6-1(a) [123] with normal incidence of the readout beam, both the forward and backward propagating on-axis probe beams are Bragg-matched. Therefore, a forward reconstruction and a phase-conjugate reconstruction are obtained simultaneously. Resonance is obtained when all diffracted beams interfere constructively. Optical losses (absorption, scatter) place an upper limit on the resonant diffraction efficiency. The finesse of the holographic cavity is defined by the losses in combination with the single-pass efficiency of the hologram.

Let r denote the amplitude reflection coefficient of the partially reflecting mirror, and η_1 the single-pass diffraction efficiency of the hologram (which is obtained from the stand-alone hologram, without the optical cavity). Also, let λ denote the wavelength, b the one-pass intensity loss coefficient inside the cavity, and L the optical path-length of the cavity. In terms of these parameters, the forward and phase-conjugate diffraction efficiencies obtained from the hologram inside the cavity are, respectively,

$$\eta_{\text{fw}} = \frac{\eta_1 (1 - r^2)}{1 + r^2 (1 - \eta_1 - b)^2 + 2r (1 - \eta_1 - b) \cos(4\pi L/\lambda)}, \quad (6.1)$$

$$\eta_{\text{pc}} = \eta_{\text{fw}} (1 - \eta_1 - b). \quad (6.2)$$

By requiring that no optical power be reflected backwards in the direction of the

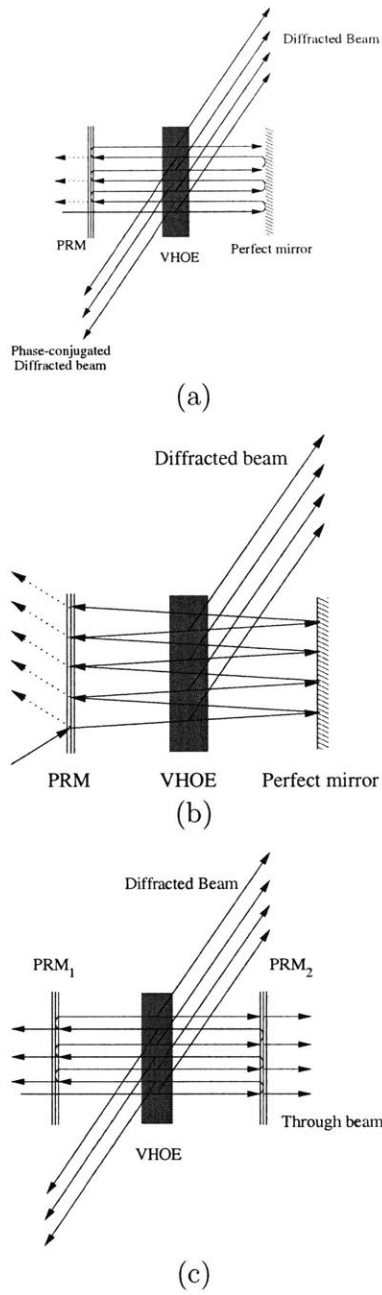


Figure 6-1: Geometries for resonant holography: (a) two-port with normal incidence; (b) two-port with oblique incidence; (c) three-port with normal incidence. VHOE: volume holographic optical element; PRM: partially reflecting mirror.

source, we obtain the resonance conditions

$$r = 1 - \eta_1 - b \quad (6.3)$$

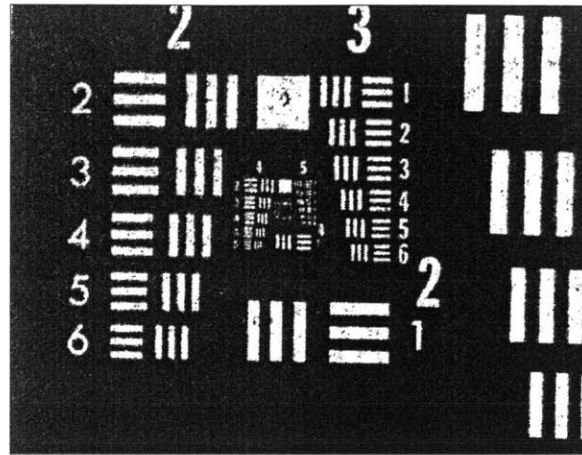
$$\text{and} \quad L = (2m + 1) \frac{\lambda}{4}, \quad (6.4)$$

where m is an arbitrary integer. The quality factor of the holographic resonator is, approximately, $Q = 1/\sqrt{b + \eta_1}$. Therefore, the coherence length of the incident beam should be larger than QL to ensure that (6.4) can be observed. When these conditions are satisfied, the resulting overall (forward plus phase conjugate) resonant diffraction efficiency is

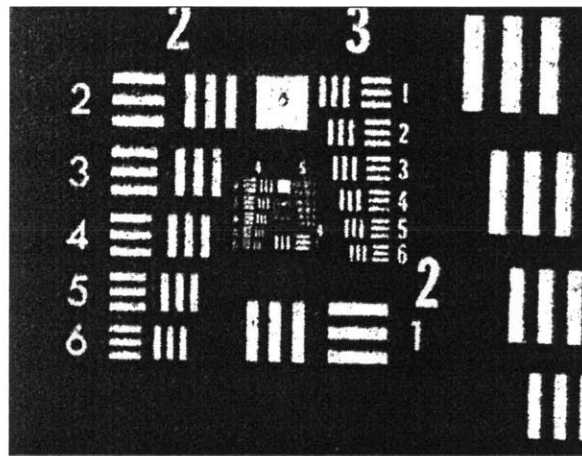
$$\eta_\infty = \frac{\eta_1}{\eta_1 + b}. \quad (6.5)$$

Since $\eta_1 + b < 1$, the resonant gain $G = \eta_\infty/\eta_1$ is always larger than 1. However, the single-pass loss coefficient b sets an upper limit to the attainable resonant gain. Resonance is most efficient when $\eta_1 \gg b$. Alternatively, losses may be compensated by including optical gain inside the holographic cavity.

The resonance conditions (6.3-6.4) apply to arbitrary diffracted wave-fronts. Spatial frequency components having equal diffraction efficiencies resonate simultaneously if they satisfy (6.3). This is verified in the experiment of Figure 6-2. On the other hand, spatial frequency components whose diffraction efficiencies deviate from (6.3) get filtered out because they are non-resonant. The sensitivity of the holographic resonator to detuning from resonance condition (6.3) is shown in Figure 6-3. These curves indicate that reconstructions degrade gracefully due to recording non-uniformities. On the other hand, resonance is extremely sensitive to the path-length condition (6.4) as in any Fabry-Perot type cavity [124]. As in other resonant configurations, the path sensitivity of resonant holograms has potential applications to interferometric sensing [125, 126] and wavelength routing [127].



(a)



(b)

Figure 6-2: Holographic reconstruction (a) non-resonant and (b) resonant. The hologram of the Air Force Resolution Chart was recorded slightly off the Fourier plane to ensure equal diffraction efficiencies for a wide bandwidth of plane wave components. The resonant and non-resonant reconstructions have comparable quality. This and subsequent experiments were implemented on a 1mm thick slab of Fe-doped LiNbO_3 with loss coefficient $b \approx 0.05$.

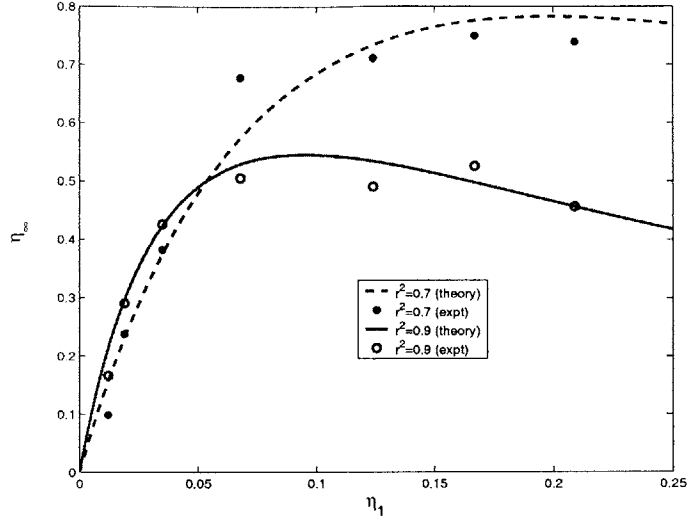


Figure 6-3: Theoretical (solid lines) and experimental sensitivity curves for deviation of the one-pass efficiency η_1 from its resonant value (6.3) for two cases of PRM reflectivity. Loss coefficient of $b = 0.05$ was used for the theoretical curves. The experimental curves were obtained with a lateral aperture of $\approx 1\text{mm}^2$, where resonance was relatively uniform.

6.2 Resonant Holographic Systems

We implemented a simple resonant holographic memory by mounting the holographic material of Figure 6-1(a) on a rotation stage. We superimposed plane wave holograms at several angular positions, separated by twice the Bragg selectivity of the material. Figure 6-4 shows resonant diffraction efficiency enhancement obtained by Bragg matching and resonating each hologram individually. The $(M/\#)$ [128] for the resonant holographic memory is related to the $(M/\#)$ for the stand alone (non-resonant) holographic memory by

$$(M/\#)_\infty \simeq \frac{(M/\#)_1}{\sqrt{b}}. \quad (6.6)$$

As expected, the losses in the optical cavity set an upper limit on the maximum achievable $(M/\#)_\infty$. For the resonant volume holographic memory of Figure 6-4, the increase in the $(M/\#)$ was ≈ 3.4 . We note that the obtained resonant gain of the $(M/\#)$ is less than the maximum possible gain *i.e.* ≈ 4.5 . This is on account of the fact that the PRM of the resonant setup ($r^2 = 0.9$) was not optimized according to

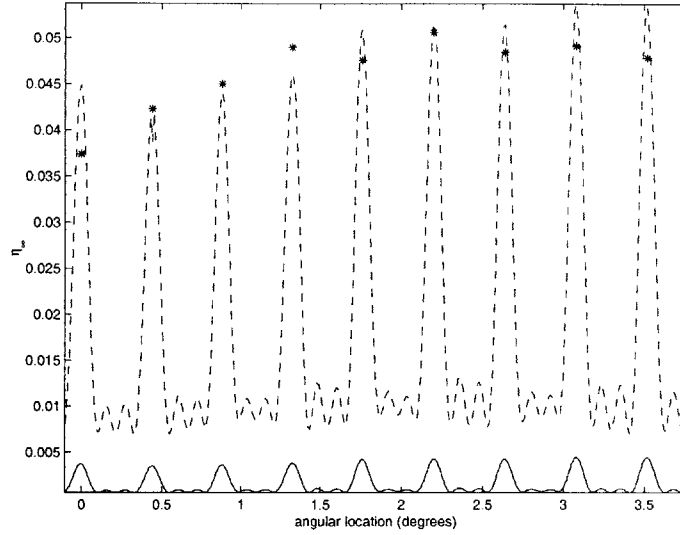


Figure 6-4: Holographic memory with resonant enhancement of the diffraction efficiency. The blue curve was obtained by angular scanning the memory without the resonator. Each peak corresponds to one stored hologram. The red curve was obtained by applying (6.1-6.2) and (6.4) to the experimental data of the blue curve. The black stars are actual values of the corresponding resonant diffraction efficiencies obtained experimentally.

(6.3).

Two methods can be used to eliminate the phase conjugate reconstruction: oblique incidence of the readout beam to the Fabry-Perot cavity, and use of a ring resonator.¹ The former presents problems in practice because the resonant beam walks off the resonator in the lateral direction.

The geometry of Figure 6-1(b) is similar to Figure 6-1(a) except the back mirror has been replaced by a partially reflecting mirror with amplitude reflection coefficient r' . Thus, this device acts as an optical three-port element. The amplitude resonance condition is

$$r = r'(1 - \eta_1 - b), \quad (6.7)$$

¹The suggestion of using a ring resonator to eliminate the phase conjugate reconstruction was made to us by Professor D. A. B. Miller.

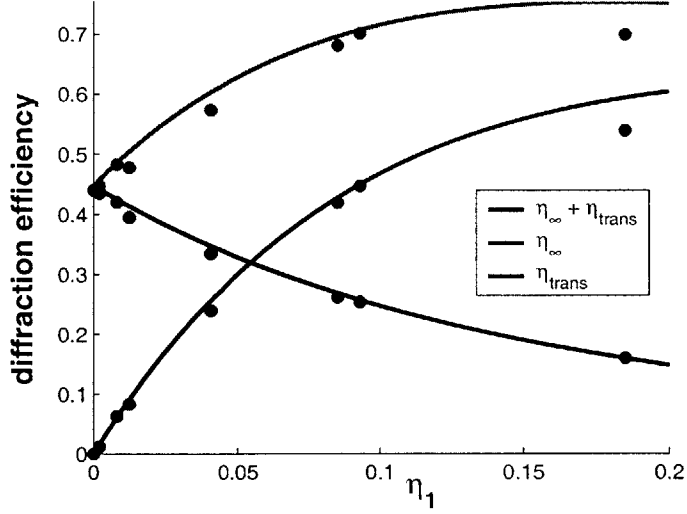


Figure 6-5: Experimental and theoretical response of the three-port element of Figure 6-1(c) with $r^2 = 0.7$, $r'^2 = 0.9$ and $b = 0.05$.

and the overall (forward plus phase conjugate) resonant diffraction efficiency is

$$\eta_{\infty} = \frac{\eta_1(1 + rr')}{1 - r^2}. \quad (6.8)$$

The fraction of the power transmitted straight through the hologram and the two partially-reflecting mirrors is

$$\eta_{\text{trans}} = \frac{r(1 - r'^2)}{r'(1 - r^2)}. \quad (6.9)$$

The sensitivity of this element to deviation of η_1 from the resonance condition (6.7) is shown in Figure 6-5. One can think of the resonant three-port element as an efficient “smart beam-splitter,” defining both the amplitude and phase of the deflected beam relative to the readout beam. Such a device could have interesting applications in fields such as quantum information processing.

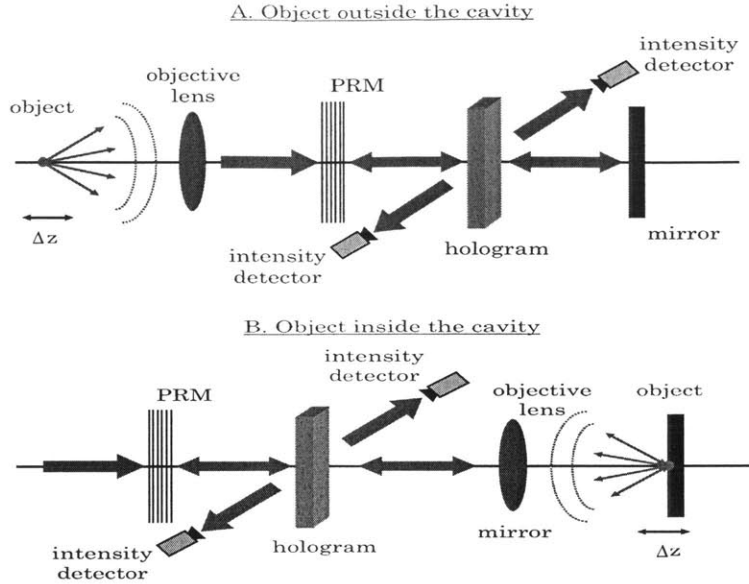


Figure 6-6: Imaging architectures for resonant imaging. (a) point source outside resonant cavity. (b) collimated point source inside resonant cavity.

6.3 Resonant holographic imaging architectures

In this section, we shall describe applying resonant holographic techniques in VHI applications. Figure 6-6 shows two possible imaging architectures to implement resonant holographic imaging. Both architectures utilize a plane wave reference volume hologram on account of the flat optical cavity. Spherical wave reference beams would require a confocal cavity.

Figure 6-7 is the schematic of a resonant holographic imaging setup in which the point source lies outside the cavity. At Bragg match, the collimated beam incident on the resonant cavity diffracts strongly. As the point source moves, two factors contribute to the drop in the diffraction efficiency:

1. The Bragg selectivity of the volume hologram causes the point source to become Bragg mismatched as it moves out of focus, leading to a drop in the diffracted power.
2. The defocused beams fail to satisfy the optical path length resonance conditions across the field, also leading to a drop of the diffracted power.

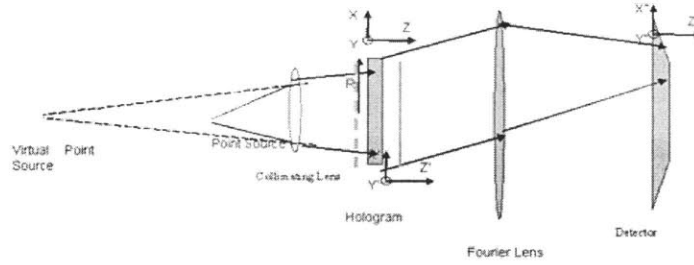


Figure 6-7: Imaging architectures for resonant imaging with point source outside resonant cavity.

These two effects in tandem ensure that the resonant holographic PSF is tighter than each of the individual resonant and holographic PSFs.

Figure 6-8 is a resonant holographic imaging setup in which the point source lies inside the cavity. This setup has an even tighter PSF than the arrangement of Figure 6-7 because the presence of the lens within the cavity ensures that both Bragg mismatch and resonant defocus occurs more rapidly than the case where the lens is outside the cavity. The analysis of the PSF of this geometry can be simplified by realizing that the point source will progressively shift by different amounts along the axial direction after each round-trip inside the cavity. This amplifies the actual offset of the point source. We can get the recursion formula for this shift as

$$z_{o,new} = z_{o,old} + \frac{f^2}{2 \left(2L - 2f + \frac{f^2}{2\Delta Z} \right)}. \quad (6.10)$$

The complete theoretical calculation of the resonant holographic PSFs is currently in progress. Figure 6-9 shows qualitative agreement between theoretical and experimental images on the camera for progressively increasing longitudinal displacement. Figure 6-10 shows experimental PSFs of a plane wave reference VHI and a resonant VHI system with the object inside the cavity.

We believe that resonant holography can significantly enhance the performance of VHI and other volume holographic systems. Recently our group has demonstrated that cross-talk effects can be reduced using Hermite-Gauss mode confocal resonant

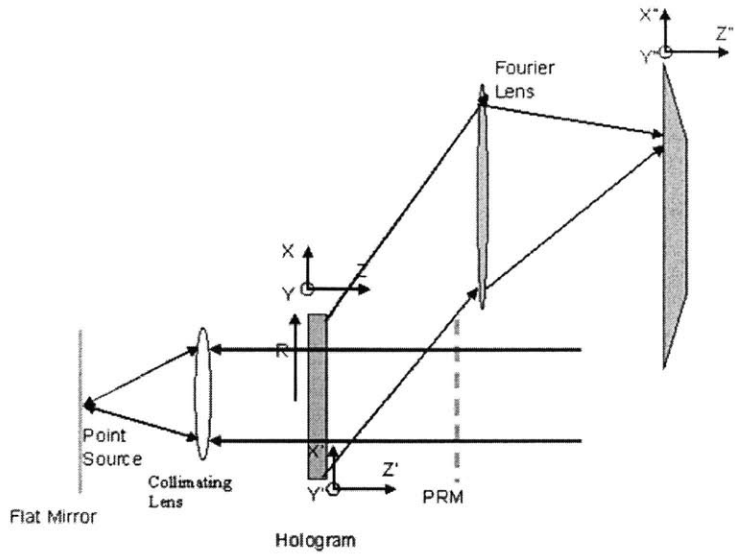


Figure 6-8: Imaging architectures for resonant imaging with point source inside resonant cavity.

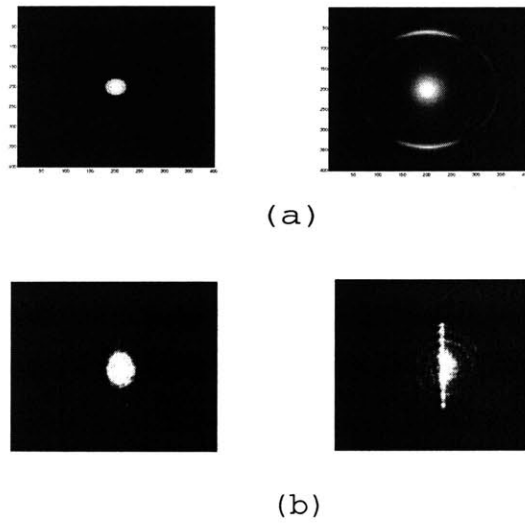


Figure 6-9: (a) Calculated and (b) experimental images on detector for readout of resonant volume hologram with the point source inside the cavity.

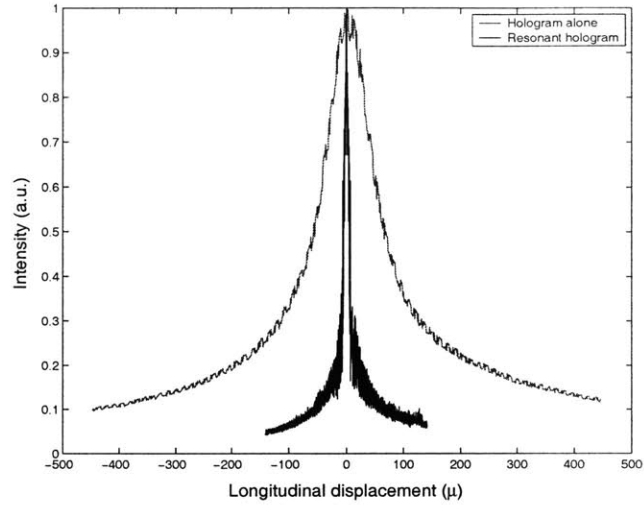


Figure 6-10: Resolution of resonant VHI with the point source within the cavity. The working distance was $660\mu\text{m}$. The NA of the system was 0.1, the one pass diffraction efficiency $\eta_1 = 3.5\%$, loss = 5% . $\eta_\infty(\text{theory}) = 12\%$, $\eta_\infty(\text{expt}) = 10\%$. Non resonant depth resolution $\Delta z_{\text{FWHM}} \sim 120\mu\text{m}$. Resonant depth resolution $\Delta z_{\text{FWHM}} \sim 10\mu\text{m}$.

holographic cavities [129]. Efforts are currently underway to build a feedback stabilized resonant cavity for further imaging applications.

Chapter 7

Conclusion

We have seen that the use of volume holograms for optical imaging presents tremendous potential for the capture of rich visual information. Unlike other optical elements like lenses/beam-splitters, a volume hologram can perform *several* functions in an imaging system. The results presented in this thesis and in earlier work [5, 81, 92, 123, 84, 82, 90, 83, 85, 105, 130] demonstrate the flexibility offered by a volume hologram based imaging system for application specific imaging. The target applications are broad, encompassing target acquisition and recognition, bio-imaging, long range surface profilometry and chemical sensing. In this chapter, we recapitulate the fundamental aspects of volume holographic imaging and present some directions for further research.

7.1 Volume Holographic Imaging Summary

The volume holographic lens is manufactured by recording a three-dimensional interference pattern of two (or more) mutually coherent beams as shown in Fig. 7-1(a). The recording is independent of the object to be imaged, although the selection of the type of hologram to be recorded (e.g. the type of reference beam) can be based prior information about the *type* of objects to be imaged (e.g. the average working distance, reflective vs. fluorescent, etc.). Simple recording schemes include interfering a spherical reference (SR) or planar reference (PR) beam with a planar signal beam to

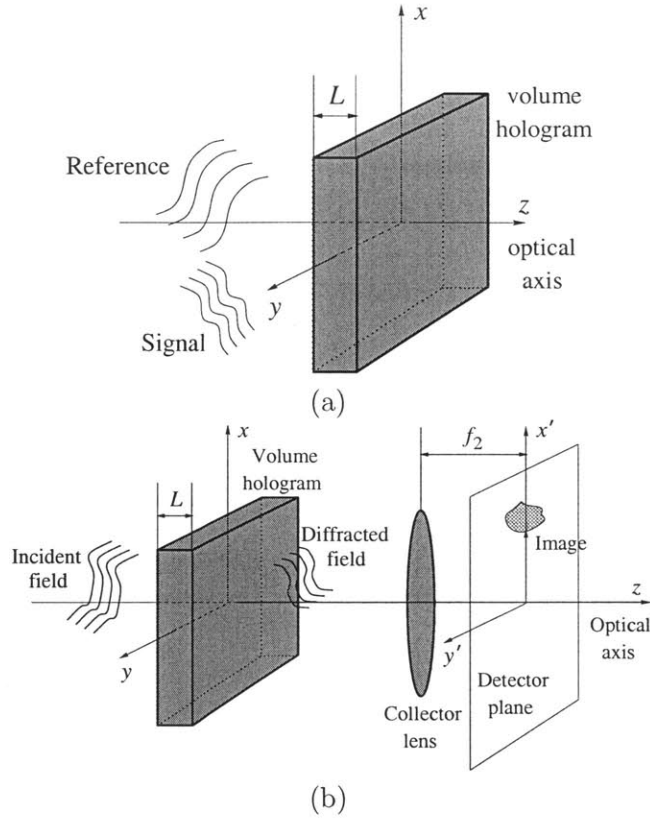


Figure 7-1: General schematic of volume holographic imaging. (a) The volume grating is the recorded 3D interference pattern of two mutually coherent beams (b) The imaging step consists of reading out the volume hologram by an unknown object illumination. The volume hologram diffracts only the Bragg matched components of the object illumination. This effect is used in conjunction with scanning to recover the object illumination.

record holograms in the transmission, reflection or 90° geometry [5]. After recording is complete, the hologram is fixed; no further processing is done on the hologram (just like the fixed lenses in an imaging instrument after they are ground and polished).

During imaging, the recorded holograms are probed by the incident illumination as shown in Fig. 7-1(b). We have rigorously discusses two volume holographic imaging setups in this thesis:

1. SR-VHI systems incorporate transmission geometry volume holograms recorded with a spherical reference and planar signal. We have demonstrated several

volumetric scan-based 3D imaging systems in Chapter 4. SR-VHI systems have a curved degeneracy line and this results in images being skewed on the detector plane. To overcome this problem, we prefer to use

2. PR-VHI systems with transmission volume holograms recorded with planar reference and signal beams. The straight fringes in the volume grating results in a straight degeneracy line. PR-VHI is our method of choice for most imaging systems both broadband and monochromatic as described in chapter 4.

When probed with a unknown light source, the VHI system diffracts the Bragg matched [8, 65] components of the incident illumination. The diffracted field is monitored by a detector or a detector array. The diffracted field intensity captured by the detector is the “image” formed by the VHI system and can be used to determine the required object information like the 3D spatial and/or spectral characteristics of the object of interest.

Most of our VHI systems were restricted to use a volume hologram that was the result of a single exposure. By multiplexing several holograms with a sequence of exposures on the same holographic material, it is possible to reduce scanning even more and obtain the $2\frac{1}{2}$ D or 3D image even in real time, provided there are enough pixels on the 2D camera to adequately sample the higher dimensional object information. This method was employed in Ref. [84] to obtain hyperspectral and 3D spatial information from a fluorescent object in real time, *i.e.* without scanning.

We have shown that despite its apparent simplicity, VHI offers unique imaging capabilities that are not available in traditional lenses. A volume hologram based system can be designed to outperform a conventional imaging system with respect to the resolution of the image produced. However, volume holographic systems suffer from a serious disadvantage as compared to other systems since only the light diffracted by the volume hologram is used for imaging - the rest of the light goes straight through and is wasted. There are two ways to solve this problem:

1. Resonant volume holography is an all optical method to enhance the diffraction efficiency of volume holograms. A resonant volume holographic system can im-

prove both the depth resolution and diffraction efficiency of simple monochromatic VHI systems like the surface profilometer. However, resonance would not work for broadband VHI systems on account of the extremely stringent path-length criterion for resonance.

2. VHI can be used in tandem with other 3D imaging systems. The beam diffracted by the hologram can be monitored as mentioned earlier for VHI whereas the straight through beam can be the input to another 3D imaging system for further optical information processing. Thus, no object information is lost in such a combined VHI-3D imager setup. We have discussed a combined VHI-confocal system in Chapter 6

7.2 Future work

This thesis represents a preliminary step in the direction of understanding and building VHI systems for practical use. There are several interesting issues that need to be addressed in translating the unique potential of VHI to a practical commercially viable imaging applications. Some of the issues are:

1. We have restricted our analysis to simple SR-VHI and PR-VHI schematics. However, it is not necessary that these systems should be the optimal configuration for every imaging application. Preliminary work has been done [131] on designing an optimum volume holographic microscope. Further work could include the recording of the volume hologram as a parameter in designing the optimal VHI for a particular application.
2. In this thesis, the digital processing of the volume holographic image data has relied on simple least-squares optimization techniques. Research is currently underway to implement more efficient deconvolution schemes like a modified Vitterbi algorithm [132] for super-resolution in VHI.
3. The response of the VHI system to randomly varying optical fields must be

understood and well characterized. Some preliminary studies on 3D optical coherence [133] are underway to understand this phenomenon better.

4. As mentioned earlier, the limited diffraction efficiency of volume holograms is one of the most severe issues in VHI. Initial experimental results [134] suggest that resonant holography may solve this problem and also enhance depth resolution further¹. A feedback controlled resonant optical cavity should be built to verify this.
5. We have shown that a combination VHI–confocal system can sometimes outperform each stand–alone system. It would be helpful to generalize this calculation for different systems like coherence imagers, tomographers, binocular systems etc.
6. We have presented preliminary comparisons in between VHI and some other systems. It would be very useful to compare VHI to the most commonly used imaging system for a particular imaging application to bring out the advantages and drawbacks of any of using the VHI system for that particular application.

¹Our colleagues at Ondax, Inc. are also looking into the problem of limited diffraction efficiency from volume holograms. They have come up with a novel method of making a volume hologram with several multiplexed volume gratings in glass. Each grating has diffraction efficiency approaching 100%.

Appendix A

Volume diffraction in the Born approximation

In most holographic materials, volume holograms are recorded as a modulation of the material refractive index, resulting after exposure to the interference pattern between the signal and reference beams. Consider such a dielectric material, as shown in Fig. A-1, occupying a volume \mathcal{V} in space, with a position-dependent dielectric constant $\epsilon(\mathbf{r})$. We assume that the modulation is weak and narrow-band, *i.e.*

$$\epsilon(\mathbf{r}) = \epsilon_o + \tilde{\epsilon}(\mathbf{r})e^{i\mathbf{K}_g \cdot \mathbf{r}}, \quad \epsilon_o \gg |\tilde{\epsilon}(\mathbf{r})|. \quad (\text{A.1})$$

Here, ϵ_o is the dielectric constant before exposure, \mathbf{K}_g is the carrier wave-vector of the grating and $\tilde{\epsilon}(\mathbf{r})$ is a low bandwidth modulation (in the sense that the maximum spatial frequency contained in $\tilde{\epsilon}(\mathbf{r})$ is much less than \mathbf{K}_g) representing the intensity modulation stored in the volume hologram. The hologram is illuminated with an incident optical field \mathbf{E}_p at a frequency ω . In this appendix, we derive the diffracted field \mathbf{E}_d , under some approximations, as the first-order solution to a wave scattering problem. The result is the diffraction integral (A.14).

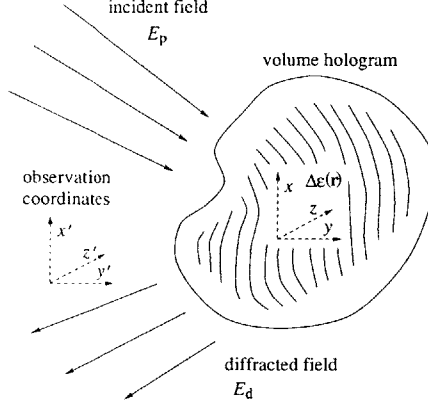


Figure A-1: Volume diffraction geometry.

The electromagnetic field satisfies Maxwell's equations in charge-free space:

$$\begin{aligned}
 \nabla \times \mathbf{E} &= i\omega\mathbf{B} & \nabla \cdot \mathbf{D} &= 0 \\
 \nabla \times \mathbf{H} &= -i\omega\mathbf{E} & \nabla \cdot \mathbf{B} &= 0,
 \end{aligned} \tag{A.2}$$

where $\mathbf{E} = \mathbf{E}_p + \mathbf{E}_d$ is the total electric field, $\mathbf{D} = \epsilon\mathbf{E}$ is the dielectric displacement, \mathbf{H} is the magnetic field, $\mathbf{B} = \mu\mathbf{H}$ is the magnetic induction and μ is the magnetic permeability, hereafter assumed to be μ_0 , the magnetic permeability of vacuum. From the two curl equations, we obtain

$$\begin{aligned}
 \nabla \times \nabla \times \mathbf{E} &= -\mu\epsilon(\omega^2\mathbf{E}) \\
 \Rightarrow \nabla(\nabla \cdot \mathbf{E}) - \nabla^2\mathbf{E} &= \omega^2\mu\epsilon\mathbf{E}
 \end{aligned} \tag{A.3}$$

To calculate $\nabla \cdot \mathbf{E}$, we use Gauss' law:

$$\nabla \cdot (\epsilon\mathbf{E}) = \nabla\epsilon \cdot \mathbf{E} + \epsilon\nabla \cdot \mathbf{E} = 0 \Rightarrow \nabla \cdot \mathbf{E} = -\frac{\nabla\epsilon \cdot \mathbf{E}}{\epsilon} \approx -\frac{\nabla\epsilon \cdot \mathbf{E}}{\epsilon_0} \tag{A.4}$$

The modulation gradient is calculated explicitly as

$$\nabla\epsilon(\mathbf{r}) = \nabla (\tilde{\epsilon}(\mathbf{r})e^{i\mathbf{K}_g \cdot \mathbf{r}}) = e^{i\mathbf{K}_g \cdot \mathbf{r}}\nabla\tilde{\epsilon}(\mathbf{r}) + i\tilde{\epsilon}(\mathbf{r})e^{i\mathbf{K}_g \cdot \mathbf{r}}\mathbf{K}_g. \tag{A.5}$$

The narrow-band grating assumption essentially means that the first term in the above expression is negligible, and we thus obtain

$$\frac{\nabla \epsilon \cdot \mathbf{E}}{\epsilon_0} = -i \frac{(\mathbf{K}_g \cdot \mathbf{E}) \tilde{\epsilon}(\mathbf{r}) e^{i\mathbf{K}_g \cdot \mathbf{r}}}{\epsilon_0} \quad (\text{A.6})$$

The wave equation for the electric field in the presence of the volume hologram follows from (A.3) after substitution of (A.6):

$$\nabla^2 \mathbf{E} + \omega^2 \mu_0 \epsilon_0 \mathbf{E} = -i \nabla \left(\frac{(\mathbf{K}_g \cdot \mathbf{E}) \tilde{\epsilon}(\mathbf{r}) e^{i\mathbf{K}_g \cdot \mathbf{r}}}{\epsilon_0} \right) - \omega^2 \mu_0 \tilde{\epsilon}(\mathbf{r}) e^{i\mathbf{K}_g \cdot \mathbf{r}} \mathbf{E} \quad (\text{A.7})$$

Using the narrow-band grating approximation, the first term on the right-hand side of (A.7) simplifies to [65]

$$\approx -i [(\mathbf{K}_g \nabla) \mathbf{E} + i(\mathbf{K}_g \cdot \mathbf{E}) \mathbf{K}_g] \tilde{\epsilon}(\mathbf{r}) e^{i\mathbf{K}_g \cdot \mathbf{r}} / \epsilon_0 \quad (\text{A.8})$$

We now define the matrix operator¹

$$\begin{aligned} U(\mathbf{r}) &= \tilde{\epsilon}(\mathbf{r}) e^{i\mathbf{K}_g \cdot \mathbf{r}} \left[\frac{-i(\mathbf{K}_g \nabla) + \mathbf{K}_g(\mathbf{K}_g \cdot)}{\epsilon_0} + \omega^2 \mu_0 i r c \right] \\ &= \frac{\tilde{\epsilon}(\mathbf{r})}{\epsilon_0} e^{i\mathbf{K}_g \cdot \mathbf{r}} [-i(\mathbf{K}_g \nabla) + \mathbf{K}_g(\mathbf{K}_g \cdot) + k^2], \end{aligned} \quad (\text{A.9})$$

where we used $k = 2\pi/\lambda = \omega\sqrt{\mu_0\epsilon_0}$. The wave equation then takes the compact form

$$(\nabla^2 + k^2) \mathbf{E} = U(\mathbf{r}) \mathbf{E}; \quad (\text{A.10})$$

i.e. the volume diffraction problem is formally equivalent to scattering of the vector field \mathbf{E} from the potential $U(\mathbf{r})$. Let $G(\mathbf{r})$ denote the Green's matrix for the homogeneous wave vector corresponding to (A.10). The solution to (A.10) is a series of

¹We define by $\mathbf{K}_g \nabla$ the outer product of the two operators, as opposed to $\mathbf{K}_g \cdot \nabla$, which denotes the inner product as usual.

diffracted orders [135]

$$\mathbf{E} = \mathbf{E}_p + \sum_{k=1}^{\infty} \mathbf{E}_d^{(k)}, \quad \text{where} \quad (\text{A.11})$$

$$\mathbf{E}_d^{(k)}(\mathbf{r}) = \int_{\mathcal{V}} d^3\mathbf{r}' G(\mathbf{r} - \mathbf{r}') U(\mathbf{r}') \mathbf{E}_d^{(k-1)} \quad (\text{A.12})$$

$$= \int_{\mathcal{V}} d^3\mathbf{r}_1 \dots \int_{\mathcal{V}} d^3\mathbf{r}_k G(\mathbf{r} - \mathbf{r}_1) U(\mathbf{r}_1) \dots G(\mathbf{r} - \mathbf{r}_k) U(\mathbf{r}_k) \mathbf{E}_p(\mathbf{r}_k). \quad (\text{A.13})$$

The iteration is initialized by $\mathbf{E}_d^{(0)}(\mathbf{r}) = \mathbf{E}_p(\mathbf{r})$. It is evident from (A.9) and (A.12) that the k^{th} order term in the solution is of the same magnitude as $(\tilde{\epsilon}(\mathbf{r})/\epsilon_o)^k$. Therefore, consistent with the weak modulation assumption, only the first term is non-negligible. This assumption is called *Born's approximation*; it is violated for strong gratings, when the coupled wave formulation [66] must be used. In most cases, we will work with volume holograms that have low diffraction efficiencies and hence, we are justified to express the diffracted field as

$$\mathbf{E}_d(\mathbf{r}) = \int_{\mathcal{V}} d^3\mathbf{r}' G(\mathbf{r} - \mathbf{r}') U(\mathbf{r}') \mathbf{E}_p(\mathbf{r}'). \quad (\text{A.14})$$

The actual computation of the diffracted field, as given by the diffraction integral (A.14), is not always straightforward. We will now focus on scalar fields only and develop an approach based on 3D Fourier analysis which simplifies the calculations significantly. The key result of this analysis is equation (A.22), which follows directly from (A.14) for a scalar incident field. We assume that the incident field is a plane wave that is linearly polarized parallel to an arbitrary direction $\hat{\mathbf{e}}$, *i.e.*

$$\mathbf{E}_p = e^{i\mathbf{k}_p \cdot \mathbf{r}} \hat{\mathbf{e}} \quad (\mathbf{k}_p \perp \hat{\mathbf{e}}). \quad (\text{A.15})$$

The diffracted field is then simply

$$\mathbf{E}_d = \int_{\mathcal{V}} d^3\mathbf{r}' G(\mathbf{r} - \mathbf{r}') \tilde{\epsilon}(\mathbf{r}') e^{i\mathbf{K}_g \cdot \mathbf{r}'} \frac{(\mathbf{K}_g \cdot \hat{\mathbf{e}})(-i\nabla + \mathbf{K}_g) + k^2}{\epsilon_o} e^{i\mathbf{k}_p \cdot \mathbf{r}}. \quad (\text{A.16})$$

Green's dyadic for homogeneous space [46] is

$$G(\mathbf{r}) = \frac{e^{ik_p|\mathbf{r}|}}{4\pi|\mathbf{r}|} I_3 \quad (\text{outgoing waves only}), \quad (\text{A.17})$$

where $k_p = 2\pi/\lambda = |\mathbf{k}_p|$, and I_3 is the 3×3 identity matrix. Substituting into (A.16), we obtain

$$\mathbf{E}_d = s(\mathbf{k}_p) \int_{\mathcal{V}} d^3\mathbf{r}' \frac{e^{ik_p|\mathbf{r}-\mathbf{r}'|}}{4\pi|\mathbf{r}-\mathbf{r}'|} \tilde{\epsilon}(\mathbf{r}') e^{i(\mathbf{K}_g+\mathbf{k}_p)\cdot\mathbf{r}'}, \quad (\text{A.18})$$

where

$$s(\mathbf{k}_p) = \frac{(\mathbf{K}_g \cdot \hat{\mathbf{e}})(\mathbf{k}_p + \mathbf{K}_g) + k^2 \hat{\mathbf{e}}}{\epsilon_o}. \quad (\text{A.19})$$

Note that the diffracted field is also linearly polarized in the direction of $\hat{\mathbf{s}}$. The angle α formed between $\hat{\mathbf{s}}$ and the incident polarization $\hat{\mathbf{e}}$ is given by

$$\cos \alpha = \hat{\mathbf{s}} \cdot \hat{\mathbf{e}} = \frac{(\mathbf{K}_g \cdot \hat{\mathbf{e}})^2 + k^2}{\sqrt{(\mathbf{K}_g \cdot \hat{\mathbf{e}})^2 (|\mathbf{K}_g|^2 + 2\mathbf{K}_g \cdot \mathbf{k}_p + 3k^2) + k^4}}. \quad (\text{A.20})$$

For a more general scalar incident field

$$\mathbf{E}_p = \tilde{E}_p(\mathbf{r}) e^{i\mathbf{k}_p \cdot \mathbf{r}} \hat{\mathbf{e}} \quad (\text{A.21})$$

where $\tilde{E}_p(\mathbf{r})$ is a low bandwidth modulation, the diffracted field is

$$\mathbf{E}_d = s(\mathbf{k}_p) \int_{\mathcal{V}} d^3\mathbf{r}' \frac{e^{ik_p|\mathbf{r}-\mathbf{r}'|}}{4\pi|\mathbf{r}-\mathbf{r}'|} \tilde{\epsilon}(\mathbf{r}') \tilde{E}_p(\mathbf{r}') e^{i(\mathbf{K}_g+\mathbf{k}_p)\cdot\mathbf{r}'}. \quad (\text{A.22})$$

This expression has a simple intuitive interpretation: each infinitesimal region inside the hologram acts as a point source with amplitude proportional to the local amplitude of the incident field and the local value of the refractive index modulation; the diffracted field is obtained as a coherent superposition of the field emitted by all these infinitesimal point sources comprising the volume hologram. Further, the 3D Fourier space equivalent of (A.22) can also be calculated. We will not go into the details here (They can be found in [86]) and just present the final result. The 3D diffracted

spectrum $\xi(\mathbf{k}_d)$ is

$$\xi(\mathbf{k}_d, z) = \frac{e^{ik_{dz}z}}{2} \mathbf{A}(\mathbf{k}_p, \mathbf{k}_d) \quad (\text{A.23})$$

$$\mathbf{A}(\mathbf{k}_p, \mathbf{k}_d) = \frac{s(\mathbf{k}_p)}{k_{dz}} \int_{\mathcal{V}} d^3\mathbf{r}' \tilde{\epsilon}(\mathbf{r}') e^{i(\mathbf{K}_g + \mathbf{k}_p - \mathbf{k}_d) \cdot \mathbf{r}'} \quad (\text{A.24})$$

The quantity $\mathbf{A}(\mathbf{k}_p, \mathbf{k}_d)$ is the three-dimensional Fourier transform of the index modulation $\tilde{\epsilon}(\mathbf{r}') e^{i\mathbf{K}_g \cdot \mathbf{r}'}$, calculated at spatial frequency $(\mathbf{k}_p - \mathbf{k}_d)$. It represents the amplitude of the diffracted field propagating in the direction of $\tilde{\mathbf{k}}_d$ when the hologram is the illuminated by a plane wave incident at direction $\tilde{\mathbf{k}}_p$.

Bibliography

- [1] M. Born and E. Wolf. *Principles of optics*. Pergamon Press, Cambridge, UK, 7th edition, 1998.
- [2] J. W. Goodman. *Introduction to Fourier Optics*. Mc Graw-Hill, New York, 2nd edition, 1996.
- [3] D. J. Brady and Z. U. Rahman. Integrated analysis and design of analog and digital processing in imaging systems: introduction to feature issue. *Appl. Opt.*, 41(29):6049–6049, 2002.
- [4] W. T. Cathey and E. R. Dowski. New paradigm for imaging systems. *Appl. Opt.*, 41(29):6080–6092, 2002.
- [5] G. Barbastathis and D. J. Brady. Multidimensional tomographic imaging using volume holography. *Proc. IEEE*, 87(12):2098–2120, 1999.
- [6] G. G. Yang, H. S. Chen, and E. N. Leith. Volume reflection holographic confocal imaging. *Appl. Opt.*, 39(23):4076–4079, 2000.
- [7] P. J. van Heerden. Theory of optical information storage in solids. *Appl. Opt.*, 2(4):393–400, 1963.
- [8] Pochi Yeh. *Introduction to photorefractive nonlinear optics*. Wiley & Sons, New York, 1993.
- [9] J. W. Goodman. *Statistical Optics*. J. Wiley & Sons, 1985.

- [10] C. J. R. Sheppard and C. J. Cogswell. Three-dimensional imaging in confocal microscopy. In T. Wilson, editor, *Confocal microscopy*, chapter 4, pages 143–169. Academic Press, San Diego, CA, 1990.
- [11] D. Huang, E. A. Swanson, C. P. Lin, J. S. Schuman, W. G. Stinson, W. Chang, M. R. Hee, T. Flotte, K. Gregory, C. A. Puliafito, and J. G. Fujimoto. Optical coherence tomography. *Science*, 254(5035):1178–1181, 1991.
- [12] P. Grangeat. Mathematical framework of cone beam 3D reconstruction via the first derivative of the radon transform. In G. T. Herman, A. K. Louis, and F. Natterer, editors, *Lecture Notes in Mathematics 1497: Mathematical Methods in Tomography*. Springer-Verlag, Berlin, 1991.
- [13] D. Marr. *Vision*. W. H. Freeman & Co., New York, 1982.
- [14] M. Minsky. Microscopy apparatus. US Patent 3,013,467, granted 12/19/1961.
- [15] G. Binnig, C. F. Quate, and C. Gerber. Atomic force microscope. *Phys. Rev. Lett*, 56(9):930–933, 1986.
- [16] G. Binnig, H. Rohrer, C. Gerber, and E. Weibel. 7×7 reconstruction on si(111) resolved in real space. *Phys. Rev. Lett*, 50(2):120–123, 1983.
- [17] M. V. Klein and T. E. Furtak. *Optics*. Wiley, New York, New York, 1986.
- [18] A. Stein and G. Barbastathis. Axial imaging necessitates loss of lateral shift invariance. *Appl. Opt.*, 41:6055–6061, 2002.
- [19] C. J. R. Sheppard and A. Choudhury. Image formation in the scanning microscope. *Opt. Acta*, 24:1051–1073, 1977.
- [20] C. J. R. Sheppard and C. J. Cogswell. Three-dimensional image formation in confocal microscopy. *J. Microscopy*, 159(2):179–194, 1990.
- [21] C. J. Cogswell and C. J. R. Sheppard. Confocal differential interference contrast (DIC) microscopy: including a theoretical analysis of conventional and confocal DIC imaging. *J. Microscopy*, 165(1):81–101, 1992.

- [22] I. J. Cox, C. J. R. Sheppard, and T. Wilson. Super-resolution by confocal fluorescence microscopy. *Optik*, 60:391–396, 1982.
- [23] P. T. C. So, T. French, W. M. Yu, K. M. Berland, C. Y. Dong, and E. Gratton. Time-resolved fluorescence microscopy using two-photon excitation. *Bioimaging*, 3(2):49–63, 1995.
- [24] P. H. Van Cittert. *Physica*, 1:201, 1934.
- [25] F. Zernike. *Proc. Phys. Soc.*, 61:158, 1948.
- [26] V. Schooneveld. Image formation from coherence functions in astronomy. In D. Reidel, editor, *IAU colloquium*, volume 49, Groningen, 1978.
- [27] A. J. Devaney. The inversion problem for random sources. *J. Math. Phys.*, 20:1687–1691, 1979.
- [28] W. H. Carter and E. Wolf. Correlation theory of wavefields generated by fluctuating, three-dimensional, primary, scalar sources I. General theory. *Opt. Acta*, 28:227–244, 1981.
- [29] I. J. LaHaie. Inverse source problem for three-dimensional partially coherent sources and fields. *J. Opt. Soc. Am. A*, 2:35–45, 1985.
- [30] A. M. Zarubin. Three-dimensional generalization of the Van Cittert-Zernike theorem to wave and particle scattering. *Opt. Commun.*, 100(5-6):491–507, 1992.
- [31] J. Rosen and A. Yariv. Three-dimensional imaging of random radiation sources. *Opt. Lett.*, 21(14):1011–1013, 1996.
- [32] J. Rosen and A. Yariv. General theorem of spatial coherence: application to three-dimensional imaging. *J. Opt. Soc. Am. A*, 13(10):2091–2095, 1996.
- [33] J. Rosen and A. Yariv. Reconstruction of longitudinal distributed incoherent sources. *Opt. Lett.*, 21(22):1803–1805, 1996.

- [34] D. Marks, R. Stack, and D. J. Brady. Three-dimensional coherence imaging in the Fresnel domain. *Appl. Opt.*, 38(8):1332–1342, 1999.
- [35] K. Itoh and Y. Ohtsuka. Fourier-transform spectral imaging: retrieval of source information from three dimensional spatial coherence. *J. Opt. Soc. Am. A*, 3(1):94–100, 1986.
- [36] D. L. Marks, R. A. Stack, D. J. Brady, D. C. Munson, Jr., and R. B. Brady. Visible cone-beam tomography with a lensless interferometric camera. *Science*, 284(5423):2164–2166, 1999.
- [37] U. Morgner, W. Drexler, F. X. Kartner, X. D. Li, C. Pitris, E. P. Ippen, and J. G. Fujimoto. Spectroscopic optical coherence tomography. *Opt. Lett.*, 25(2):111–113, 2000.
- [38] E. R. Dowski and W. T. Cathey. Extended depth of field through wave-front coding. *Appl. Opt.*, 34(11):1859–1866, 1994.
- [39] D. L. Marks, R. Stack, D. Brady, and J. van der Gracht. Three-dimensional tomography using a cubic-phase plate extended depth-of-field system. *Opt. Lett.*, 24(11):253–255, 1999.
- [40] A. V. Jelalian. *Laser radar systems*. Boston: Artech House, 1992.
- [41] A. P. Pentland. A new sense for depth of field. *IEEE Trans. Pattern Anal. Machine Intell.*, 9:523–531, 1987.
- [42] P. Cavanagh. Reconstructing the third dimension: Interactions between color, texture, motion, binocular disparity and shape. *Computer Vision, Graphics, and Image Processing*, 37(2):171–195, 1987.
- [43] A. M. Bruckstein. On shape from shading. *Computer Vision, Graphics, and Image Processing*, 44(2):139–154, 1988.
- [44] O. Faugeras and Q.-T. Luong. *The geometry of multiple images*. MIT Press, Cambridge, MA, 2001.

- [45] C. M. Vest. Formation of images from projections: Radon and abel transforms. *J. Opt. Soc. Am.*, 64(9):1215–1218, 1974.
- [46] J. D. Jackson. *Classical electrodynamics*. J. Wiley & Sons, second edition, 1975.
- [47] P. Potluri, M. Xu, and D. J. Brady. Imaging with random 3d reference structures. *Opt. Exp.*, 11(18):2134–2141, 2003.
- [48] D. Psaltis, D. Brady, X. G. Gu, and S. Lin. Holography in artificial neural networks. *Nature*, 343(6256):325–330, 1990.
- [49] D. Brady and D. Psaltis. Control of volume holograms. *J. Opt. Soc. Am. A*, 9(7):1167–1182, 1992.
- [50] D. Gabor. A new microscopic principle. *Nature*, 161:777–779, 1948.
- [51] E. Leith and J. Upatnieks. Wavefront reconstruction and communication theory. *J. Opt. Soc. Am.*, 52:1123–1134, 1962.
- [52] J. Zhang, B. Tao, and J. Katz. Three-dimensional velocity measurements using hybrid HPIV. In R. J. Adrian, D. F. G. Durao, F. Durst, M. V. Heitor, M. Maeda, and J. H. Whitelaw, editors, *Developments in Laser Techniques and Fluid Mechanics*. Springer, Berlin, 1997.
- [53] T. Zhang and I. Yamaguchi. Three-dimensional microscopy with phase-shifting digital holography. *Opt. Lett.*, 23(15):1221–1223, 1998.
- [54] J. H. Milgram and W. Li. Computational reconstruction of images from holograms. *Appl. Opt.*, 41(5):853–864, 2002.
- [55] P. K. Rastogi, editor. *Holographic interferometry*. Springer-Verlag, 1994.
- [56] J. C. Wyant. Two-wavelength interferometry. *Appl. Opt.*, 10:2113, 1971.
- [57] C. Polhemus. Two-wavelength interferometry. *Appl. Opt.*, 12(9):2071–2074, 1973.

- [58] M. Bertero, P. Brianzi, and E. R. Pike. Super-resolution in confocal scanning microscopy. *Inv. Probl.*, 3(2):195–212, 1987.
- [59] M. Bertero, P. Boccacci, M. Defrise, C. De Mol, and E. R. Pike. Super-resolution in confocal scanning microscopy. II. The incoherent case. *Inv. Probl.*, 5(4):441–461, 1989.
- [60] M. Bertero, P. Boccacci, R. E. Davies, and E. R. Pike. Super-resolution in confocal scanning microscopy. III. The case of circular pupils. *Inv. Probl.*, 7(5):655–674, 1991.
- [61] M. Bertero, P. Boccacci, R. E. Davies, F. Malfanti, E. R. Pike, and J. G. Walker. Super-resolution in confocal scanning microscopy. IV. Theory of data inversion by the use of optical masks. *Inv. Probl.*, 8(1):1–23, 1992.
- [62] J. G. Walker, E. R. Pike, R. E. Davies, M. R. Young, G. J. Brakenhoff, and M. Bertero. Superresolving scanning optical microscopy using holographic optical processing. *J. Opt. Soc. Am. A*, 10(1):59–64, 1993.
- [63] J. Grochmalicki, E. R. Pike, J. G. Walker, M. Bertero, P. Boccacci, and R. E. Davies. Superresolving masks for incoherent scanning microscopy. *J. Opt. Soc. Am. A*, 10(5):1074–1077, 1993.
- [64] M. Bertero, P. Boccacci, F. Malfanti, and E. R. Pike. Super-resolution in confocal scanning microscopy. V. Axial super-resolution in the incoherent case. *Inv. Probl.*, 10(5):1059–1077, 1994.
- [65] E. N. Leith, A. Kozma, J. Upatnieks, J. Marks, and N. Massey. Holographic data storage in three-dimensional media. *Appl. Opt.*, 5(8):1303–1311, 1966.
- [66] H. Kogelnik. Coupled wave theory for thick hologram gratings. *Bell Syst. Tech. J.*, 48(9):2909–2947, November 1969.
- [67] D. Psaltis. Parallel optical memories. *Byte*, 17(9):179, 1992.
- [68] D. Psaltis and F. Mok. Holographic memories. *Sci. Am.*, 273(5):70–76, 1995.

- [69] J. F. Heanue, M. C. Bashaw, and L. Hesselink. Volume holographic storage and retrieval of digital data. *Science*, 265(5173):749–752, 1994.
- [70] H. Lee, X.-G. Gu, and D. Psaltis. Volume holographic interconnections with maximal capacity and minimal cross talk. *J. Appl. Phys.*, 65(6):2191–2194, March 1989.
- [71] D. Brady, S. Lin, X. G. Gu, and D. Psaltis. Holography in artificial neural networks. *Nature*, 343:325–330, 1990.
- [72] Y. S. Abu-Mostafa and D. Psaltis. Optical neural computers. *Sci. Am.*, 256(3):66–73, 1987.
- [73] J. Hong. Applications of photorefractive crystals for optical neural networks. *Opt. Quant. Electr.*, 25(9):S551–S568, 1993.
- [74] D. J. Brady, A. G.-S. Chen, and G. Rodriguez. Volume holographic pulse shaping. *Opt. Lett.*, 17(8):610–612, 1992.
- [75] P.-C. Sun, Y. Fainman, Y. T. Mazurenko, and D. J. Brady. Space-time processing with photorefractive volume holography. *SPIE Proceedings*, 2529:157–170, 1995.
- [76] P.-C. Sun, Y. T. Mazurenko, W. S. C. Chang, P. K. L. Yu, and Y. Fainman. All-optical parallel-to-serial conversion by holographic spatial-to-temporal frequency encoding. *Opt. Lett.*, 20(16):1728–1730, 1995.
- [77] K. Purchase, D. Brady, G. Smith, S. Roh, M. Osowski, and J. J. Coleman. Integrated optical pulse shapers for high-bandwidth packet encoding. *SPIE Proceedings*, 2613:43–51, 1996.
- [78] D. M. Marom, P.-C. Sun, and Y. Fainman. Analysis of spatial-temporal converters for all-optical communication links. *Appl. Opt.*, 37(14):2858–2868, 1998.
- [79] C. Mead. Neuromorphic electronic systems. *Proc. IEEE*, 78(90):1629–1636, 1990.

- [80] C. A. Mead. Scaling of MOS technology to submicrometer feature sizes. *Analog Int. Circ. & Signal Proc.*, 6(1):9–25, 1994.
- [81] G. Barbastathis, M. Balberg, and D. J. Brady. Confocal microscopy with a volume holographic filter. *Opt. Lett.*, 24(12):811–813, 1999.
- [82] A. Sinha and G. Barbastathis. Volume holographic telescope. *Opt. Lett.*, 27:1690–1692, 2002.
- [83] A. Sinha and G. Barbastathis. Volume holographic imaging for surface metrology at long working distances. *Opt. Exp.*, 11(24):3202–3209, 2003.
- [84] W. Liu, D. Psaltis, and G. Barbastathis. Real time spectral imaging in three spatial dimensions. *Opt. Lett.*, 27:854–856, 2002.
- [85] A. Sinha, W. Sun, and G. Barbastathis. Broadband volume holographic imaging. *submitted to Appl. Opt.*, 2003.
- [86] H. Coufal, D. Psaltis, and G. Sincerbox, editors. *Holographic data storage*. Springer, Berlin - New York, 2000.
- [87] G. Barbastathis, M. Levene, and D. Psaltis. Shift multiplexing with spherical reference waves. *Appl. Opt.*, 35:2403–2417, 1996.
- [88] G. Barbastathis and D. Psaltis. Shift-multiplexed holographic memory using the two-lambda method. *Opt. Lett.*, 21(6):429–431, 1996.
- [89] D. Psaltis, F. Mok, and H.Y.-S. Li. Nonvolatile storage in photorefractive crystals. *Opt. Lett.*, 19(3):210–212, 1994.
- [90] A. Sinha, W. Sun, T. Shih, and G. Barbastathis. Volume holographic imaging in the transmission geometry. *Appl. Opt.*, 43(7):1–19, 2004.
- [91] H Fisk-Johnson. An improved method for computing a discrete hankel transform. *Computer Physics Communications*, 43(2):181–202, 1987.

- [92] G. Barbastathis and A. Sinha. Information content of volume holographic imaging. *Trends in Biotechnology*, 19(10):383–392, 2001.
- [93] M. Subbarao and S. Gopal. Depth from defocus: a spatial domain approach. *Intl. Jrnl. of Comp. Vision*, 13(3):271–294, 1994.
- [94] T. Wilson, editor. *Confocal microscopy*. Academic Press, San Diego, CA, 1990.
- [95] G. Barbastathis and D. Psaltis. Volume holographic multiplexing methods. In H. Coufal, D. Psaltis, and G. Sincerbox, editors, *Holographic data storage*. Springer, 2000.
- [96] U. R. Dhond and J. K. Aggarwal. Structure from stereo: A review. *IEEE Tans. Sys. Man. Cyber.*, 14(6):1489–1510, 1989.
- [97] J. Aloimonos, I. Weiss, and A. Bandyopadhyay. Active vision. In *Proc. ICCV*, pages 35–54, 1987.
- [98] N. Ahuja and A. Abbott. Active stereo: integrating disparity, vergence, focus, aperture, and calibration for surface estimation. *Patt. Anal. and Mach. Intell.*, 15(10):1007–1029, 1993.
- [99] N. George and W. Chi. Extended depth of field using a logarithmic asphere. *Jrnl. of Opt. A: Pure and Appl. Opt.*, 5(5):S157–S163, 2003.
- [100] M. Bertero and P. Boccacci. *Introduction to inverse problems in imaging*. Institute of Physics, 1998.
- [101] G. Barbastathis and D. Psaltis. Volume holographic multiplexing methods. In H. J. Coufal, D. Psaltis, and G. T. Sincerbox, editors, *Holographic Data Storage*. Springer Optical Sciences, 2000.
- [102] F. H. Mok, G. W. Burr, and D. Psaltis. A system metric for holographic memory systems. *Opt. Lett.*, 21(12):896–898, 1996.

- [103] J. White, H. Ma, J. Lang, and A. Slocum. An instrument to control parallel plate separation for nanoscale flow control. *Rev. Sc. Instruments*, 74(11):4869–4875, 2003.
- [104] A. Sinha, W. Sun, T. Shih, and G. Barbastathis. N-ocular holographic 3d imaging. In *OSA Annual Meeting*, Orlando, FL, 2002. paper WD7.
- [105] A. Sinha, W. Sun, and G. Barbastathis. N-ocular volume holographic imaging. *submitted to Appl. Opt.*, 2003.
- [106] C. E. Shannon. *Bell Syst. Tech. J.*, 27:379–423, 1948.
- [107] C. E. Shannon. *Bell Syst. Tech. J.*, 27:623–656, 1948.
- [108] G. T. Di Francia. *J. Opt. Soc. Am.*, 59:799–804, 1969.
- [109] B. R. Frieden. Information, and the restorability of images. *J. Opt. Soc. Am.*, 60(4):575–576, 1970.
- [110] R. N. Bracewell. Radio astronomy techniques. In S. Flügge, editor, *Encyclopaedia of physics*, volume 54. Springer-Verlag, 159.
- [111] H.-Y. S. Li, Y. Qiao, and D. Psaltis. Optical network for real-time face recognition. *Appl. Opt.*, 32(26):5026–5035, 1993.
- [112] M. Levene, G. J. Steckman, and D. Psaltis. Method for controlling the shift invariance of optical correlators. *Appl. Opt.*, 38(2):394–398, 1999.
- [113] E. N. Leith, A. Kozma, J. Upatnieks, J. Marks, and N. Massey. Holographic data storage in three-dimensional media. *Appl. Opt.*, 5(8):1303–1311, August 1966.
- [114] D. Slepian. *Bell Syst. Tech. J.*, 37:163, 1958.
- [115] H. H. Barrett, J. L. Denney, R. F. Wagner, and K. J. Myers. Objective assessment of image quality. II. Fisher information, Fourier crosstalk, and figures of merit for task performance. *J. Opt. Soc. Am. A*, 12(5):834–852, 1995.

- [116] H. H. Barrett and W. E. Smith. Hotelling trace criterion as a figure of merit for the optimization of imaging systems. *J. Opt. Soc. Am. A*, 3(5):717–725, 1986.
- [117] T. M. Cover and J. A. Thomas. *Elements of information theory*. J. W. Wiley, 1991.
- [118] M. Balberg, G. Barbastathis, S. Fantini, and D. J. Brady. Confocal imaging through scattering media with a volume holographic filter. *Proc. SPIE*, 3919:69–74, 2000.
- [119] D. Psaltis and N. Farhat. Optical information-processing based on an associative-memory model of neural nets with thresholding and feedback. *Opt. Lett.*, 10(2):98–100, 1985.
- [120] D. Z. Anderson. Coherent optical eigenstate memory. *Opt. Lett.*, 11:56, 1986.
- [121] W. H. Steier, G. T. Kavounas, R. T. Sahara, and J. Kumar. Enhanced opto-optical light deflection using cavity resonance. *Appl. Opt.*, 27(8):1603–1606, 1988.
- [122] S. A. Collins and H. J. Caulfield. Optical holographic interconnects: categorization and potential efficient passive resonated holograms. *J. Opt. Soc. Am. A*, 6(10):1568–1577, 1989.
- [123] A. Sinha and G. Barbastathis. Resonant holography. *Opt. Lett.*, 27:385–387, 2002.
- [124] A. Yariv. *Optical Electronics*. Saunders College, 4th edition, 1991.
- [125] D. Z. Anderson. Coupled resonators employing phase-conjugating and ordinary mirrors. *Opt. Lett.*, 9(9):417–419, 1984.
- [126] A. Bearden, M. P. O’Neill, L. C. Osborne, and T. L. Wong. Imaging and vibrational analysis with laser-feedback interferometry. *Opt. Lett.*, 18(3):238–240, 1993.

- [127] M. A. Scobey, W. J. Lekki, and T. W. Geyer. Filters create thermally passive, stable multiplexers. *Laser Focus World*, 33(3):111–116, 1997.
- [128] F. Mok, G. W. Burr, and D. Psaltis. A system metric for holographic memory systems. *Opt. Lett.*, 21(12):896–898, 1996.
- [129] K. Tian and G. Barbastathis. Crosstalk in resonant holographic memories. *to appear in Jrnl. Opt. Soc. Am. A*, 2004.
- [130] A. Sinha, G. Barbastathis, W. Liu, and D. Psaltis. Imaging using volume holograms. *to appear in Opt. Eng.*, 2003.
- [131] R. Menon, D. Gil, J. Rivas, G. Barbastathis, and A. Sinha. Optimum volume holographic microscope. In *OSA Annual Meeting*, Long Beach, CA, 2001. paper MC5.
- [132] M. A. Neifeld and Y. Wu. Parallel image restoration with a two-dimensional likelihood-based algorithm. *Appl. Opt.*, 41(23):4812–4824, 2002.
- [133] K. Tian and G. Barbastathis. Coherence patterns originating from incoherent volume sources. *to appear in Opt. Lett.*, 2004.
- [134] A. Sinha, W. Sun, and G. Barbastathis. Resolution of resonant holographic imaging. In *OSA Annual Meeting*, Orlando, FL, 2002. paper ThFF6.
- [135] C. Cohen-Tannoudji, B. Diu, and F. Laloë. *Quantum Mechanics*. Hermann & Wiley-Interscience, Paris, France, 1977.